INTERNATIONAL JOURNAL OF
IJCOE
COASTAL, OFFSHORE & ENVIRONMENTAL ENGINEERING

Volume 3 | Issue 4 | Nov 2018

www.ijcoe.org info@ijcoe.org

International Journal of Coastal, Offshore and Environmental Engineering (IJCOE) Vol. 3 / Issue. 4 / Nov 2018 12

International Journal of Coastal, Offshore & Environmental Engineering
Since 2015
ISSN: 2980-8731 (online)

Volume 3 | Issue 4| Nov 2018
IJCOE
Editor-in-Chief: Prof. Hamid S.Bahai

International Journal of Coastal, Offshore & Environmental Engineering
Since 2015
ISSN: 2980-8721 (online)

In The Name of God

Message from the Editor-in-Chief

The IJCOE journal office was established in 2015,and its first issue was published in 2016. TheIJCOE covers a wide range of research in thefields of oceanography & ocean technology, aswell as marine industries & marine engineering.The editorial board of IJCOE consists of nearly130 of the greatest scientists and researchersfrom over 30 countries worldwide, and thejournal's review board comprises 1,000 membersfrom all five continents. The membership andapplication process for joining the editorial andreview boards of this journal is ongoing. IJCOE isa research-academic quarterly journal that haspublication and distribution permissions fromthe Press Organization and permission topublish scientific-research articles from theMinistry of Science, Research, and Technology(MSRT) with an "A" rating. It also holds a "Q1"rating from the ISC institute with an impactfactor (IF) of approximately 0.43 and isconsidered a "core journal" (prestigious andoutstanding journal). IJCOE is an open-accessjournal and allows the download and receipt ofaccepted articles in full text for free. It respectsand adheres to copyright and COPE regulations.The journal's office operates 24/7, providingservices to researchers. In addition to publishinga regular quarterly journal, IJCOE has 16 specialissues on specific topics in preparation. It alsoprovides conditions for publishing specializedbooks, references, and handbooks. Moreover, itis ready to cooperate with the secretariats ofreputable international conferences to publishtheir selected and outstanding articles. IJCOEevaluates, appraises, and publishes books,articles, and the scientific achievements andfindings of esteemed researchers and scientistsworldwide who are innovating and conductingin-depth research in the "important and strategicfield of the maritime technology & Oceanengineering." It welcomes any form of jointcooperation with universities, research institutes,and related research centers at the national,regional, and international levels, and extends ahand for collaboration.

Classification of Editorial Board in IJCOE

Editor-in-Chief

Director-in-Chief

Deputy Editor

Executive Managers

English Text Editor

Technical Editor

International Editorial Board

National Editorial Board

Editorial Board Associate

Editorial Board Assistant

Guest Editorial Board

Advisory Board

Administrative Coordinator

Honorary Board Member

Methodology Advisor

Author Benefits

- Open Access
- Rapid Publication
- Thorough Peer-Review
- No Copyright Constraints
- Coverage by Leading Indexing Services
- Discounts On Article Processing Charges (APC)
- No Space Constraints, No restriction on the maximum length of the papers, number of figures or colors

INTERNATIONAL JOURNAL OF IJCOE COASTAL, OFFSHORE & ENVIRONMENTAL ENGINEERING

Aims of IJCOE

Hydrodynamics

Marine equipment

Structural mechanics

Ocean environmental predictions

Stochastic calculations Experimental

Automatic Control of Marine Systems

Scope of IJCOE

Marine Hazards

Ocean Acoustics

Naval Architecture

Ocean Engineering

Coastal Engineering

Marine Meteorology

Marine Earth Sciences

Underwater Technology

Marine Renewable Energy

Polar & Arctic Engineering

Marine Renewable Energy

Marine Geography & Geodesy

Marine Environmental Engineering

Automatic Control of Marine Systems

Hydro Physics & Physical Oceanography

Type of papers

- Case Studies
- Book Reviews
- Review Article
- Letters to the Editor
- Methodology Papers
- Editorials and Commentaries
- Response or Rejoinder Papers
- Perspective or Opinion Papers
- Conceptual or Theoretical Papers
- Meta-Analysis and Systematic Reviews
- Short Communications or Brief Reports
- Research Articles (Original Research Papers)

Scientific Research Journal

Ministry of Science, Research And Technology (MSRT)

Jurnal Ranking 2023: A

Ministry Of Science, Research And Technology (ISC)

Citation Impact 2022: 0.429

Quartile 2022 : Q1

Core Collection

IJCOE is a Member of

Cantact Us

Office 1 | Research Institute of Meteorology and Atmospheric Science

Address | Tehran, Shahid Kharrazi Highway, Pajoohesh Blvd, Research Institute of Meteorology and Atmospheric Science, Sand and Dust Storm International Research Center (SDS-IRC), No. 13, 1st floor.

Phone | +982144787652

Postal code | 13611-14977

website | www.rimac.ac.ir

Office 2 | Iranian National Institute for Oceanography and Atmospheric Science

Address | Tehran, Dr. Fatemi Gharbi St., Shahid Etemadzade St., No. 3, third floor.

Phone | +982166944873

Postal code | 13389 – 14118

website | www.inio.ac.ir

Email | Info@ijcoe.org

Website | www.ijcoe.org

Follow Us

www.ijcoe.org

INTERNATIONAL JOURNAL OF IJCOE COASTAL, OFFSHORE & ENVIRONMENTAL ENGINEERING

Volume & Issue:

Volume 3, Issue 4, November 2018

Number of Articles: 6

Content

INTERNATIONAL JOURNAL OF
COASTAL & OFFSHORE ENGINEERING IJCOE Vol.3 /No. 4/Winter 2018 (1-11)

Available online at: http://ijcoe.org/browse.php?a_code=A-10-89-1&sid=1&slc_lang=en

Numerical Study on Hydrodynamic Force and Wave Induced Vortex Dynamics around Cylindrical Pile

Mohammad Mohammad Beigi kasvaei[1], Mohammad Hossein Kazeminezhad[2*], Abbas Yeganeh-Bakhtiary[3]

[1] *PhD Candidate, Iranian National Institute for Oceanography & Atmospheric Science, Tehran, Iran; mmbeigi@inio.ac.ir*
[2*] *Corresponding Author: Assistant Professor, Iranian National Institute for Oceanography & Atmospheric Science, Tehran, Iran; mkazeminezhad@inio.ac.ir*
[3] *Associate Professor, School of Civil Engineering, IUST, Tehran, Iran; yeganeh@iust.ac.ir*

ARTICLE INFO

Article History:
Received: 30 Aug. 2017
Accepted: 5 Mar. 2018

Keywords:
Keulegan-Carpenter (KC) number
OpenFOAM
RANS Equations
Vortex Shedding
Wave-Pile Interaction

ABSTRACT

Three-dimensional numerical simulation of regular waves passing over cylindrical monopile was conducted to investigate the hydrodynamic forces and vortex dynamics. The rectangular wave flume and monopile were modeled with a solver; available in the open-source CFD toolkit OpenFOAM®. This solver applies the Reynolds-Averaged Navier-Stokes (RANS) equations with the volume of fluid technic (VOF) for tracking free surface. To validate numerical model, results were compared to experimental data, and admissible agreement was seen. Computations were done for four cases with different wave characteristics consequently for different Keulegan-Carpenter (KC) numbers. In-line force acting on pile was studied and the results indicated that the total in-line force was influenced as the KC number varied. The vortex dynamics around the pile was also investigated by means of the Q criterion and vorticity field. Furthermore, variation of bed shear stress around the pile was investigated; it was concluded that the bed shear stress was influenced by KC number which is the result of existence of horseshoe vortices. The bed shear stress near the pile was negative due to existing of the horseshoe vortex. It began when KC exceeds 6; while by increasing KC up to 20, the magnitude of negative values of bed shear stress near the pile increase which implied the horseshoe vortices were completely formed.

1. Introduction

Cylindrical piles are widely used in marine structures such as offshore wind turbine monopiles, offshore platform legs and jetty piers. These structures are subjected to waves with different conditions. Cylindrical piles regarding their dimensions and wave characteristics are categorized in slender, intermediate and large piles. This can be demonstrated by means of Keulegan-Carpenter (KC) number as:

$$\mathrm{KC} = \frac{U_m T}{D} \tag{1}$$

where U_m is the maximum of wave orbital velocity, T is wave period and D is the pile diameter. For the slender piles the flow field changes significantly with the increase of disturbance around the pile. At upstream of the pile, the horseshoe vortex is formed due to rotation in the incoming flow; the lee side vortices are caused by the rotation in the boundary layer over the surface of the pile [1]. For the intermediate piles, the turbulence around them is more complex. Existence of vortices around the pile affects the wave force acting on the pile which is one of the most criteria in pile design [2]. Consequently, a great deal of effort is required to investigate the vortex dynamics around the pile. For the large piles, flow does not separate, hence no vortices occur; while, reflection and diffraction occur [1]. It is beyond the scope of this paper to investigate on the large piles.

Due to the importance of wave-pile interaction, both physical and numerical modeling of the wave-pile interaction has been of great interest in the last decades. Sumer et al. [1] carried out vast experiments on flow passing over vertical cylinders as well as the wave induced vortex shedding around vertical cylinders. A range of different KC numbers is used to investigate its influence on different parameters around the pile e.g. vortices and bed shear stress.

Iwagaki and Ishida [2] conducted an experimental study on wake vortices and pressure distribution around a circular cylinder under oscillatory motion. It is concluded that the wave pressures around a cylinder are affected by both wake vortices and the dynamic pressure.

As mentioned before, numerical modelling of wave induced flow and hydrodynamic forces over pile also carried out in the literature [3-11]. Wave forcing from steep and fully nonlinear regular stream function waves on slender piles is computed by Paulsen et al. [12]. Jiang et al. [13] numerically studied the solitary waves propagating over a cylindrical pile to investigate wave loads and vortices. Haddorp [14] carried out literature review and analytical study on flow regime and scour around cylindrical pile. In order to categorize the flow regime around a vertical pile, a graph was presented based on Sumer and Fredsoe's [15] investigations. The graph shows three flow regimes or three pile categories as illustrated in Figure 1. As seen, KC= 1 and KC= 6 are the borders for categorizing between large, intermediate and slender pile, respectively. Moreover, it indicates that from KC= ∞ (current flow) to KC= 6, horseshoe vortices exist and KC= 1 is the limit state of existing lee-wake vortices. Based on Hoffmans and Verheij [16] and Coastal Engineering Manual [17], diffraction and reflection are significant when D/L > 0.1; however, Sumer and Fredsoe [15] and Isaacson [18] maintained D/L > 0.2 as the limit state for the diffraction limit.

Short literature review revealed that, some studies have been carried out on waves and pile interaction. However, few studies have been conducted on the wave force acting on the pile and vortex dynamics considering the slender and intermediate piles categories objectively. The main aim of the study presented in this paper is to investigate on the wave force acting on the pile and vortex dynamics around that and the effect of KC number on them, especially for slender pile, intermediate pile and when it is located in the borderline between slender and intermediate. The open source CFD code of OpenFOAM® is implemented to simulate non-breaking regular waves passing over the pile. The multiphase, Eulerian solver (interFoam) is applied to solve the governing equations. First, numerical results were compared to the experimental ones to validate the model. Then, four cases with different KC numbers were simulated to investigate hydrodynamic wave force, vortex dynamics and bed shear stress.

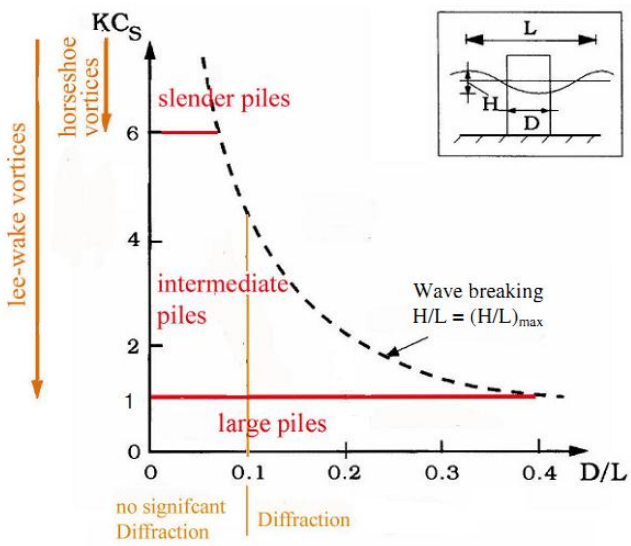

Figure 1. Demonstration of the flow regimes according to KC and *D/L*, adopted from [14]

2. Numerical Method

2.1. Governing Equations

Reynolds averaged Navier–Stokes equations (RANS) coupled with the continuity equation for incompressible flows in Cartesian coordinates are considered as the governing equations for the flow as follows:

$$\frac{\partial U_i}{\partial t}+\frac{\partial\left(U_iU_j\right)}{\partial x_i} = -\frac{1}{\rho}\frac{\partial P}{\partial x_i}+\frac{\partial}{\partial x_i}\left[\frac{\mu_{eff}}{\rho}\left(\frac{\partial U_i}{\partial x_j}+\frac{\partial U_j}{\partial x_i}\right)\right]+g_i-\frac{\partial\left(\overline{u_i'u_j'}\right)}{\partial x_j} \quad (2)$$

$$\frac{\partial U_i}{\partial x_i}=0 \quad (3)$$

where U_i denotes the mean fluid velocity component in the i-th direction, P is the pressure, ρ is the fluid density, g_i denotes the acceleration of gravity, u' denotes the fluctuating velocity component, $\mu_{eff}=\mu+\mu_t$, μ is the molecular viscosity, and μ_t is the turbulent eddy viscosity.

The Shear Stress Transport (SST) k-ω turbulence model is employed as the turbulence closure [19]. The turbulent kinetic energy k and the specific dissipation rate ω are expressed as

$$\frac{\partial(\rho k)}{\partial t}+\frac{\partial\left(\rho U_j k\right)}{\partial x_j}=P_k-\beta^*\rho\omega k+\frac{\partial}{\partial x_j}\left[\left(\mu+\sigma_k\mu_t\right)\frac{\partial k}{\partial x_j}\right] \quad (4)$$

$$\frac{\partial(\rho\omega)}{\partial t}+\frac{\partial\left(\rho U_j\omega\right)}{\partial x_j}=\frac{\gamma}{\upsilon_t}P_k-\beta\rho\omega^2+ \frac{\partial}{\partial x_j}\left[\left(\mu+\sigma_k\mu_t\right)\frac{\partial\omega}{\partial x_j}\right]+2\left(1-F_1\right)\frac{\rho\sigma_{\omega2}}{\omega}\frac{\partial k}{\partial x_j}\frac{\partial\omega}{\partial x_j} \quad (5)$$

here F_1 is a harmonic function expressed as

$$F_1=\tanh\left\{\min\left[\max\left(\frac{\sqrt{k}}{\beta^*\omega d},\frac{500\nu}{d^2\omega}\right),\frac{4\rho\sigma_{\omega2}k}{CD_{k\omega}d^2}\right]\right\}^4 \quad (6)$$

$$CD_{k\omega}=\max\left(2\rho\sigma_{\omega2}\frac{1}{\omega}\frac{\partial k}{\partial x_j}\frac{\partial\omega}{\partial\omega j},10^{-10}\right) \quad (7)$$

and $\nu_t=\mu_t/\rho$ is the turbulent kinematic viscosity, μ_t is computed as:

$$\mu_t=\frac{\rho a_1 k}{\max\left(a_{1\omega},\Omega F_2\right)} \quad (8)$$

$$F_2=\tanh\left[\max\left(2\frac{\sqrt{k}}{\beta^*\omega d},\frac{500\nu}{d^2\omega}\right)\right]^2 \quad (9)$$

where d is the distance between the field point and the nearest wall, and Ω is the vorticity magnitude.

Turbulence model constants are $\sigma_{k1}=0.85034$, $\sigma_{k2}=1.0$, $\sigma_{\omega1}=0.5$, $\sigma_{\omega2}=0.85616$, $\beta_1=0.075$, $\beta_2=0.0828$, $\beta^*=0.09$, $a_1=0.31$, $\gamma_1=5/9$ and $\gamma_2=0.4403$ [19, 20].

The free surface is traced by the VOF technique [21]. The governing equations of the flow and transport equation for the volume fraction of water were solved by a Finite Volume Method, in which the equations were integrated over the control volume and time.

2.2. Computational Domain and Boundary Conditions

A numerical rectangular shape wave tank was modelled, as shown in Figure 2. Dimensions were l_x, l_z and h in X, Z and Y directions, respectively. Pile diameter is demonstrated as D and water depth equals to d. As illustrated in Figure 2, no-slip wall boundary condition was considered for bottom of the wave tank, since flow velocity is zero in all directions. Slip wall boundary condition also was implemented for the side walls (front and back in OpenFOAM modelling) and ceiling of the tank [7]. Pile was located at specific distance away from left boundary of tank and no-slip wall boundary condition was considered for the hydraulically smooth pile face. Wave inlet was located at the left-hand side of the wave tank. At the inlet, regular waves using Airy theory as surface elevation were generated. As the wave tank was long enough for all the cases, waves can develop along that and can reach the real shape. At the outlet, a wave damping (relaxation zone) technique was performed which adequately stamps out reflections in the wave tank [4]. A toolbox of waves2Foam [7, 22] was adopted to generate and absorb free surface water waves. Waves2Foam applies the VOF and the relaxation zone technique (active sponge layers) to the 'InterFoam' multiple phase solver.

The "blockMesh" utility was used for mesh generation. Computational domain was divided to eight blocks. Total number of cells was O (10^5) in the modelling. Non-uniform mesh was used with relatively fine mesh close to the pile and bed to fully consider the wall boundary impact on numerical modelling. The finest grid next to the pile was about 0.01 of the pile diameter. Meshes were totally hexahedral and parallel to the stream lines. The numerical model was run with several forms of meshing to obtain the optimum one. The model results are not significantly sensitive to the selected mesh form and cells sizes. Figure 3 shows the general view of the applied mesh.

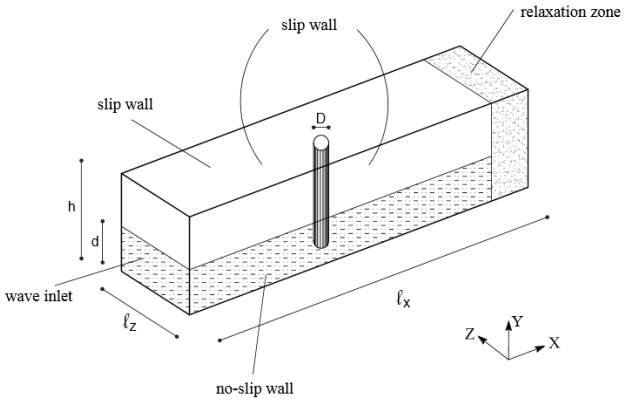

Figure 2. Computational domain and boundary conditions (not scale)

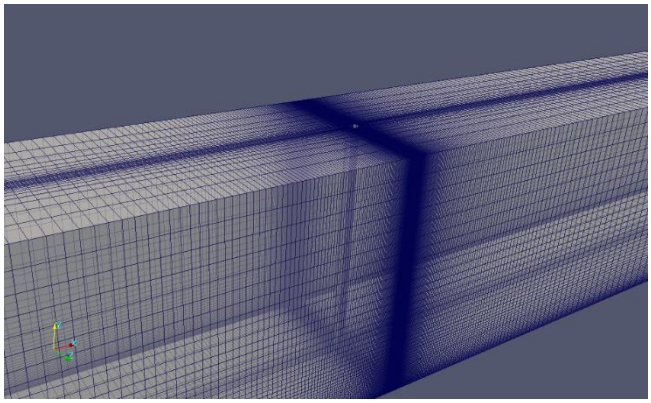

Figure 3. A view of applied mesh around the pile

3. Model Validation

Prior to investigate the effects of KC number on hydrodynamic force acting upon and vortex dynamics around the vertical pile, model validation was carried out using experimental data of Mo et al. [6]. The experiments conducted in the Large Wave Flume (GKW) of Coastal Research Centre (FZK) in Hannover, Germany. This wave flume has an effective length of 309 m, a width of 5 m and a depth

of 7 m. A steel circular cylinder with a diameter of 0.7 m was instrumented and installed in the flume. In order to simulate above mentioned experimental condition, total length of numerical flume in the direction of wave propagation was considered l_x= 77 m to reduce the computational costs, while other dimensions were as experimental conditions. Pile diameter (D) was 0.7 m and located at 40 m away from the wave inlet (left boundary). Wave height and wave period were 1.2 m and 4 s, respectively and KC number was 6.13. For mesh generation, blockMesh utility of OpenFOAM was used and all meshes were hexahedral with total number of about 433,000. Boundary conditions were the same as the other cases as described in section 3. Simulation was conducted for 40 s which means 10 waves were generated and passed over the pile.

For model validation, some numerical results were compared to experimental ones. Comparison of simulated and measured nondimensional in-line force acting on the pile is presented in Figure 4. The wave forces on the pile was predicted by integrating the pressure and viscous stresses along the pile in a discretized manner. The pressure and viscous forces from each cell face on the surface of the pile were summed to find the total pressure and viscous forces, respectively. As seen from the figure, there is a good agreement between the numerical results and the experimental ones. Thus, the numerical model can predict the hydrodynamic force acting on the pile well. Figure 5 illustrates water particle velocity for both numerical simulation and experimental results at wave gauge located at x=40 m near the side wall in two different levels (y/d= -0.32 and y/d= -0.57, y is distance from still water level and d is water depth). The particle velocity was nondimensionalized by dividing it to the phase velocity of the wave. In both levels, acceptable agreement was seen between the numerical results and the experimental ones. In addition, time histories of dynamic pressure along the half perimeter of the pile in six angular points at y/d= -0.11 are depicted in Figure 6. As seen, the numerical results conform closely with experimental results. Since generated vortices around the pile affect the pressure field, by obtaining acceptable results in modeling of pressure field, it is expected that the numerical model performs well in simulation of vortex dynamics as well.

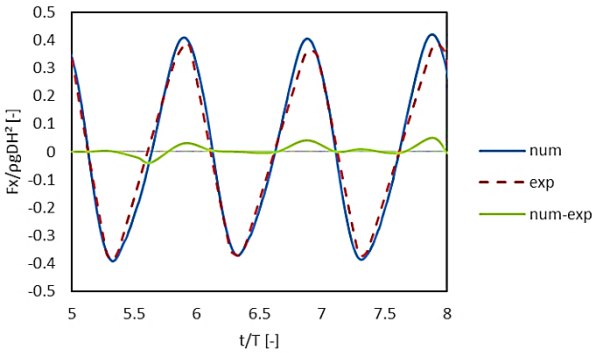

Figure 4. Total in-line force acting upon pile in numerical model and experimental results

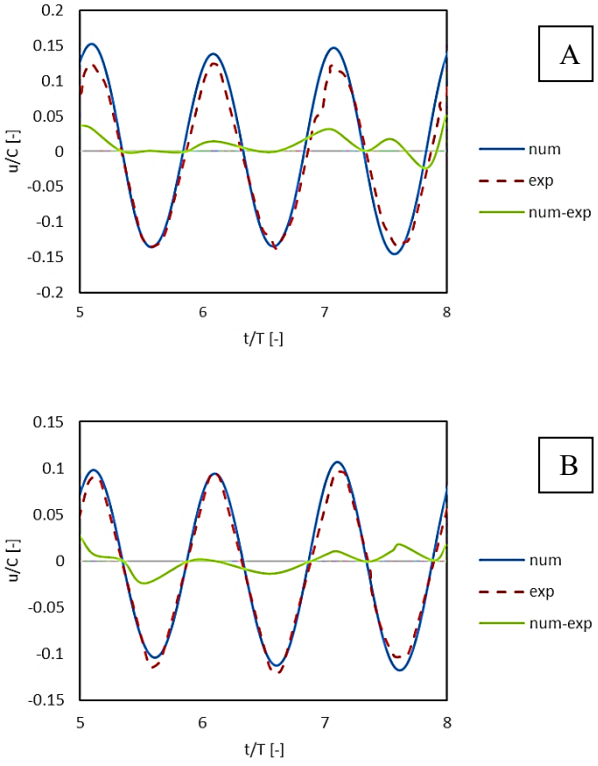

Figure 5. Water particle velocity at wave gauge location with coordinate $x = 40\text{m}$ near the side wall in two different levels (A) $y/d = -0.32$ (B) $y/d = -0.57$

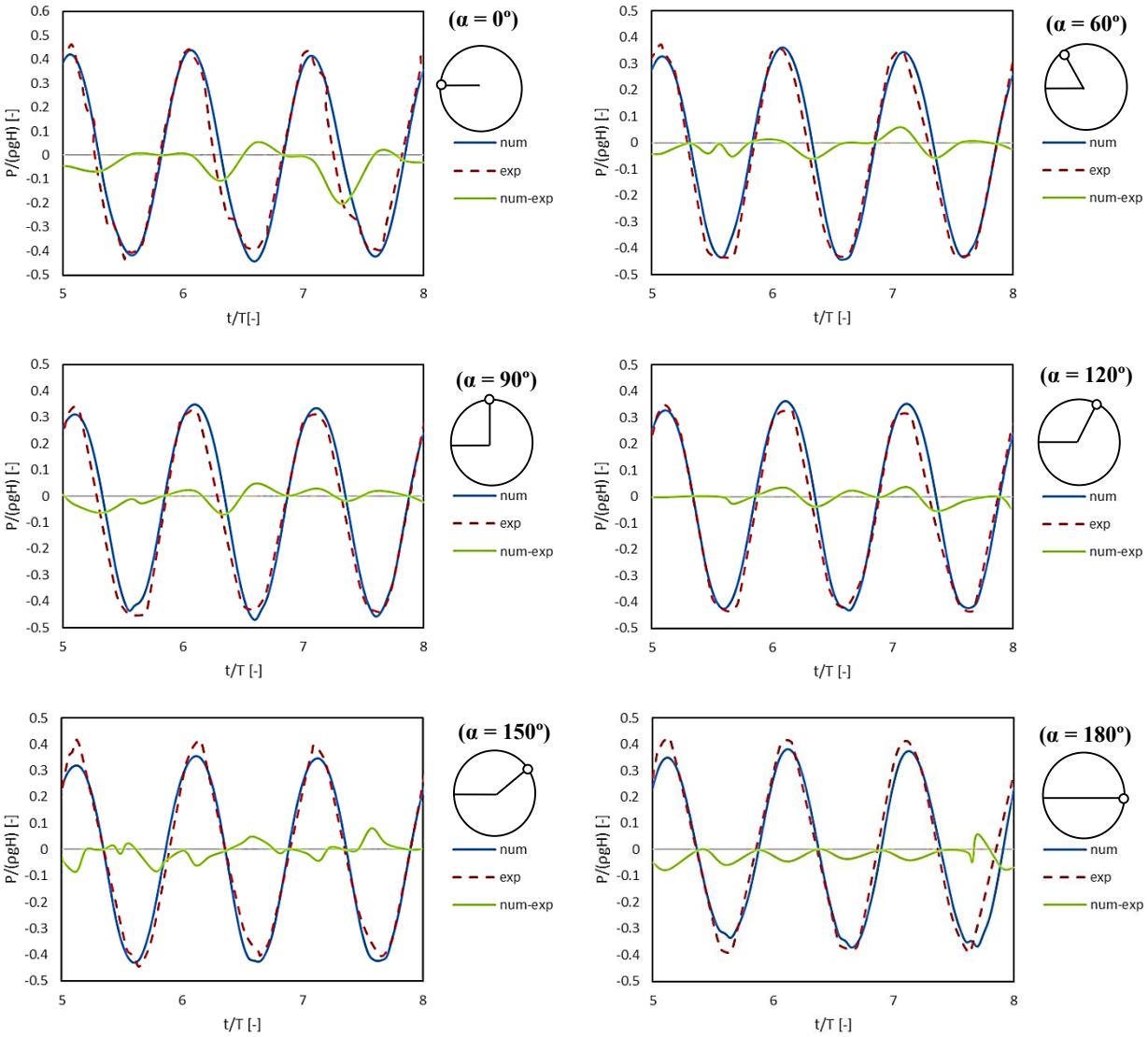

Figure 6. Time histories of dynamic pressure along the perimeter of the pile at in six angular points at y/d= -0.11

Although, the free surface study is not the main goal of this paper, due to the presence of the wave and the wave-pile interaction, accuracy in free surface modelling is also required. Therefore, the numerical results and experimental data for the surface elevation at four wave gauges are presented and compared in Figure 7. The reference wave amplitude in Figure 7 is the maximum elevation of WG 11, which is located near the side wall at x = 40 m. The other three wave gauges are located close to the pile face which locations are shown for every single graph on its top. As it is shown good agreement were seen among numerical results and those of the experiments. This approved that the use of Airy wave theory in wave inlet does not affect the results, which is due to the fact that the wave develops along the flume. For WG_{cyl} 1 which is located in frontline of the pile, it is seen that the numerical model tends to overestimate the wave trough passed the pile, which can be attributed to disturbance in front of the pile.

4. Result and Discussion

Four cases of experimental studies of Sumer et al. [1] with different wave characteristics are numerically modelled to investigate the influence of KC number on the hydrodynamic forces acting on pile and vortex dynamics around the pile. In all four cases wave tank dimensions were equal to l_x= 26.5 m, l_z= 0.6 m and h= 0.8 m. Table 1 presents the wave and the pile characteristics. Pile diameter and water depth were respectively 0.04 and 0.4 m. A multi block hexahedral mesh with 560,000 total number of cells was generated by blockMesh utility. The simulations were carried out for 10 waves period. All aspects of numerical method including consistency, stability, convergence, accuracy and mesh dependency on the results were considered during the simulations.

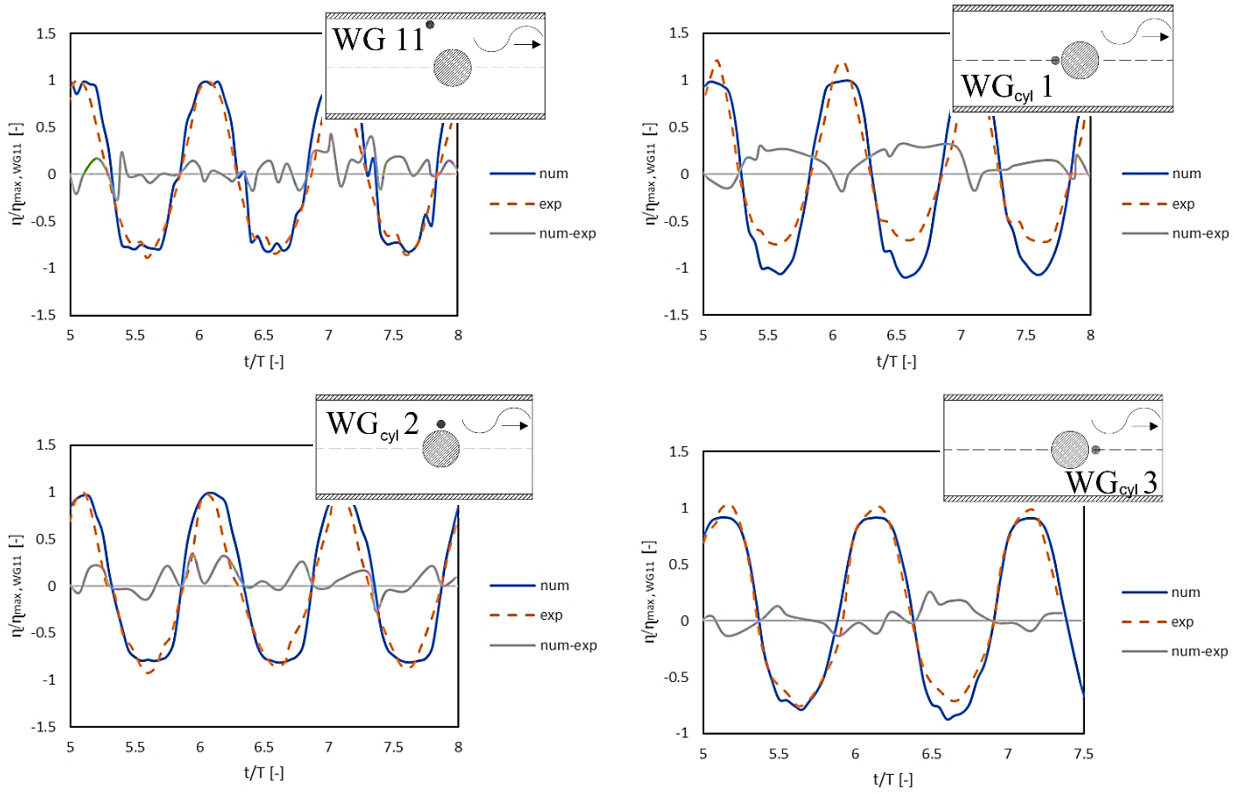

Figure 7. Time histories of surface elevation at 4 different wave gauges

Table 1. Wave and pile characteristics in simulations

Case No.	Water depth (*d*) [m]	Wave height (*H*) [m]	Wave period (*T*) [sec]	Pile diameter (*D*) [m]	*KC* number [-]
1	0.4	0.024	2.2	0.04	2.8
2	0.4	0.023	4.4	0.04	6.1
3	0.4	0.039	4.4	0.04	10.3
4	0.4	0.08	4.4	0.04	20.1

4.1. Hydrodynamic Force

When a pile is exposed to incident waves, depend on the size of circular pile and wave characteristics, the flow field disturbance is different. Hydrodynamic forces acting on pile can be estimated by Morison's equation. It can be said Morison's equation is valid when $D/L<0.2$ (L is the wave length and D is the pile diameter) [23]. In addition to D/L, KC number is significant in the calculation of hydrodynamic forces acting on pile. In the above-mentioned cases $D/L<0.2$, while the related KC numbers are in three ranges: KC<6.0 (Case 1), KC≈ 6 (Case 2) and KC>6 (Cases 3-4). It is expected that the flow pattern and the hydrodynamic force affected by the KC variations.

The time series of total hydrodynamic in-line force acting on the pile for all cases with different KC numbers are depicted in Figure 8. As seen, variation of KC number influences on the hydrodynamic in-line force. According to Eq. (1), KC may change by variation in U_m, T or D. As seen in Table (1), in all four cases D and T are not changed, except for case 1. Therefore, for case 1, KC change due to change in T and for case 2, 3 and 4, KC change due to change in U_m, which is result of change in H. Comparing results for case 1 and 2 showed that change in KC due to change in T is not significantly influence on the in-line force on pile. While, for case 2, 3 and 4, in which change in KC is due to change in H, the in-line force increased remarkably by increasing KC. In Case 4 (KC= 20.1) which is in vortex shedding regime [9] (will be explained extensively in the next section), three pick points in negative values of force can be seen. These are due to vortex shedding behind the pile and consequently increasing of turbulence intensity around the pile.

As seen from Figure 8, in case 4 (cnoidal wave theory characteristics), the absolute value of the wave forces in the crest half period are larger than the absolute value of the wave forces in the trough half period. This is due to the fact that cnoidal waves have a sharp crests and very flat troughs [17].

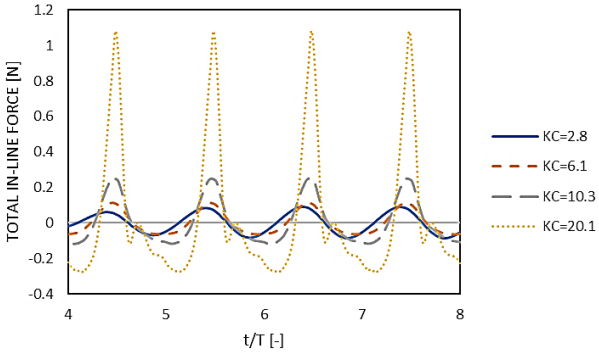

Figure 8. Time series of total hydrodynamic in-line force acting upon pile for all cases with different KC number

Figure 9 illustrates relation between the drag force to the inertia force components [23]. In the graph,

positions of the studied cases are specified by different symbols. It is obvious that for Case 1 (KC= 2.8) the inertia force component is dominant, and is 2 times larger than the drag force component. For Case 2 (KC= 6.1) red rectangle is located on border line and for Cases 3 and 4 that KC exceeds than 6, symbols are located in region, in which the inertia force component is equal to drag force component. As expected for small KC number condition inertia force is dominant, on the other hand for large KC number drag force is dominant. Recalling the Figure 1 ([14]'s graph), it is seen that case 1 belongs to intermediate pile region, while cases 3 and 4 belong to slender pile. Case 2 is near border line of intermediate and slender pile. It can be concluded that, for intermediate piles drag force component is half of inertia force component and for slender piles those components are equal. Fully developed vortices affected velocity field and then resulted in pressure field which might cause to increase the drag force. These were along with experimental data stated that wave pressures around a cylinder are affected by wake vortices [2]. Also, these vortices induce local pressure depressions in the wave field.

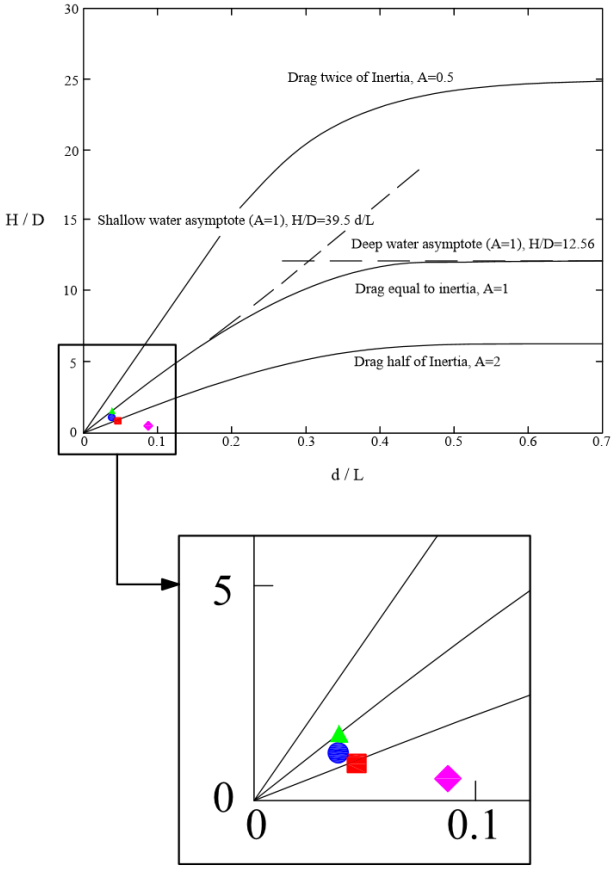

Figure 9. Relative magnitude of inertia and drag forces for cylinders with *D/L* < 0.2 [23]
Case 1 ◆, case 2 ■, case 3 ●, case 4 ▲

4.2. Vortex Dynamics

The vortex dynamics, related to horseshoe vortices, lee-wake vortices and vortex shedding are evaluated by means of Q criterion, vorticity and amplification factor of bed shear stress (α). The vorticity has been using in numerous studies to show vortex shedding around a structure. However, due to its weakness to distinguish between vortex cores and shear motions, the vorticity method can be replaced by other criteria, e.g. the Q criterion, the Δ criterion, the λ_{ci} criterion, and the λ_2 criterion [24]. These methods are formulated based on more precise mathematical foundations and obvious physical explanation. In this study, the Q criterion is applied to investigate vortex shedding around the pile in addition to vortices results. The Q criterion is estimated as follows:

$$Q = \frac{1}{2}\left(\|\Omega\|^2 - \|S\|^2\right) \tag{10}$$

where Ω is the rate-of-rotation tensor corresponding to the pure rotational motion and equals to

$$\Omega = \frac{1}{2}\left[\nabla U - (\nabla U)^T\right] \tag{11}$$

and S is the rate-of-strain tensor corresponding to the pure irrotational motion and equals to

$$S = \frac{1}{2}\left[\nabla U + (\nabla U)^T\right] \tag{12}$$

where U is the velocity vectors in three-dimensional Cartesian coordinate and, ∇U is the full local velocity gradient tensor.

In Figure 10, Q criterion variations around the pile at a specific instant time for all cases are depicted. In this figure, $\omega t = 90^\circ$ (left-hand side panel) and $\omega t = 270^\circ$ (right-hand side panel) mean pile is located in the crest and trough half-period, respectively. Therefore, for the former one, horseshoe vortices is formed in the left-hand side of the pile and lee-wake vortices is formed in the right-hand side of the pile. For the latter one, horseshoe vortices is formed in the right-hand side of the pile and lee-wake vortices is formed in the left-hand side of the pile. Regarding to Figure 10, there is no lee-wake vortices when KC= 2.8. By increasing KC to more than 6.0, horseshoe vortices are formed in front of the pile and symmetric lee-wake vortices behind the pile. In addition to horseshoe vortices in front of the pile, at KC= 10.3 and KC= 20.1, the vortex shedding are occurred behind the pile. It can be seen that when KC is very small, the horseshoe vortex may not even be formed. Instead, for the large KC the flow in each half-period is similar to when steady current, which are in line with Sumer et al. results [1]. In addition to Q criterion, the vorticity field is investigated for all cases. Here, vorticity in different stage during one wave period for case 4 (KC= 20.1) is depicted to show the generation and suppression of vortex shedding as well as its impact on the wave force due to increasing disturbance. Figure 11 shows the vorticity in every T/22 time step (= 0.2 sec) during one wave period for case 4 (KC= 20.1).

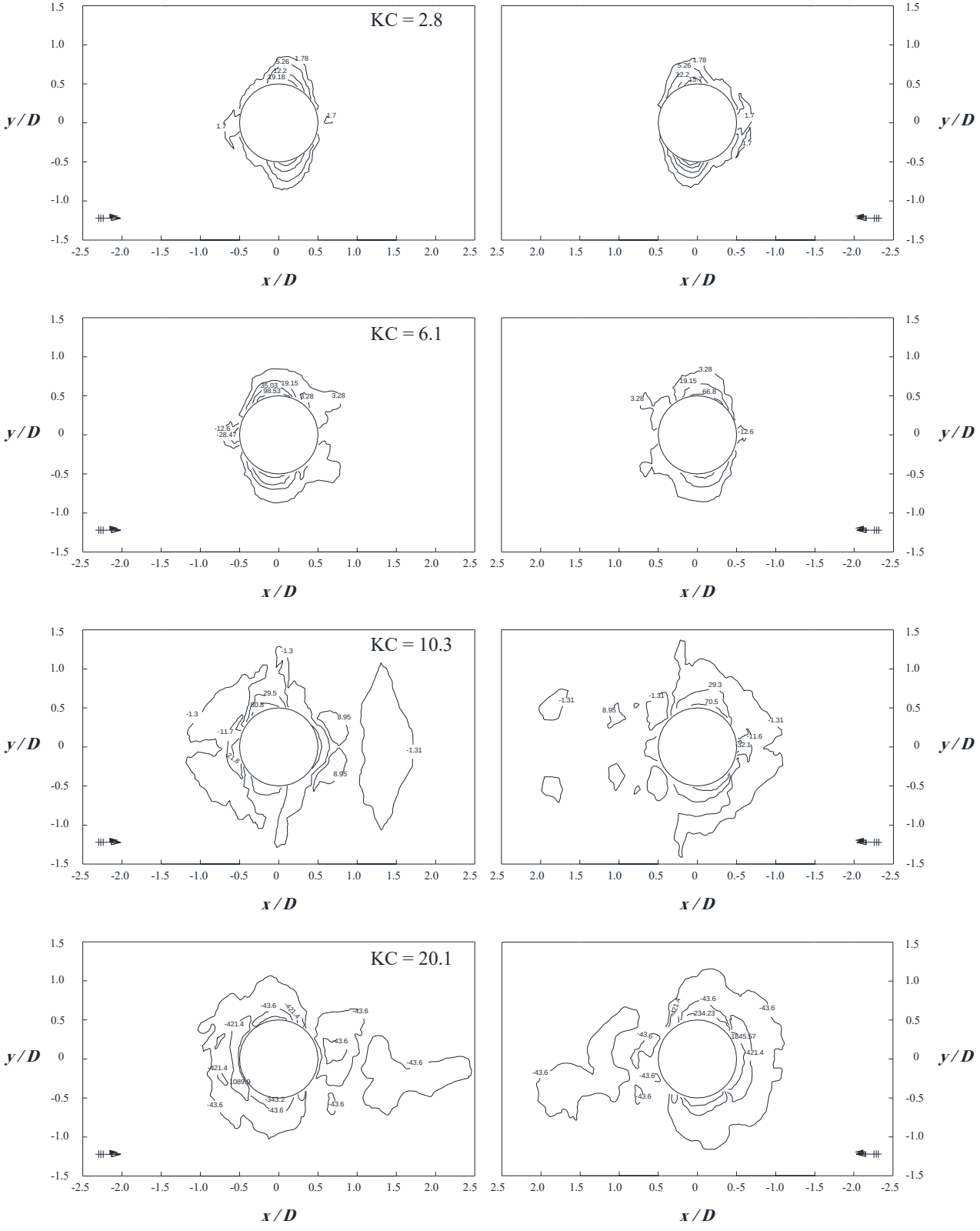

Figure 10. *Q* Criterion around the pile at the bottom of the wave tank at a selected instant of time ($\omega t = 90^{\circ}$ for the left-hand side pictures and $\omega t = 270^{\circ}$ for the right-hand side pictures)

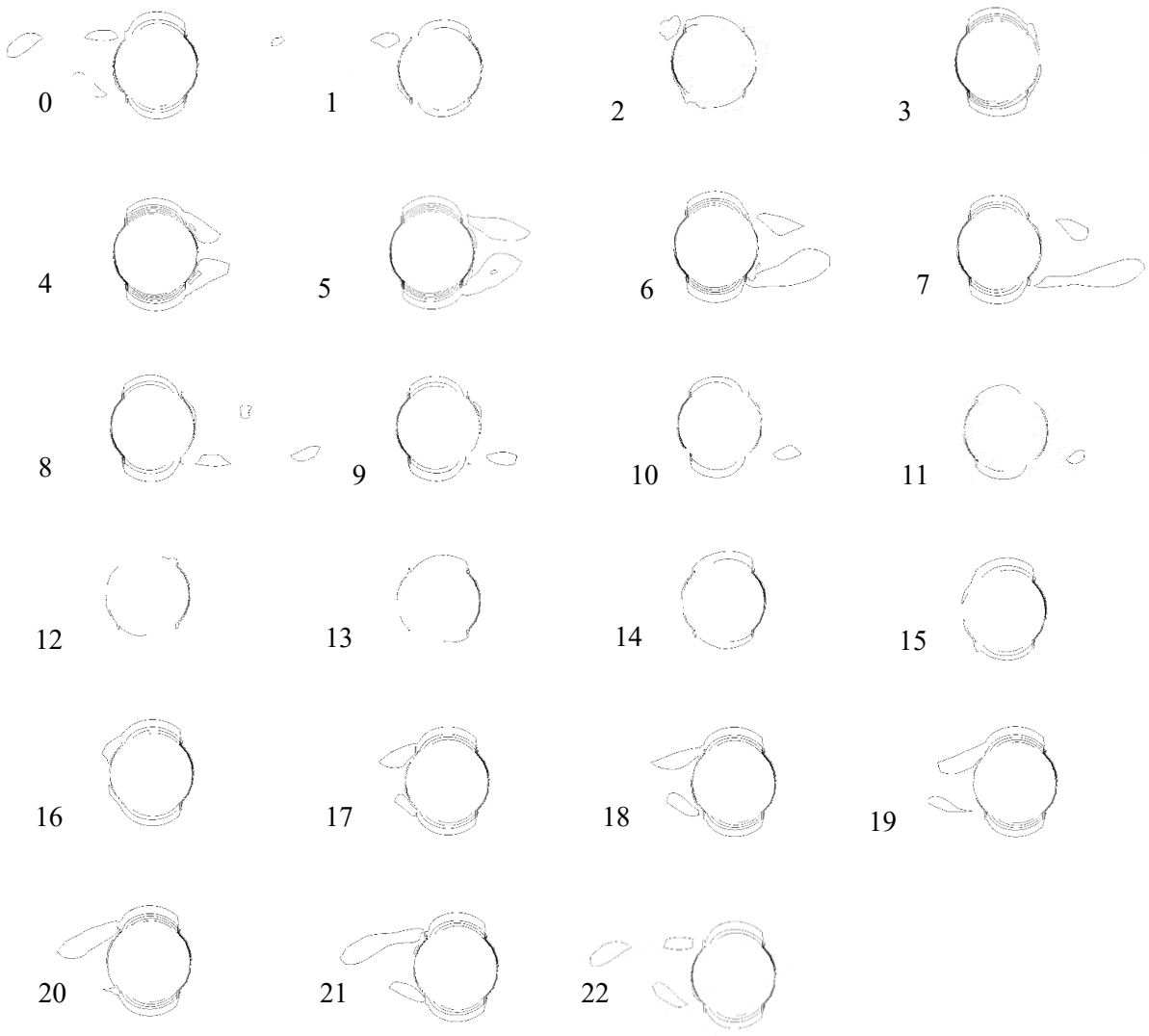

Figure 11. Vorticity snap shot during one wave period for case 4 (KC= 20.1)

In the figure, the pile is in the crest half-period at stage 0, and remaining vortices from previous stage in up-stream side are damped suddenly due to Cnoidal wave shape in crest half period. After a short while lee-wake vortices are generated and vortex shedding happened, from time stage 4. This is continuing to the flow direction changed and pile would be in trough half-period at stage 7. But, vortex shedding is still happening and vortices are being separated from the flow. Following the flow reversal, downstream vortices pushed back and hit on the pile, which is the main reason for existence of some disturbance in the total in-line force acting on pile in trough half-period. To comprehend more, variation of the total in-line force acting on pile for case 4 (KC= 20.1) corresponding to time stages of Figure 11 is depicted in Figure 12. Considering simultaneously both figures, the existence of small pick point in the trough half-period through time stage 7 to 11 is approved. This is happening up to time stage 12, when the vortex shedding is damped and the flow direction totally is changed. As seen from Figure 11, after that time the vortex shedding is reversal to the pile and the trend continues.

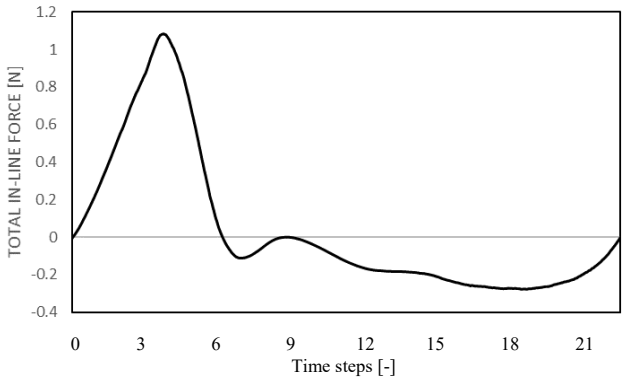

Figure 12. Total in-line force acting upon pile variation in one wave period for case 4 (KC=20.1)

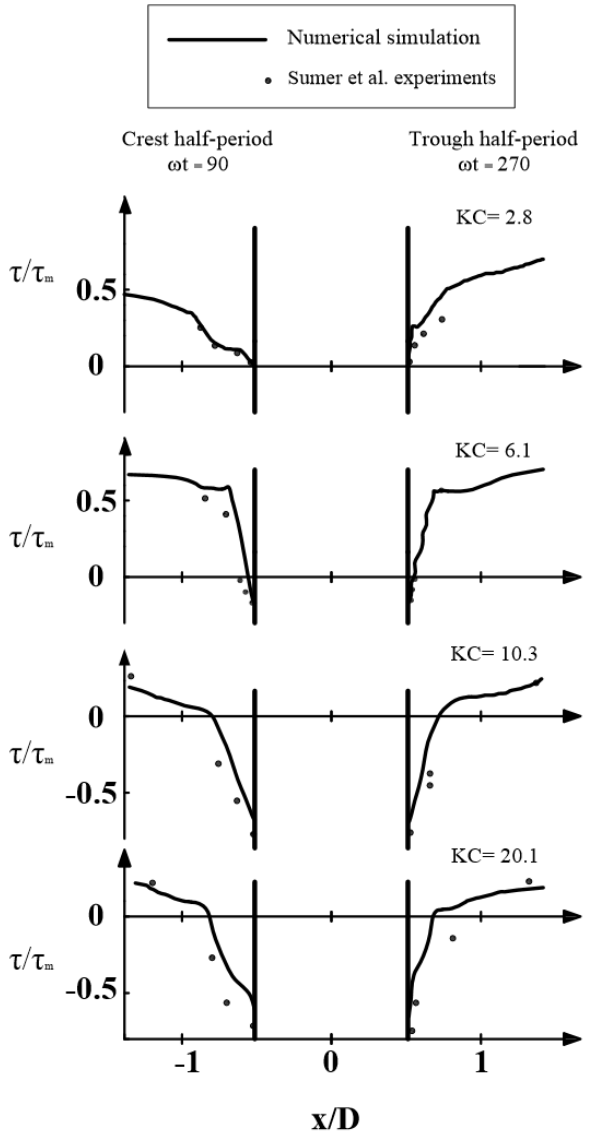

Figure 13. Variation of bed shear stress along x axes near the pile at crest half-period ($\omega t = 90^{\circ}$) and trough half-period ($\omega t = 270^{\circ}$) for all cases

Generation of horseshoe vortex around the pile affect the bed shear stress and consequently the sediment transport potential and scour around the pile. The numerical results showed that the bed shear stress increases with increasing KC, which can be consequence of the increased presence of the horseshoe vortices. The bed shear stress is expressed by means of amplification factor

$$\alpha = \frac{\tau}{\tau_{\infty}} \tag{13}$$

where τ refers to the bed shear stress and τ_{∞} is the bed shear stress for the undisturbed flow. Bed shear stress beneath the horseshoe vortex was investigated and it is concluded that when no negative bed shear stress near the pile exist, no horseshoe vortex exists either. The numerical model results are in line with Sumer et al. statement [1]. Figure 13 illustrates variation of bed shear stress along x axis near the pile at the crest half-period ($\omega t = 90^{\circ}$) and the trough half-period ($\omega t = 270^{\circ}$) for all cases. As seen, for Case 1 (KC=2.8) no horseshoe vortex formed as no negative bed shear stress existed for both wave phase, which is along with obtained results by investigating the vorticity and *Q* criterion. In Case 2 (KC= 6.1) the bed shear stress near the pile have some negative values, which is result of generating horseshoe vortices there. By increasing KC for Case 3 and 4 the magnitude of negative values of bed shear stress in vicinity of the pile increased, which implies the horseshoe vortices are completely formed.

5. Conclusions

Three-dimensional numerical simulation of regular waves passing over a cylindrical pile was carried out to investigate the hydrodynamic force acting on pile as well as vortex dynamics around that. The open-source CFD toolkit OpenFOAM, which combines the Eulerian multi-fluid approach, was applied to model the rectangular wave flume and monopile.

Some numerical results were compared to the experimental ones to validate the model e.g. water particle velocity at a wave gauge, the surface elevation at four wave gauges, the total in-line force acting on the pile and the time histories of dynamic pressure along the perimeter of the pile in six angular points.

Four cases with different KC number were modeled to investigate on hydrodynamic in-line force acting on pile and the vortex dynamics around the pile. The vorticity field around the pile was investigated as well as vortices by means of *Q* criterion. From the numerical investigation, the following conclusions are drawn:

- Variation of KC number has different impacts on the hydrodynamic in-line force acting on pile. That is, change in KC due to change in *T* did not significantly influence on the hydrodynamic in-line force acting on pile. While, it remarkably increased for increasing KC due to change in *H*.
- In vortex shedding regime, drag force component increased and inertia force component decreased.

- Some pick points in negative values of the total in-line force acting on the pile were seen, which can be due to vortex shedding behind the pile and consequently increasing of disturbance around that.
- The bed shear stress near the pile when KC >6 is negative which is the result of existence of horseshoe vortices. By increasing KC up to 20, the magnitude of negative values of bed shear stress near the pile increased which implies horse shoe vortices were completely formed.

6. References

1- Sumer, B. M., Christiansen, N., & Fredsøe, J. (1997). The horseshoe vortex and vortex shedding around a vertical wall-mounted cylinder exposed to waves. *Journal of Fluid Mechanics*, *332*, 41-70.

2- Iwagaki, Y., & Ishida, H. (1976). Flow separation, wake vortices and pressure distribution around a circular cylinder under oscillatory waves. *Coastal Engineering Proceedings*, *1*(15).

3- Morgan, G. C. J., Zang, J., Greaves, D., Heath, A., Whitlow, C., & Young, J. (2011). Using the rasInterFoam CFD model for wave transformation and coastal modelling. *Coastal Engineering Proceedings*, *1*(32), 23.

4- Amini Afshar, M. (2010). Numerical wave generation in Open FOAM®.

5- Baykal, C., Sumer, B. M., Fuhrman, D. R., Jacobsen, N. G., & Fredsøe, J. (2015). Numerical investigation of flow and scour around a vertical circular cylinder. *Philosophical Transactions of the Royal Society of London A: Mathematical, Physical and Engineering Sciences*, *373*(2033), 20140104.

6- oM, W., Irschik, K., Oumeraci, H., & Liu, P. L. F. (2007). A 3D numerical model for computing non-breaking wave forces on slender piles. *Journal of Engineering Mathematics*, *58*(1), 19-30.

7- Jacobsen, N. G., Fuhrman, D. R., & Fredsøe, J. (2012). A wave generation toolbox for the open-source CFD library: OpenFoam®. *International Journal for Numerical Methods in Fluids*, *70*(9), 1073-1088.

8- Benitz, M. A., Schmidt, D. P., Lackner, M. A., Stewart, G. M., Jonkman, J., & Robertson, A. (2014, June). Comparison of hydrodynamic load predictions between reduced order engineering models and computational fluid dynamics for the oc4-deepcwind semi-submersible. In *ASME 2014 33rd International Conference on Ocean, Offshore and Arctic Engineering* (pp. V09BT09A006-V09BT09A006). American Society of Mechanical Engineers.

9- Higuera, P., Lara, J. L., & Losada, I. J. (2013). Simulating coastal engineering processes with OpenFOAM®. *Coastal Engineering*, *71*, 119-134.

10- Paulsen, B. T., Bredmose, H., & Bingham, H. B. (2014). An efficient domain decomposition strategy for wave loads on surface piercing circular cylinders. *Coastal Engineering*, *86*, 57-76.

11- Stahlmann, A. (2013, June). Numerical and experimental modeling of scour at foundation structures for offshore wind turbines. In *The Twenty-third International Offshore and Polar Engineering Conference*. International Society of Offshore and Polar Engineers.

12- Paulsen, B. T., Bredmose, H., Bingham, H. B., & Jacobsen, N. G. (2014). Forcing of a bottom-mounted circular cylinder by steep regular water waves at finite depth. *Journal of fluid mechanics*, *755*, 1-34.

13- Jiang, C., Yao, Y., Deng, Y., & Deng, B. (2015). Numerical Investigation of Solitary Wave Interaction with a Row of Vertical Slotted Piles. *Journal of Coastal Research*, *31*(6), 1502-1511.

14- Haddorp, R. (2005). Predictability of Scour at Large Piles due to Waves and Currents.

15- Sumer, B. M. (2002). *The mechanics of scour in the marine environment* (Vol. 17). World Scientific Publishing Company.

16- Hoffmans, G.J.C.M., Verheij, H.J. (1997): "Scour Manual", Rotterdam.

17- Coastal Engineering Manual (2003): "EM 1110-2-1100 (Part VI) ", Chapter 5, p.242-245, Washington.

18- Isaacson, M. (1979). Wave-induced forces in the diffraction regime. *Mechanics of wave-induced forces on cylinders*.

19- Menter, F. R. (1994). Two-equation eddy-viscosity turbulence models for engineering applications. *AIAA journal*, *32*(8), 1598-1605.

20- WILCOX, D. (1988). Reassessment of the scale-determining equation for advanced turbulence models. *AIAA journal*, *26*(11), 1299-1310.

21- Hirt, C. W., & Nichols, B. D. (1981). Volume of fluid (VOF) method for the dynamics of free boundaries. *Journal of computational physics*, *39*(1), 201-225.

22- Jacobsen, N. G. (2017). waves2Foam Manual.

23- OS, D. (2011). J101, Design of Offshore Wind Turbine Structures. *DET NORSKE VERITAS AS, Ausgabe*, *9*.

24- Chen, Q., Zhong, Q., Qi, M., & Wang, X. (2015). Comparison of vortex identification criteria for planar velocity fields in wall turbulence. *Physics of Fluids*, *27*(8), 085101.

25- Sumer, B. M. (2006). *Hydrodynamics around cylindrical structures* (Vol. 26). World scientific.

INTERNATIONAL JOURNAL OF
COASTAL & OFFSHORE ENGINEERING
IJCOE Vol.3 /No. 4/Winter 2018 (13-20)

Available online at: http://ijcoe.org/browse.php?a_code=A-10-139-2&sid=1&slc_lang=en

Investigation of Infragravity Waves Dependency on Wind Waves for Breaking and Nonbreaking Conditions in the Sandy Beaches of Southern Caspian Sea (Nowshahr Port)

Seyed Masoud Mahmoudof

Assistant Professor, Iranian National Institute for Oceanography and Atmospheric Science (INIOAS), Tehran, IRAN; m_mahmoudof@inio.ac.ir

ARTICLE INFO

Article History:
Received: 3 Feb. 2018
Accepted: 17 Mar. 2018

Keywords:
Caspian Sea
Infragravity waves
Swell and sea separation
Energy dependency
Field measurements

ABSTRACT

In this study, the evolution and dependency of infragravity waves (IGWs) on wind waves for breaking and nonbreaking conditions is separately investigated. The efficiency of two constant cutoff frequencies (0.125 and 0.14 Hz) is compared for wave data measured in the sandy beaches of Nowshahr at the Southern Caspian Sea. It is found that the frequency of 0.125 Hz results higher correlation coefficients between IGWs energy content and two wind wave groups. Two pair different correlation patterns between IGWs in one side and wind waves higher and lower than 0.125 Hz in another side were recognized for breaking and nonbreaking conditions. It can be concluded that the IGWs excitation is controlled by the frequency distribution of wind wave energy.
According to 0.125 Hz as more successful option, the correlation of IGWs with swell waves is generally more significant than sea waves. In the nonbreaking wave condition, the IGWs are well correlated with sea waves, whereas no considerable correlation between IGWs and sea waves is found in the breaking condition. It is resulted that IGWs energy is approximately linearly proportional of both swell and sea waves in nonbreaking condition. In the high and moderate conditions of incident wave energy, the density of IGWs energy grows shoreward, while energy attenuation can be detected for IGWs in very low energy waves.

1. Introduction

Low frequency or infragravity waves (IGWs) are more significant in the coastal zones. Several studies focused on this type of long waves (1-3). The importance of IGW is well understood in the nearshore shallow waters. The sediment transport pattern and incident wave field can be influenced by IGW, strongly. Also, shoreline erosion, sand bar formation and specific morphology can be pointed out as the consequent phenomena of these long waves.
The correlation of low frequency wave energy to higher harmonics and generation of this type of waves by shorter waves (swell and/or sea waves) was demonstrated by several studies (4-6).
In this paper, the correlation of IGW energy content with wind wave groups is observationally investigated in the sandy beaches of Nowshahr port. The Field data were included water level fluctuations measured near the shore. In section 2, the previous studies due to low frequency waves dependency on wind waves are reviewed. In the next section the field data campaign and analytical specifications are presented. The results are discussed in section 4 and the study is finally summarized in the last section.

2. Background and Previous Studies

Infragravity waves are impressive on many shallow water processes. The various consequent effects of IGWs were investigated by means of field measurements, laboratory observations and numerical modelling (7-12).
This type of low frequency waves was firstly observed by Munk (13) and named surf beat. Tucker (14) as an example pointed out that the infragravity waves energy level was correlated with short wave energy content. Ruessink (15) concluded that IGWs are locally generated by incident short waves.
As waves propagate shoreward, two main processes arise. The first is shoaling occurred before wave breaking for low and moderate wave energy condition. The consequent nonlinearity enhancement during shoaling increases the bound IGWs energy as a result of difference nonlinear wave by wave interactions. The

second process is wave breaking during high energy condition. In this process, the swell and sea waves energy dissipates dramatically and random group wave breaking releases the bound IGWs as free long waves (16-18). Therefore, it is expected that the dominance of bound IGWs during a moderate energy level, replaces to free one during energetic waves and sever breaking in the surf zone. Both of these two types of IGWs were recorded and reported by field measurements and experimental studies (3, 6, 15, 19, 20). The released IGWs harmonics are reflected by the shore line and propagate seaward direction. The leaky and edge waves are two types of subsequent phenomena of this process. Several studies were planned to illustrate the correlation of two IGW groups energy to higher frequency bands energy for different wave conditions (4-6, 15). Therefore, the separation and classification of waves seems important and impressive from this aspect.

Okihiro, Guza (21) recommended the 0.04 Hz frequency as the threshold between IGWs and swell to ensure that IGWs content were not contaminated by long-period swell. Elgar, Herbers (4) selected the 0.004-0.04 Hz frequency band for IGWs range, 0.14 Hz and 0.30 Hz as the constant swell-sea separation frequency and upper wind wave limit, respectively. Herbers, Elgar (5, 22) considered the range of 0.005-0.05 Hz as the IGWs frequency band. These criteria were sometimes similar or dissimilar in other studies. Brander, Kench (23) and Ogawa (24) supposed that IGWs frequency band ranges up to 0.05 Hz, as well as, swell energy distributes in band of 0.05-0.125 Hz and sea waves range is in the frequency band of 0.125-0.33 Hz.

The wave energy of each group is proportional to the integration of energy density variance spectrum on each frequency band $\left(E_{f_1-f_2} \propto \int_{f_1}^{f_2} S(f)df\right)$. Elgar, Herbers (4) found that the IGWs energy is more correlated with swell waves than sea waves. They reported the linear proportionality of total IGWs energy to swell waves. In that study, the wind waves were separated to swell and sea groups, but the wave condition (breaking or nonbreaking) was not emphasized. Ruessink (6) pointed out that the total IGWs energy is linearly correlated to wind waves (swell or sea 0.04 – 0.33 Hz), while this correlation for bound IGWs is quadratic. Ruessink (6) did not classify wind waves to swell and sea separately and the wave condition was not underscored in Ruessink (15), may be due to studied intermediate water depth stations. Herbers, Elgar (5) evaluated the dependency of IGWs on swell and abandoned sea waves. Based on previous studies, it seems that the dependency and correlation of IGWs with swell and sea waves for breaking and nonbreaking wave conditions can be separately studied in details.

3. Field Measurements and Data Analysis

Field data acquisition was including the water level fluctuations measurements on a shore perpendicular transect located on the western sandy beaches of Nowshahr Port in the southern Caspian Sea (Figure 1). In the studied area, tidal level variation is negligible and less than 10 cm.

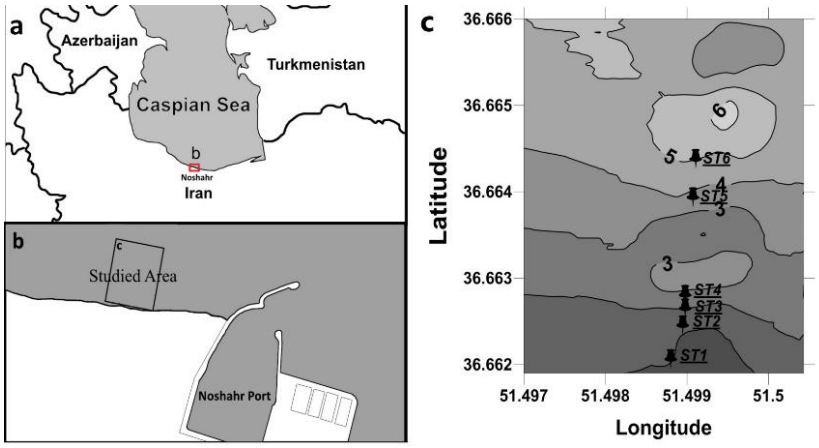

Figure 1. Location of Nowshahr in the Southern Caspian Sea, b) Nowshahr Port and the study area, c) Bathymetry of the studied area (31)

Wave data were recorded by using six synchronized pressure sensors deployed within the near shore zone as depicted in Figure 2. Bathymetry of the studied area was surveyed using a single beam echo-sounder in the beginning and end of the field campaign, which showed inconsiderable changes during the measurement period. The beach profile and the location of data gathering stations are depicted in Figure 2. Bottom profile exhibits a single bar system which has a seaward slope of ~0.025.

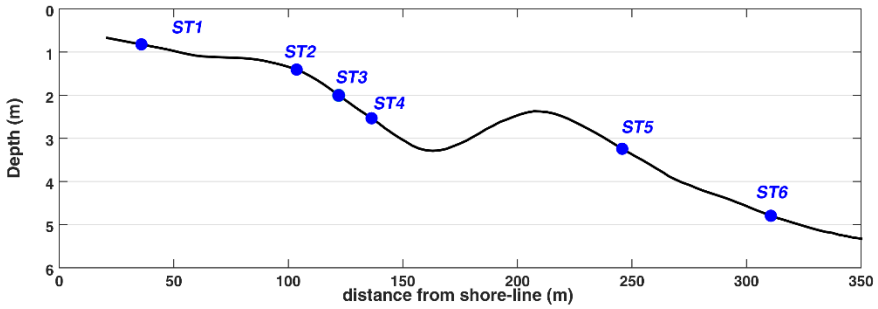

Fig. 2. Beach profile and the position of measurements in the transect

The instrumentation details are shown in Table 1. Wave data were continuously recorded in ST1, ST2, and ST6 while in ST3, ST4 and ST5 because of low data logger capacity, data retrieval was necessary after a period of two-day measurement. Therefore, the acquisition was interrupted and including of three couples of days at ST3, ST4 and a single couple of days at ST5. The sampling rate was set to 4Hz at ST1, ST2 and 2Hz at ST6, while this rate at other stations was 1Hz.

Table 1. Details of instrumentation including sampling rate, depth and distance from shore for each station

Stations	Instrument	Sampling rate	Depth (m)	Distance from shore (m)	Duration
ST1	RBRvirtuoso	4 Hz	0.8	35	3/4/2014– 3/16/2014 (continuously)
ST2	RBRvirtuoso	4 Hz	1.4	103	3/4/2014– 3/16/2014 (continuously)
ST3	DST-centi Star-Oddi	1 Hz	2.0	120	3/5/2014–3/7/2014, 3/9/2014–3/11/2014, 3/12/2014–3/14/2014
ST4	DST-centi Star-Oddi	1 Hz	2.5	135	3/5/2014–3/7/2014, 3/9/2014–3/11/2014, 3/12/2014–3/14/2014
ST5	DST-centi Star-Oddi	1 Hz	3.2	245	3/5/2014–3/7/2014
ST6	ADCP	2 Hz	4.8	310	3/3/2014– 3/16/2014(continuously)

Two non-locally generated storms (approximately 600 km far from the study area, according to MetOcean data, http://www.bocmetocean.com/forecast_maps.php) passed over the study area during the measurement period. It should be noted that no wave breaking was observed for offshore waves till ST6 in the total period of the measurements. More details of instrumentation, measurements, field specifications and observations can be found in Mahmoudof, Badiei (25).

The depth attenuation correction was applied for all pressure sensors. For two shallower stations (ST1 and ST2), 4096 data of water level corresponding to each 17.07-minute burst were detrended and divided into 512-point segments with 50% overlap to produce the wave spectrum with approximately 32 degrees of freedom (d.o.f.). Then, spectral analysis was performed for each 128 second duration segment data and spectra were averaged for all segments of each burst. The resulted spectrum frequency resolution was $\Delta f = 0.0078 Hz$. The similar process method was implemented for ST3, ST4, ST5 and ST6, except that each burst data was divided into 128-point segment for first three stations and 256-point for ST6 because of the slower sampling rate.

Based on resulted spectra, other spectral characteristics were achieved. For the present study objectives, it is supposed that IGWs range from 0.004 up to 0.05 Hz (similar to (5) and (22)) and upper limit of wind waves is 0.35 Hz. But the swell and sea separation threshold is investigated according to two constant frequencies of 0.125 and 0.14 Hz. The energy of each wave group is calculated as

$$E_{IGWs} \approx \int_{0.005Hz}^{0.05Hz} S(f)df \quad (1)$$

$$E_{swell} \approx \int_{0.05Hz}^{f_s} S(f)df \quad (2)$$

$$E_{sea} \approx \int_{f_s}^{0.35Hz} S(f)df \quad (3)$$

where f_s is the separation frequency of sea and swell waves.

4. Results and discussion

Time series of significant wave height at ST1, ST2 and ST6 are illustrated in Figure 3. It is clear that two storms with maximum significant wave heights of approximately 1.4m and duration of 16 and 29 hours were occurred in the study area. The peak periods of both were about 9.5s. It can be found that the dissipation and wave breaking were dominant shoreward direction from 03/08/2014 5:00 to 03/09/2014 12:00 and 03/13/2014 4:00 to 03/14/2014 12:00. In the following, the correlation between IGWs energy and wind waves was evaluated similar to earlier studies (4-6, 15). This evaluation is separately performed for swell and sea wave groups in the breaking and nonbreaking conditions.

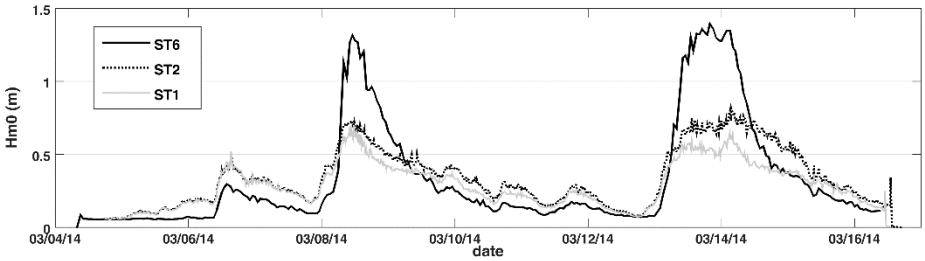

Figure 3. Time series of significant wave height at ST1 (solid-bright), ST2 (dotted) and ST6 (solid-dark)

In the present study, the fitted proportionality between IGWs and two wind wave groups energy are evaluated by means of relation $E_{IGWs} \propto E^{m}_{sea/swell}$, where $E_{sea/swell}$ is the energy density of sea or swell waves. The exponent *m* (slope) clarifies the dependency type (linear or quadratic) of IGWs energy on higher harmonics. Also, the correlation of IGWs energy with swell and sea is investigated by means of two aforementioned constant separation frequencies. For both of cutoffs, ~3200 bursts were analyzed and evaluated in the study area, totally. The resulted correlation coefficients and exponent *m* are presented in tables 2 and 3 for both cutoffs. It is obvious that the *m* value is vague and not meaningful for categories with low correlation coefficients. These exponent coefficients are shadowed in the resulted tables.

Table 2. The IGWs dependency on swell and sea separation based on constant frequency of 0.125 Hz

		Swell		Sea	
		Breaking	*Nonbreaking*	*Breaking*	*Nonbreaking*
Correlation Coefficients	ST6	-	0.94	-	0.84
	ST5	-	0.89	-	0.85
	ST4	0.79	0.88	0.58	0.83
	ST3	0.78	0.86	0.52	0.84
	ST2	0.80	0.93	0.30	0.94
	ST1	0.78	0.94	0.02	0.95
Slope (*m*)	ST6	-	0.69	-	0.92
	ST5	-	1.19	-	0.80
	ST4	0.62	1.26	1.57	0.90
	ST3	0.63	1.27	1.57	0.97
	ST2	0.88	1.13	2.33	1.64
	ST1	1.35	1.17	0.70	1.70

Table 3. The IGWs dependency on swell and sea separation based on constant frequency of 0.14 Hz

		Swell		Sea	
		Breaking	*Nonbreaking*	*Breaking*	*Nonbreaking*
Correlation Coefficients	ST6	-	0.92	-	0.79
	ST5	-	0.89	-	0.85
	ST4	0.78	0.85	0.51	0.83
	ST3	0.77	0.82	0.44	0.84
	ST2	0.78	0.91	0.17	0.93
	ST1	0.88	0.94	0.39	0.89
Slope (*m*)	ST6	-	0.64	-	0.96
	ST5	-	1.10	-	0.80
	ST4	0.64	1.02	1.57	0.90
	ST3	0.64	1.05	1.55	0.97
	ST2	1.12	1.18	1.69	1.65
	ST1	1.10	1.20	3.07	2.07

Both separation frequencies exhibit two different types of correlation and dependency trends of IGWs energy on the swell and sea waves, especially for breaking waves. It means that including swell and sea waves energy into a single group of wind wave (such as Ruessink (6)) is not well-advised. Some of the results can be ambiguous as a result of neglecting this hint. Therefore, it is necessary to evaluate the correlation and dependency of IGWs formation on the sea and swell waves, separately.

Based on the correlation coefficients resulted by constant frequency of 0.125 and 0.14 Hz (Tables 2 and 3, respectively), it can be derived that the correlation of IGWs energy with both of swell and sea groups is more significant in the nonbreaking than breaking condition. Normally, it is expected that free IGWs are more dominant in the breaking condition. Therefore, it can be concluded that the dependency of bound IGWs on wind waves is more significant than free ones'. This outcome is consistent with the results presented in Table 1 in Ruessink (6). Also, it is perceptible that the IGWs are slightly more correlated with swell than sea in nonbreaking condition. It is consistent with lower

correlation coefficients for sea waves in Elgar, Herbers (4) and Ruessink (15).

In Tables 2 and 3, it is demonstrated that the IGWs energy is well correlated with sea wave energy for nonbreaking waves. Unlikely, no remarkable correlation can be reported between IGWs and sea waves for breaking condition. This result was indirectly reported by Ruessink (6).No line was fitted for IGWs energy versus Ess (the total energy of swell and sea waves) in that paper for breaking waves.

Considering two constant method results for exponent *m*, it can be resulted that the IGWs energy is approximately linearly proportional of swell energy for nonbreaking condition. In this condition, the exponent values varied 1.02~1.27, except ST6. This finding is reliable for sea waves in nonbreaking condition for ST3 to ST6, too (the m varies between 0.80 and 0.97). The increment of exponent *m* at very shallow water (ST1 and ST2) for nonbreaking wave condition can be interpreted as the nonlinearity enhancement and bound IGWs growth as a result of depth reduction and wave shoaling. This finding is consistent with the bound wave theory (16). As well as, the increment of exponent of *m* for swell waves is clear in the breaking condition. But this finding can be explained as a result of released IGWs growth due to random wave breaking. The best method to clarify the proportional bound and free IGWs is Bispectral analysis (16, 17), which is not in the present study scope.

However, the constant frequency 0.125 Hz is slightly more accurate than 0.140 for the studied area. The dependency of IGWs energy on swell and sea waves at all stations for breaking and nonbreaking conditions is depicted in Figures 4 to 7, resulted from 0.125 Hz cut-off. Taking account into the 0.125 Hz as the more appropriate separation frequency, the evolution of IGWs is studied across the shore. The percentage of each wave group (IGW, swell and sea) was estimated for three stations (ST1, ST2 and ST6) where the data acquisition was continuous. It is depicted in Figure 8 that the percentage of IGWs energy is negligible during all of the field measurements period at ST6. Coincident with the storm peaks the contribution of swell and sea energy was approximately 50% at this station. From ST6 to shoreline the relative dissipation of swell waves was more serious than sea waves during storms, then the swell percentage energy was diminished at ST2.

In Figures 8 and 9, it can be observed that the IGWs energy grew across the shore as the high and moderate energetic waves passed through the surf-zone. The relative IGWs energy amplification is concurrent with relative sea descent in ST1 during the storms. However, both of swell and sea wave groups were absolutely dissipated across the shore for breaking wave condition (Figure 9b and 9c).

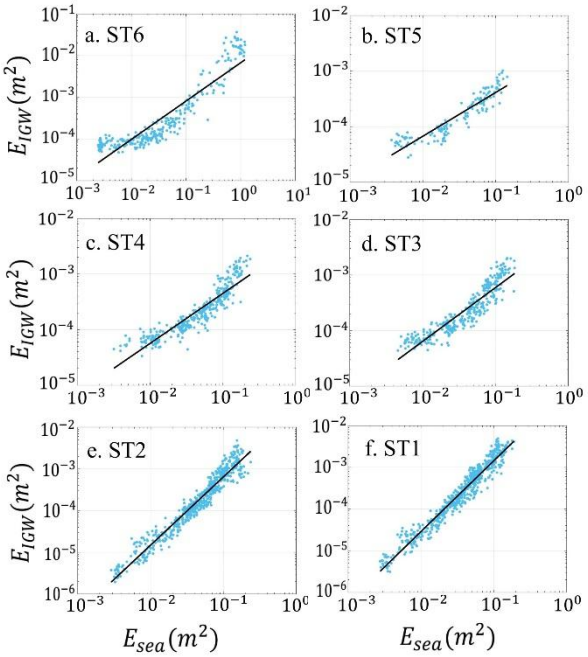

Figure 4. Correlation of IGWs with sea waves for nonbreaking condition

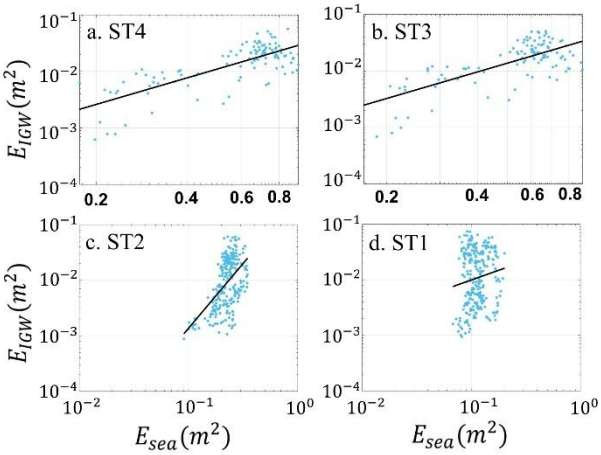

Figure 5. Correlation of IGWs with sea waves for breaking condition

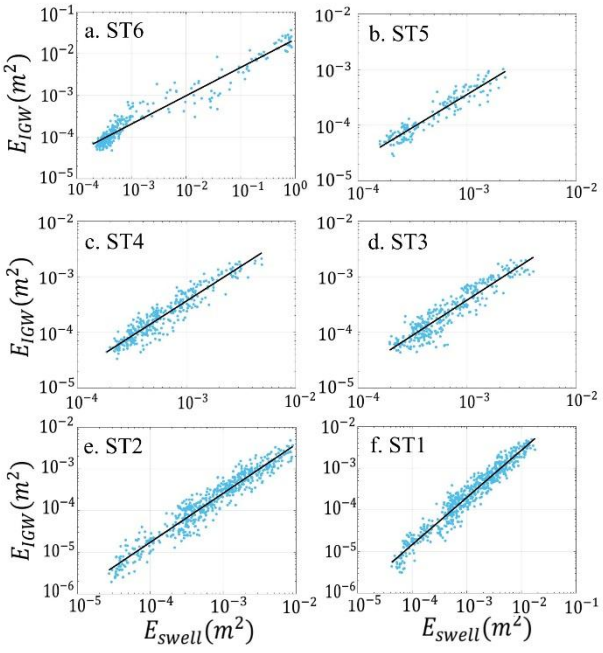

Figure 6. Correlation of IGWs with swell waves for nonbreaking condition

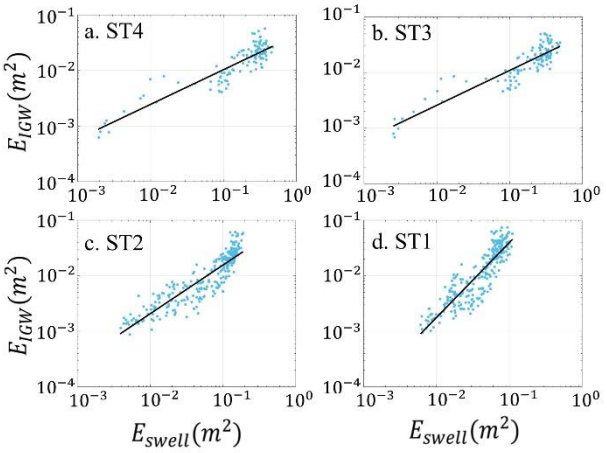

Figure 7. Correlation of IGWs with swell waves for breaking condition

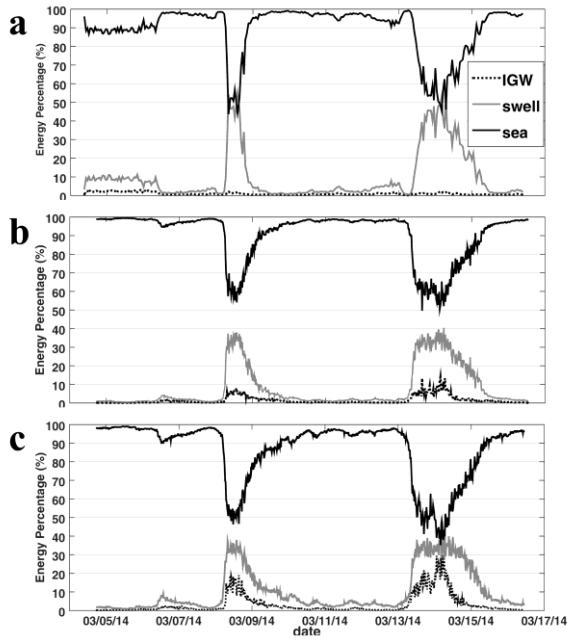

Figure 8. The percentage of each waves group energy at: a) ST6; b) ST2 and c) ST1.

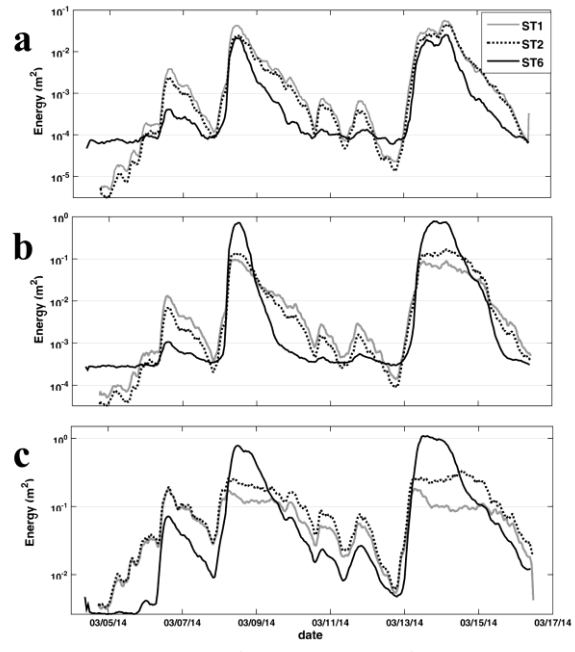

Figure 9. The evolution of each wave group from ST6 till ST1: a) IGWs; b) swell waves; c) sea waves.

In Figure 9a the IGWs attenuation can be observed for very low energy condition of incident waves. Several possible mechanisms have been reported for IGWs decay near the shore. The first guilty phenomena for this event is bottom friction, especially on rough gravel or coral reef bottoms (26). But on the fine sandy beaches, it seems that the bottom friction is the secondary responsible mechanism (27, 28). Several studies reported that nonlinear energy transfer back to the primary wind waves energy can be regarded as the key factor for IGWs attenuation on steep beaches (29, 30). On the gently sloping beaches with IGWs dominancy climate, the nonlinear triad interactions between very long IGWs can result in steepening shorter IGWs and thus the breaking of these type of IGWs losses considerable energy content (27, 29, 30). However, considering the above explanations and in-situ observational evidences, it seems that the IGWs decay for very low wave energy content illustrated in Figure 9a is a result of bottom friction.

5. Conclusion

In this study, the evolution and dependency of Infragravity waves (IGWs) on swell and sea waves on a sandy beach at the west of Nowshahr Port in the southern coasts of Caspian Sea was separately investigated. The wave gauges were deployed at 6 stations on a shore perpendicular transect. The recorded storms were originally generated more than 600 km far away from the studied area in the central part of Caspian Sea. The significant wave height of observed storms was more than 1.3m and peak periods were approximately 9.5s.

The swell and sea wave groups were separated according to two constant cutoff frequencies of 0.125 and 0.14 Hz.

The spectral analysis was accomplished for about 3200 bursts with 17.07-minute duration. The energy of each wave group was evaluated by integrating the energy variance density ranged between 0.004-0.05 Hz as IGWs, 0.05-fs and fs-0.35 as swell and sea waves, respectively. The correlations and dependencies of IGWs energy on swell and sea energy resulted from each cutoff frequencies were separately evaluated in the breaking and nonbreaking conditions. Both of cutoffs present high correlation coefficients. This outcome implies that the IGWs energy excitation is controlled by frequency distribution of wind wave energy. By means of both separation cutoffs, different correlation patterns between IGWs and two wind wave groups has been resulted. It can be concluded that the including swell and sea waves in one wind wave group to predict the dependent IGWs energy is not advised and two wind wave groups must be separated.

The frequency of 0.125 Hz resulted slightly higher correlation coefficients and showed more reliable predictability of IGWs based on swell and sea energy

distribution in the studied area. For nonbreaking waves, the correlation of IGWs with swell and sea is very robust. In the breaking condition, the dependency of IGWs on sea waves is negligible while the IGWs are considerably dependent on swell waves. However, the dependency of IGWs on swell waves is generally more significant than sea waves. The IGWs energy showed a linear proportionality with both swell and sea waves for nonbreaking waves.

The general investigations revealed that the IGWs energy density increased in the shoreward direction in the moderate and high energy wave condition due to nonlinearity enhancement (result of shoaling) and wave breaking, respectively. In during of very low energy level, the IGWs dissipation was observed as a possible bottom friction consequence.

Acknowledgment

The author is thankful for M. Jafari for his assistance in the field measurements. Special thanks for M. Allahyar and the Ports and Maritime Organization for their field measurement supports.

References

1- Sheremet A., Guza R., Elgar S., Herbers T., (2002*), Observations of nearshore infragravity waves: Seaward and shoreward propagating components*. Journal of Geophysical Research: Oceans. Vol.107(C8).

2- Battjes J., Bakkenes H., Janssen T., Van Dongeren A., (2004), *Shoaling of subharmonic gravity waves*. Journal of Geophysical Research: Oceans., Vol.109(C02009).

3- Baldock T., Huntley D., (2002), *Long–wave forcing by the breaking of random gravity waves on a beach*. Proceedings of the Royal Society of London A: Mathematical, Physical and Engineering Sciences: The Royal Society; p. 2177-2201.

4- Elgar S., Herbers T., Okihiro M., Oltman-Shay J., Guza R., (1992), *Observations of infragravity waves.* Journal of Geophysical Research. Vol.97: 15573-15577.

5- Herbers T., Elgar S., Guza R., O'Reilly W., (1995), *Infragravity-frequency (0.005–0.05 Hz) motions on the shelf. Part II: Free waves.* Journal of Physical Oceanography. Vol. (25): 1063-1079.

6- Ruessink B., (1998), *Bound and free infragravity waves in the nearshore zone under breaking and nonbreaking conditions*. Journal of Geophysical Research: Oceans. Vol. (103): 12795-805.

7- Aagaard T., Bryan K.R., (2003), *Observations of infragravity wave frequency selection.* Continental Shelf Research. Vol. (23): 1019-1034.

8- Luick J.L., Hinwood J.B., (2008), *Water levels in a dual-basin harbour in response to infragravity and edge waves.* Progress in Oceanography. Vol. (77): 367-375.

9- Guerrini M., Bellotti G., Fan Y., Franco L., (2014), *Numerical modelling of long waves amplification at Marina di Carrara Harbour*. Applied Ocean Research. Vol. (48): 322-330.

10- López M., Iglesias G., (2014), *Long wave effects on a vessel at berth*. Applied Ocean Research. Vol. (47): 63-72.

11- Inch K., Davidson M., Masselink G., Russell P., (2017), *Observations of nearshore infragravity wave dynamics under high energy swell and wind-wave conditions*. Continental Shelf Research. Vol. (138): 19-31.

12- Diaz-Hernandez G., Mendez F.J., Losada I.J., Camus P., Medina R., (2015), *A nearshore long-term infragravity wave analysis for open harbours*. Coastal Engineering. Vol. (97): 78-90.

13- Munk W.H., (1949), *Surf beats*. Trans Am Geophys Union. Vol. (30): 849–854.

14- Tucker M., (1950), *Surf beats: sea waves of 1 to 5 min. period*. Proceedings of the Royal Society of London A: Mathematical, Physical and Engineering Sciences: The Royal Society; p. 565-73.

15- Ruessink B., (1998), *The temporal and spatial variability of infragravity energy in a barred nearshore zone*. Continental Shelf Research. Vol. (18): 585-605.

16- Hasselmann K., (1962), *On the non-linear energy transfer in a gravity-wave spectrum Part 1*. General theory. Journal of Fluid Mechanics. Vol. (12): 481-500.

17- Longuet-Higgins M.S., Stewart R., (1962), *Radiation stress and mass transport in gravity waves, with application to 'surf beats'*. Journal of Fluid Mechanics. Vol. (13): 481-504.

18- Masselink G., (1995), *Group bound long waves as a source of infragravity energy in the surf zone.* Continental Shelf Research. Vol. (15): 1525-1547.

19- Baldock T., (2006), *Long wave generation by the shoaling and breaking of transient wave groups on a beach*. Proceedings of the Royal Society of London A: Mathematical, Physical and Engineering Sciences: The Royal Society; p. 1853-1876.

20- Lin Y-H., Hwung H-H., (2012), *Infra-gravity wave generation by the shoaling wave groups over beaches.* China Ocean Engineering. Vol. (26): 1-18.

21- Okihiro M., Guza R., Seymour R., (1992), *Bound infragravity waves*. DTIC Document.

22- Herbers T., Elgar S., Guza R., (1994), *Infragravity-frequency (0.005-0.05 Hz) motions on the shelf. Part I: Forced Waves*. Journal of Physical Oceanography. p. 917-927.

23- Brander R.W., Kench P.S., Hart D., (2004), *Spatial and temporal variations in wave characteristics across a reef platform, Warraber Island, Torres Strait, Australia*. Marine Geology. Vol. (207):169-184.

24- Ogawa H., (2013), *Observation of wave transformation on a sloping type B shore platform under wind-wave and swell conditions*. Geo-Marine Letters. Vol. (33): 1-11.

25- Mahmoudof S.M., Badiei P., Siadatmousavi S.M., Chegini V., (2016), *Observing and estimating of intensive triad interaction occurrence in very shallow water*. Continental Shelf Research. Vol. (122): 68-76.

26- Henderson S.M., Bowen A., (2002), *Observations of surf beat forcing and dissipation.* Journal of Geophysical Research: Oceans. 107.

27- De Bakker A.T.M., Tissier M.F.S., Ruessink B.G., (2014), *Shoreline dissipation of infragravity waves.* Continental Shelf Research. Vol. (72): 73-82.

28- Van Dongeren A., Battjes J., Janssen T., Van Noorloos J., Steenhauer K., Steenbergen G., Reniers A., (2007), *Shoaling and shoreline dissipation of low-frequency waves.* Journal of Geophysical Research. Vol. (112), C02011.

29- De Bakker A.T.M., Tissier M.F.S., Ruessink B.G., (2016), *Beach steepness effects on nonlinear infragravity-wave interactions: a numerical study*. Journal of Geophysical Research. Vo. (121): 554-570.

30- Guedes R.M.C., Bryan K.R., Coco G., (2013), *Observations of wave energy fluxes and swash motions on a low-sloping, dissipative beach*. Journal of Geophysical Research. Vol. (118): 3651-3669.

INTERNATIONAL JOURNAL OF
COASTAL & OFFSHORE ENGINEERING IJCOE Vol.3 /No. 4/Winter 2018 (21-26)

Available online at: http://ijcoe.org/browse.php?a_code=A-10-171-1&sid=1&slc_lang=en

Simulating the Pattern of Pollutant Emission in the Hadish Watercourse

Maryam Rahbani*

*Assistant Prof., Marine Science and Technology Department, University of Hormozgan, Bandar Abbas, Iran; maryamrahbani@yahoo.com

ARTICLE INFO

Article History:
Received: 18 Nov. 2017
Accepted: 14 Mar. 2018

Keywords:
Hadish watercourse
pollution
Delft3D
tide
Persian Gulf

ABSTRACT

Hadish watercourse located in the in south of Iran, is a seasonal channel of water which crosses through Bandar Abbas to reach to the Persian Gulf. This watercourse is faced with numerous environmental problems in regard with the pollution entrance. Huge amount of the urban and industrial sewages of the city are discharged into this watercourse. In this investigation, considering the discharge of 1.36 m^3/s into this watercourse, according to the literatures, the procedure of emission of pollution in the area was modeled. For this purpose Delft3D software has been employed. The model has been calibrated and evaluated considering water level data from Rajaee Port. It was found that, the pollution mainly remains inside the watercourse which is due to the ebb dominance nature of the channel. The results of this research show that the discharging the sewage into this channel endangers not only the western coast of Bandar Abbas, but the health of the citizens.

1. Introduction

Studying the quality of surface waters, such as streams and watercourses is of particular importance. This is specifically more crucial when this waterway crosses through a city. It also requires further attention when sewage and industrial or urban wastewater are released to them. According to Montuelle and Graillot the urban, and industrial developments produce many pollutant emissions, in increasing quantities and of a highly variable nature [1]. The problem will be arise when these materials are discharged to a waterway or a stream inside a city [2].

Hadish watercourse is one such waterway, which crosses across Bandar Abbas city to reach to the Persian Gulf (PG). Bandar Abbas is a coastal city in the south of Iran, and is also the center of Province Hormozgan. Figure 1 shows the location of the city in the province Hormozgan (A), the area considered for the model establishment (B), and the position of Hadish watercourse inside the city (C). This watercourse is also a tidal stream which could be count as complex watercourse that represent a transitional zone between riverine and marine systems [3].

The length of this watercourse is about 3000m., and its width in its mouth is about 60m [4]. The depth of the channel reaches up to 2.5 during flood period, when the channel is filed with Persian Gulf's water [5].

According to literature "if the pollution transport and dissemination mechanism in estuaries or rivers is specified, planning may be made to reduce the effects of pollution on public health" [6]. Generally, when a sewage pollution is released into water, it quickly spreads and is transferred by water flow owing to molecular motions, turbulence, and non-uniformity of velocity in flow section [7].

The health of Hadish watercourse nowadays is at risk. Vast amount of urban and industrial sewages from the city itself and from the neighboring area are discharged to the channel. The aim of this study is to find out the destination of the release pollutant in this channel, and the role of this sever channel for polluting PG. The pattern of the pollution during the tidal cycle has been investigated using Delft3D software.

2. Materials and Methods

2.1. Model establishment

The two dimensional version of Delft3D software, developed by Delft Hydraulic in Netherland, has been used for this investigation. The Flow Module in combination with Water Quality module of the model were considered to use [8]. The area considered for the modeling has been chose far out of the watercourse into the PG, far enough from the mouth, to prevent flow disturbances inside the channel (Figure 2A). In accord with the availability of the field data, the model extended inside the PG from the channel mouth along the coast in each direction for 3.5 km, and along the watercourse toward the sea for 10 km.

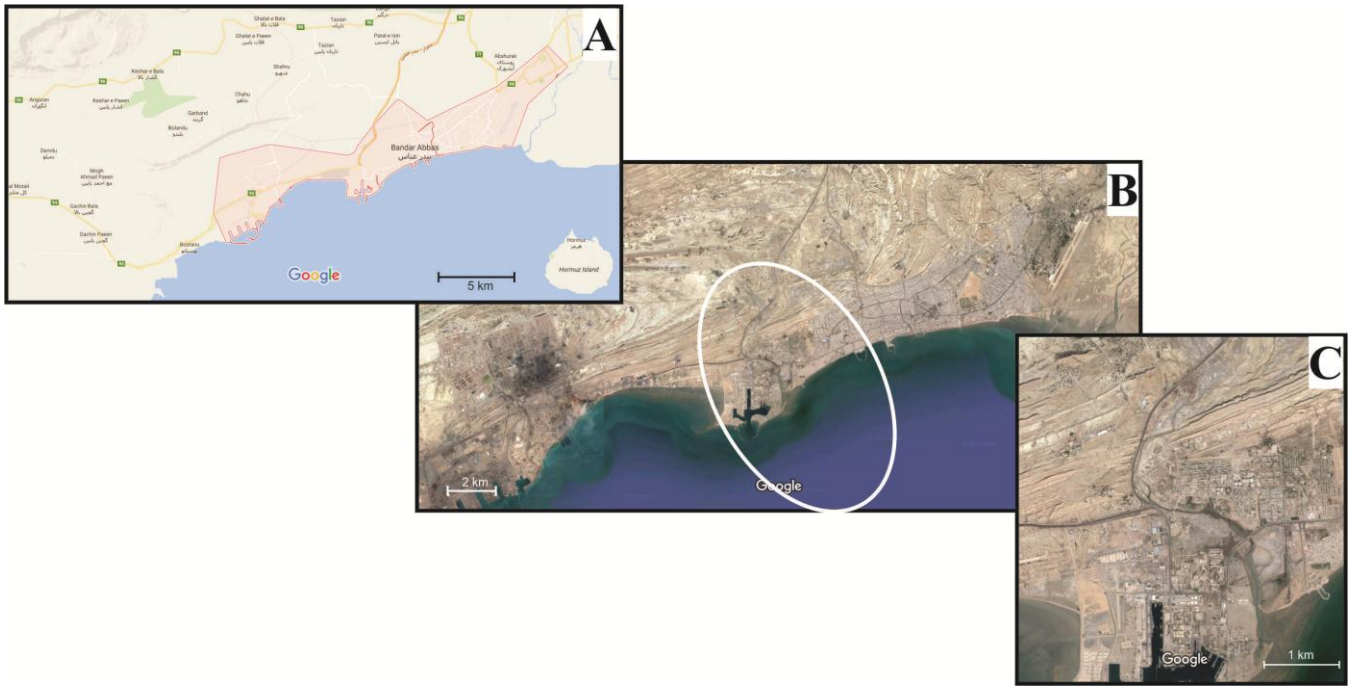

Figure 1: Area under investigation (Hadish watercourse) in Bandar Abbas

The bathymetry file for the area is received from National Cartographic Center of Iran (Figure 2B). As can be seen in Figure (2A) all boundaries along the watercourse were considered as dry boundary. Due to the seasonal nature of this channel, the upstream of the channel is almost always empty. Out inside the PG however three open boundaries were defined including western, eastern, and southern boundaries.

Since no measured data for water level was exist near the eastern and western boundaries, the water level data used for these two boundaries of the model where those derived out form the results reported by Ghasemizadeh [9]. In this investigation which has been carried out using MIKE21, the model results derived at Hormoz station were compared with those measured at Hormioz station.

Figure 3 shows the scatter diagram of water level derived from the model and those measured at field. The data presented in this figure are for the period of one month, from 18th of March 2011 till the 17th of April 2011, with the time step of 2 seconds. To show the good performance of the model, fitted trendline for the presented data in graph is provided. The equation represented the fitted trendline and its corresponded R-square are shown in the figure. Considering the fitted trendline equation, and the value of the R-square, it can be concluded that the water level data derived from this model can be used as boundary condition of the present model.

Since the area under investigation is located near the Rajaaee Port, those water level time series measured at this station has been applied, for the western boundary condition.

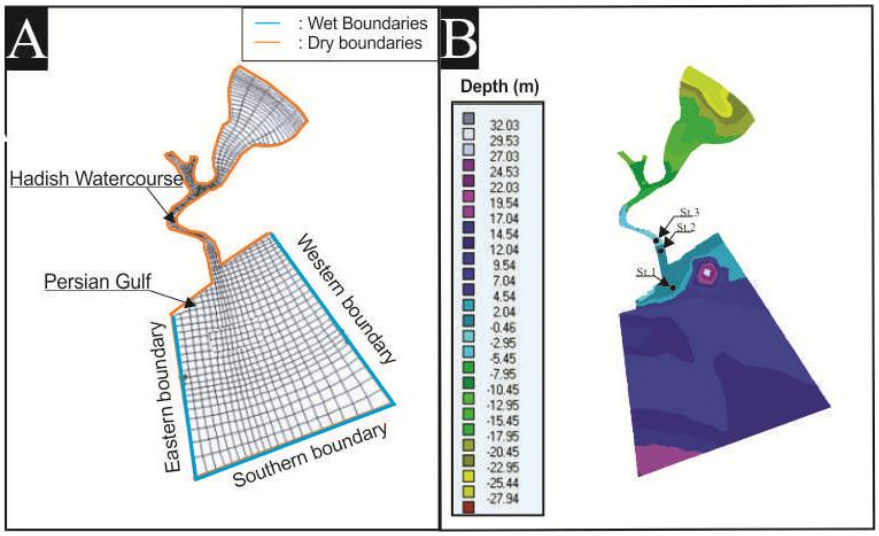

Figure 2: (A) Grid cells, the boundaries, and (B) the Bathymetry of the area

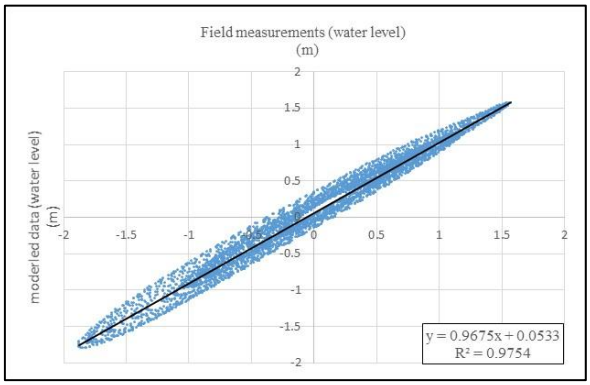

Figure 3: calibrated and validated water level data at Hormoz station

The time step of the model was considered 6 seconds on the basis of the Courant number stability. This number can be calculated using eq. (1).

$$C_r = 2\Delta t \sqrt{gH\left(\frac{1}{\Delta x^2}+\frac{1}{\Delta y^2}\right)} < 4\sqrt{2} \qquad (1)$$

in which g is gravity in m/s^2, Δt is time step in second, H is water depth in m., and Δx, Δy are the size of grids in x and y direction respectively in m. [10].

The threshold depth for the area, indicating the border between the wet and dryness cell, has been taken to be 0.01 meter. The vertical eddy viscosity parameter adopted for the modeling is 5 m^2/s through calibration. Since this study does not involve salinity and/or temperature transfer, the horizontal eddy diffusivity parameter doesn't take into account.

The bed roughness, in which its value can be expressed by Manning's number, should be adjusted as calibration parameter. The value between 0.016 and 0.04 is recommended by the Delft3D manual [11] for this parameter. Since the bottom of the watercourse is mainly covered by cement and stone the Manning's coefficient of friction is suggested to be relatively high. To achieve proper value for bed roughness, several simulations had been carried out with different Manning's number, and the water level data derived from the simulations were compared with the those water level time series, measured at Rajaaee Port station.

Figure 4 shows the water level results derived from three different simulations using the coefficient values of 0.02, 0.03, and 0.04 for Manning's number. Measured water level data is presented as dotted line in the figure. As it can be seen in the figure, employing value of 0.02 for the simulation, the model can reproduce the best fitted water level data with those of the field data.

2.2. Statistical methods to evaluate model results

There are different statistical methods to evaluate model results. Every single method could provide distinct information in which could be suitable to describe the model results.

Bias, RMSE, correlation coefficient (CC), and Nash-Sutcliffe Efficiency (NSE) are four methods has been used in this study to evaluate model results. These statistical values can be calculated using equations (2) to (5) respectively.

$$Bias = \bar{y} - \bar{x} \qquad (2)$$

$$RMSE = \sqrt{\frac{1}{N}\sum_{i=1}^{n}(x_i - y_i)^2} \qquad (3)$$

$$CC = \frac{\sum_{i=1}^{n}(x_i-\bar{x})(y_i-\bar{y})}{\sqrt{\sum_{i=1}^{n}(x_i-\bar{x})^2 \sum_{i=1}^{n}(y_i-\bar{y})^2}} \qquad (4)$$

$$NSE = 1 - \frac{\sum_{i=1}^{n}(x_i - y_i)^2}{\sum_{i=1}^{n}(x_i - \bar{x})^2} \qquad (5)$$

x_i and y_i in the above equations represents the measured and modeled results respectively. $\bar{x}$ and $\bar{y}$ are the averaged values for x and y.

Values near zero for Bias and RMSE means the goodness of estimated values. Correlation coefficient varies between -1 and 1, and shows the positive or negative correlation between the estimated and real values. NSE values varies between -∞ and 1. Minus values declare the poor estimation of the model [12].

2.3. Introducing pollution to the model

To investigate the emission of pollution in the area, the discharge of pollution should be introduced to the model [13]. Since no confirmed data was found in regard with the discharge of pollution into the watercourse, the average value of 1.36 m^3/s, reported by Ideh-Pardazan No Consulting Engineers [3], was considered as pollution discharge. To identify the behavior of the pollutant particle, its concentration was considered to be constant in this research.

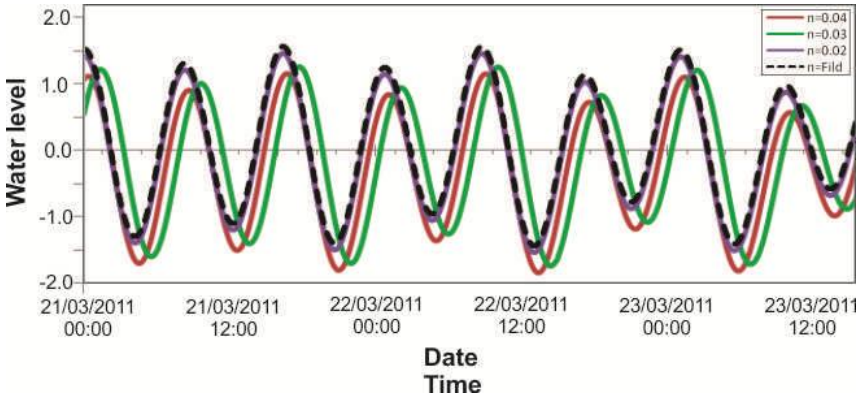

Figure 4: Model calibration with different Manning number

For pollution and particle tracking, Delft3d software is provided with a module called "D-WATER QUALITY". Trackers in this module are considered to be special types of materials, which are not affected by chemical and biological changes and are merely displaced under hydrodynamic and physical conditions [14]. Using this module, it is possible to track a specific particles pathway, and/or the pattern of pollution in a field of study.

In order to estimate the approximate time in which pollutant needs to reach to the mouth of the channel by the PG, a pollution dissemination modeling was executed. This is to comprise a proper time interval for a released pollution to reach to the mouth of the channel. A tracker particle was released at the middle of the watercourse (ST. 3 in Figure 5).

After executing several models for different periods, it was found that a one-month time period is sufficient for the aim of this research.

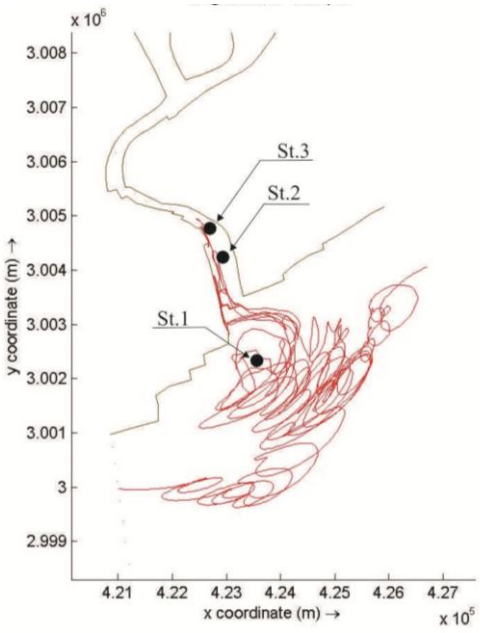

Figure 5: particle tracker simulating for a period of one month

3. Results and Discussion

Scattered diagram of water level data is provided to present the goodness of the model results. Figure 6 shows that modeled water level are in good agreement with the measured water level at Rajaee Port station. As it can be seen in the figure the data are scattered perfectly along the trend line of X=Y.

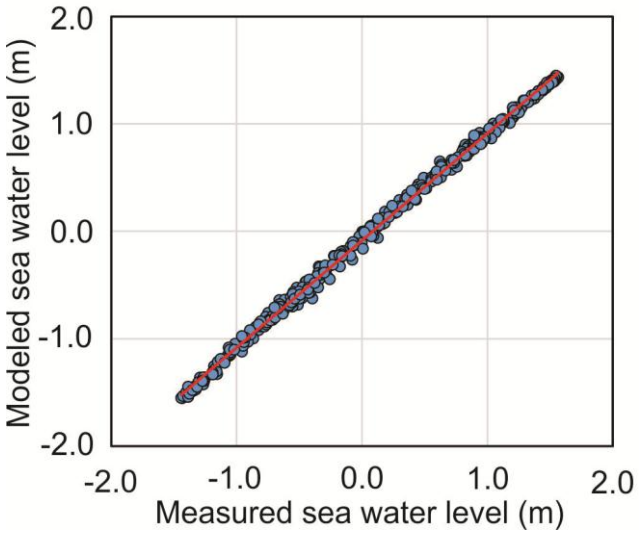

Figure 6: Scattered diagram of water level data

In order to represent the statistical values for the model results Bias, RMSE, correlation coefficient and NSE were calculated for the modeled water level results. Table 1 shows this values.

Table 1: statistical values for the modeled results

Bias	RMSE	CC	NSE
-0.74	0.83	0.001	0.98

All the statistical values confirm that the developed model could provide water level results comparable with those measured in the field.

Figure 7 shows the field water level data at Rajaaee Port (A), water level at three stations 1, 2, and 3 at mouth and along the watercourse (B) (see Figure 2B), and current velocity time series at the same stations(C). This figure shows that the water level along the channel is in phase with the water level at Rajaaee Port. The

high water is about 2 m in Rajaaee Port and inside the channel. During the ebb phase however, the whole water of the channel empties into PG. The current velocity (Figure 7(C)) at the mouth of the channel is not with the same phase as that of stations 2 and 3. It could be seen that at the beginning of the flood phase, the strong current at the channel mouth speeds out of the channel toward the PG. The speed reaches up to 30 cm/s. At the end of the ebb phase however, the station at the mouth experiences quit contrariwise experience; for the last 2 hours of this phase a relative strong current of about 20 cm/s follows toward the channel. This suggests the longer period for ebb phase, which is also represented in Figure 7(B). Besides, according to the Figure 7(C) the seaward current velocity at the mouth of the channel (station A) is weaker than the flow toward the channel (about 10 cm/s). All of these results emphasize that the channel is ebb dominant, which is in agreement with the local observations.

Figure 8 show the pattern of current velocity distribution for the two instant time of the low water (A), and high water (B) in the 21st of March 2011. The low tide of 01:40 and the high tide of 23:00 are shown in Figure 7 with dotted lines in order to be recognizable easily. This figure shows that the inflow current velocity at high water is weaker than outflow current velocity at low water. This is also confirmed the ebb dominance of the watercourse.

In order to trace the behavior of the released sewages in the channel the amount of 1.36 m^3/s as a pollutant substance was introduced to the model at all stations. The model was executed for one month. Figure 9 (A to D) show the results for the first, forth, seventh, and tenth day of this execution. All the presented pictures are derived out during the flood phase. It can be seen that in the first day of the pollution release, its affect has been felt inside the PG (Figure 9A). In the fourth day of the simulation this amount inside the PG was decrease significantly (Figure 9B). This rule is followed in the seventh day as shown in Figure 9(C). In the tenth day of the simulation (Figure 9D) no trace of pollution can be seen in the PG. and this trend continues for the whole month. Inside the channel however during all these days the maximum pollution is evident.

The entrance of the pollution inside the PG at the beginning of the simulation can be due to the model warm up. This means the model needs at least ten days of simulation for stabilization in regard with pollution.

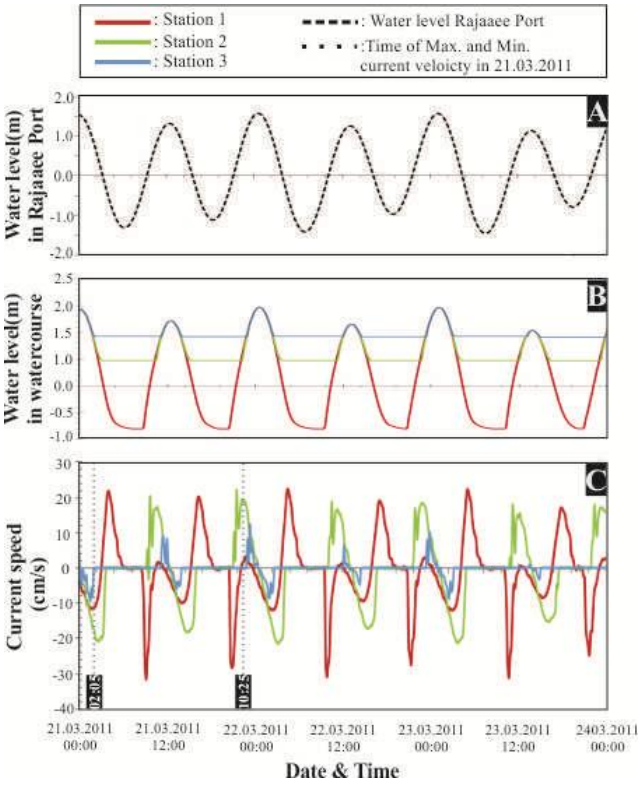

Figure 7: (A) Water level at Rajaaee Port, (B) water level at stations 1, 2, and 3 along the watercourse, (C) current velocity time series in the stations 1, 2, and 3

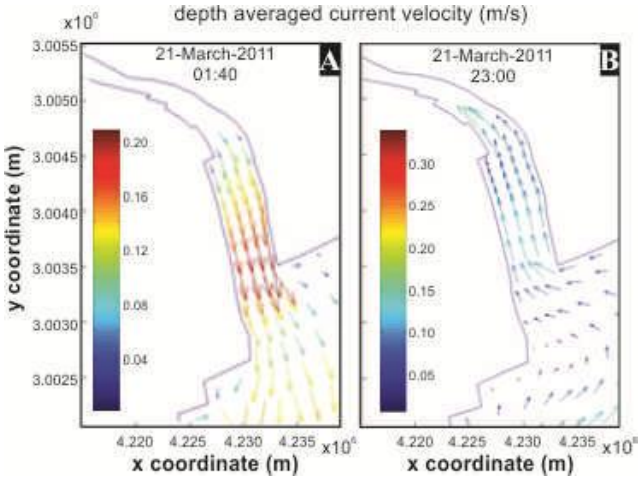

Figure 8: Current velocity pattern inside the watercourse at (A) low tide (01:40 21/03/2011) and (B) high tide (23:00 21/03/2011)

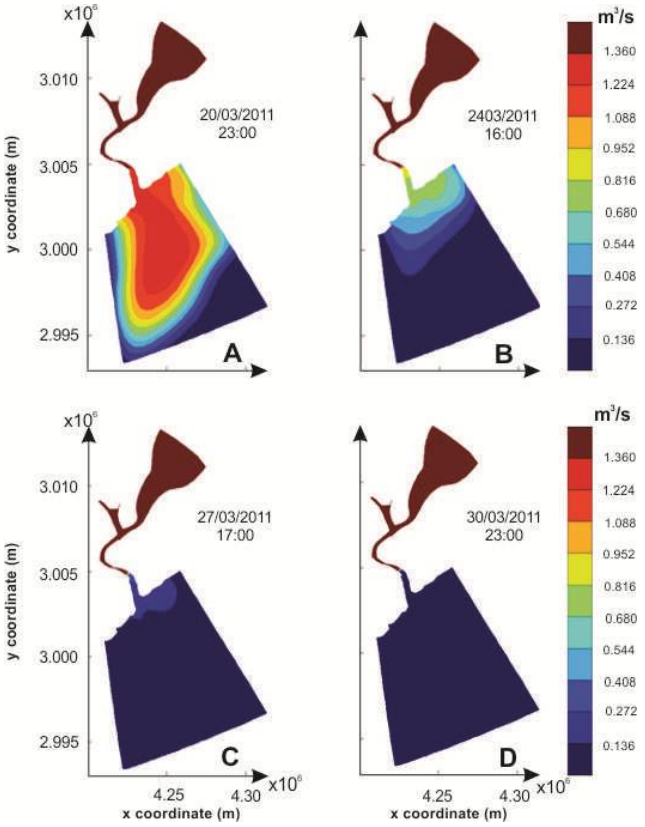

Figure 9: The pattern of pollution in the area under investigation for the first, fourth, seventh, and tenth day of model simulation

4. Conclusion

The watercourse of Hadish in Bandar Abbas was modelled in this investigation, to represent the side effect of release of urban sewage in it. The results show that the channel is merely under the effect of tide, and the upstream of the channel is mostly dry. It was found that the channel is ebb dominant.

Introducing the pollution discharge of 1.36 m^3/s to the model along the channel, the model was executed, and the results show that the pollutant mainly remains to the channel and rarely enter to the PG. This finding even if is not evaluated using the actual data, due to the unavailability of the field data, is an alarm for the city of Bandar Abbas and its citizens to think carefully about the release of sewage in this watercourse and find a solution to restore this watercourse.

8. References

1- Montuelle, B. and D. Graillot, (2017*), Fate and effect of pollutants in rivers: from analysis to modeling*, Environ Sci Pollut Res., 24 (3): 3211-3213.

2- Farnham, D.J., R.A. Gibson, D.Y. Hsueh, W.R. McGillis, P.J. Culligan, N. Zain, and R. Buchanan, (2017), *Citizen science-based water quality monitoring: Constructing a large database to characterize the impacts of combined sewer overflow in New York City*. Science of the Total Environment, 580, 168-177.

3- Cheng, X.J., W. Zhan, Z.R. Guo, and L.R. Yuan, (2012), *A modeling study on saltwater intrusion to western four watercourses in the Pearl River estuary*. China Ocean Engineering, 26(4), pp.575-590.

4- Ideh-Pardazan No Consulting Engineers, (2011), *Reports of studies conducted on river bed limit determination and organization, surveying and creating GIS system for the seasonal rivers around Bandar Abbas*. Regional Water Company of Hormozgan Province. [in Farsi]

5- Hamzeh, M., (2007), *Further Necessities for Estuary Protection*. Bandar va Darya Journal, Vol. 12, p. 117-119. [in Farsi]

6- Qiany, Z. and H. June, (2009), *Scalindispersion mode for pollutant transport in river*. Journal of environmental modeling software, Vol. 24, 627-631.

7- Ward, E.W., and K. Winter, (2016), *Missing the link: urban stormwater quality and resident behaviour*. Water SA, 42(4), 571-576.

8- Deltares, (2010), Delft3D-FLOW, Simulation of multidimensional hydrodynamic flows and transport phenomena, including sediments, user manual.

9- Ghasemizadeh, N., (2012), *Examining the Effect of Constructing Long Wharfs on Coastline Variations (Case Study: Persian Gulf Eastern Coast)*. M.Sc. thesis, International Campus of Hormozgan University, Qeshm, 124 pages. [in Farsi]

10- Luijendijk, A. P., (2001), *Validation, Calibration and Evaluation of Delft3D-Flow Model with Ferry Measurements*. M.Sc, Thesis, TUDelft, C9535180.

11- WL|DelftHydraulics, (2006), *Delf3D User Manual*, Delft Hydraulics 3.27 v.

12- Moriasi, DN., JG. Arnold, MW. Van Liew, RL. Bingner, RD. Harmel, and TL. Veith, (2007), Model evaluation guidelines for systematic quantification of accuracy in watershed simulations. *Trans. Asabe, 50*(3), pp.885-900.

13- Bliss-Guest, and A. Patricia, (1981), *The Protocol against Pollution from Land-Based Sources: A Turning Point in the Rising Tide of Pollution*. Stan. J. int'l L. 17: 261.

14- Baghernejad, A., (2011), *Examining Pollution Dissemination in Qeshm Waterway*. M.Sc. thesis, Hormozgan University. [in Farsi]

INTERNATIONAL JOURNAL OF
COASTAL & OFFSHORE ENGINEERING IJCOE Vol.3 /No. 4/Winter 2018 (27-35)

Available online at: http://ijcoe.org/browse.php?a_code=A-10-52-1&sid=1&slc_lang=en

Numerical Modeling of Heat and Brine Discharge near Qeshm Desalination Plant

Saeed Memari[1], Seyed Mostafa Siadatmousavi[2*]

[1] M.Sc. Student, School of Civil and Environmental Engineering, Iran University of Science and Technology; s_memari@civileng.iust.ac.ir
[2] Assistant Professor, School of Civil and Environmental Engineering, Iran University of Science and Technology; siadatmousavi@iust.ac.ir*

ARTICLE INFO

Article History:
Received: 26 Dec. 2017
Accepted: 17 Mar. 2018

Keywords:
Numerical Modeling
Desalination Plant
FVCOM
Finite Volume
3D Circulation model

ABSTRACT

Desalination plants have become invaluable solutions especially where freshwater resources are scarce. However, the byproduct of their operation is an outflow which is more saline and heated than the ambient water body. This heated plume adversely affects the ecosystem if it is not treated properly. In this study, 3D finite volume coastal and ocean model is employed to address this issue close to Qeshm Island. In addition to calibrating the model, two alternatives are simulated and discussed to mitigate the adverse effects of the heated plume. It is shown that the plume tends to move in the upper layer of the water column due to its lower density than the ambient water. By moving the outfall to deeper parts of the sea—10-meter-deep—the negative effects of the plume significantly decrease, and as a result, it fulfills the Iran national guidelines. Moreover, due to the mechanism of the Qeshm desalination plant, the spread of salinity is of the least importance compared to the increase in temperature.

1. Introduction

Today, with the galloping rate of water use in both industrial and municipals sectors, the need for a reliable source to this end is crucial. Meanwhile, desalination plants have become invaluable tools to supply freshwater; however, their byproduct – brine – should be accurately dealt with, since the brine can adversely affect the environment if it is not discharged appropriately and according to guidelines [1]. The Qeshm desalination plant is located at the northern part of the Qeshm Island. It uses distillation process to extract freshwater from oceanic saline water. However, by using this process, the outflow is not only more saline than the ambient water—sea water—but also warmer due to the process it went through. Warm and saline water discharged into the sea adversely affects fauna and flora close to the outfall location [2]. Accordingly, especial discharge plan should be considered to deal with this kind of byproduct.

Two types of approaches are employed when discharging into the sea is concerned [3], first of which is near-field approach which deals with the area where the plume is greatly dominated by the momentum force. This momentum is generated when the brine leaves the outfalls, and its effect is much greater than the turbulence existing in the sea. The parameter which is most important in this region is dilution. Physical condition, namely shape, diameter, and the number of outfalls as well as well as ambient conditions, namely depth and currents are of great importance when the plume behavior in the near-field is concerned. The second approach is called far-field, and the far-field area begins where the plume is no longer bounded to the initial momentum of the outfall. In fact, sea currents and sea turbulence are the most important factors in dispersion of the plume in far-field area [4-6].

Among methods to determine the plume behavior, mathematical models are used by solving the advection-diffusion equation under certain conditions to simplify the equation [7]. To solve the equation, its parameters for describing the ambient currents and conditions should be simplified in a way that the equation can be solved analytically [8, 9]. Accordingly, this method is unable to consider all parameters playing roles in dispersion of the plume at the same time. On the other hand, hydrodynamic models have become invaluable tools in simulating the currents and plume behavior using all parameters having impact on currents and plume behavior.

Purnama et al. studied the optimum location of the outfall by solving advection-diffusion equation so that the brine effects at the beach are minimized [7, 10, 11].

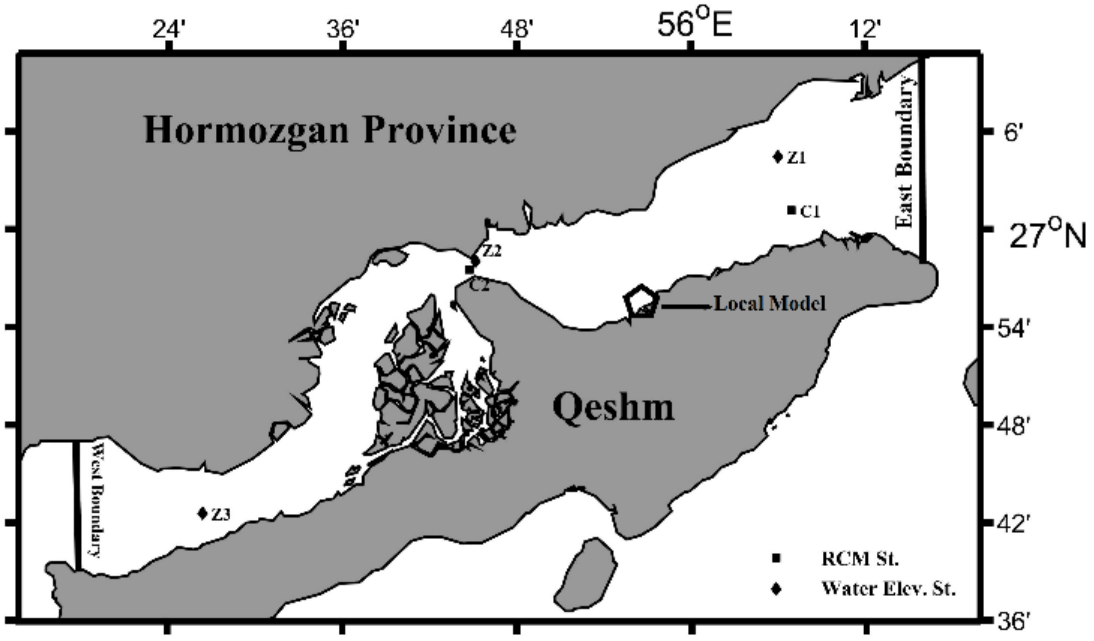

Figure 1: The regional model domain, open boundaries, location of the local model, and the stations used for calibration. The domain of the local model is shown by pentagon.

They solved this equation under simplified condition to determine the horizontal distribution of the brine plume. Similarly, Mohamed used a 2D numerical model to assess the effects of land reclamation on the circulation on the behavior of the heated plume [12]. Likewise, Sun et al. used a 3D numerical model (FVCOM) to determine the plume behavior for a reverse osmosis desalination plant and to locate the outfall where it has minimum effect on the sea grass [13].

2. Materials and Methods

2.1. Case Study

Khuran Channel—also known as Strait of Khuran—is located at the north part of the Persian Gulf (Fig. 1), between Qeshm island and southern mainland of Iran (55.24-56.25 E, 26.60-27.15 N). The maximum depth of the channel is ~34 meters (Fig. 2), and it is considered as a shallow channel [14]. Length of the Khuran Channel between its west and east borders is 110 km, and its maximum width is ~25 km at its east border and its minimum width is ~3.5 km at the middle of the channel. Meteorological data acquired from Iran Meteorological Organization assert that the variation in temperature between day and night are not significant and the weather is considered warm and humid in summers with mild temperature in winters.

Furthermore, current directions are mainly along the channel, and currents are mainly generated by tides. Likewise, main tide constitutes are M2, S2, N2, K1, and O1 [15, 16]. Wind, on the other hand, poorly contributes on the generation of currents, since wind direction is generally perpendicular to dominant alongshore currents induced mainly by tide; therefore, wind effects are negligible [14].

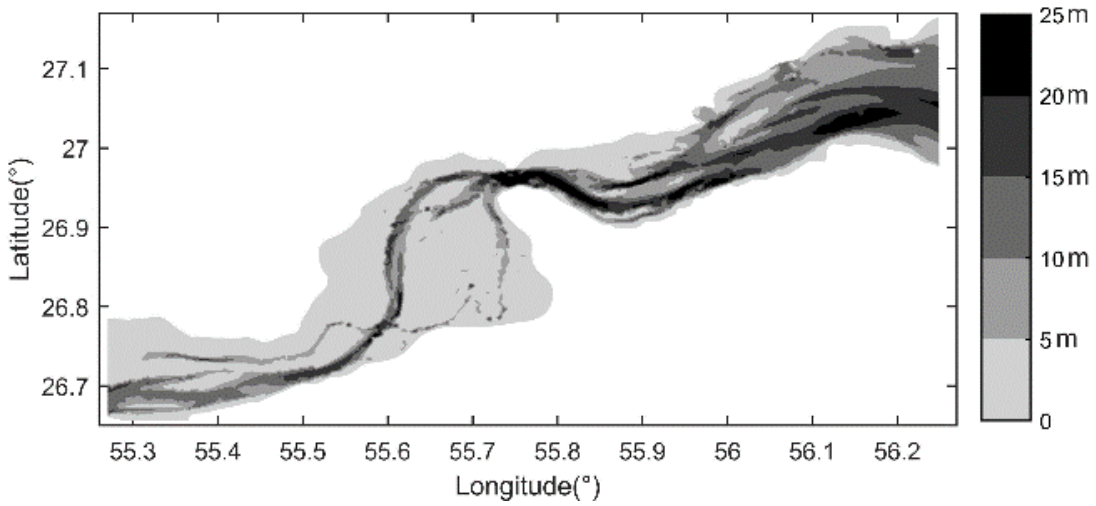

Figure 2: Bathymetry of the Khuran Channel in the northern part of the Qeshm Island

Khuran Channel is the habitat of many marine animals and plants. Moreover, mangrove forests are present in the middle of the channel, and they are preserved as protected areas. There are also a number of industrial facilities along the coast of Khuran Channel, namely ship building companies, power plants, desalination plants, ports, to name but a few. Most of these facilities discharge their waste into the channel. Meanwhile, heated outflows are of great importance, since not only they adversely affect the marine ecosystem, but they might cause stratification as well, taking a great deal of time to dilute with ambient water.

Qeshm desalination plant had experienced some problems in its discharge pipelines and decided to discharge its heated and saline waste through a channel at the beach and on the surface near the plant. By applying this old-fashioned method of discharging, it took a long time for the outflow to dilute because currents near the shore were generally weak. Moreover, the absence of initial momentum existed for a submerged outfall also increased the dilution time.

2.2. Governing Equations and the Numerical Model

Finite Volume Coastal and Ocean Model—FVCOM—with an unstructured grid was applied for this study [17]. FVCOM numerically solves the equations of conservation of momentum, continuity, temperature, salinity, and equation of state for density, analogous to the equations used in other ocean models, which are presented hereunder.

$$\frac{\partial u}{\partial t}+u\frac{\partial u}{\partial x}+v\frac{\partial u}{\partial y}+w\frac{\partial u}{\partial z}-fv=-\frac{1}{\rho_0}\frac{\partial P}{\partial x}\frac{\partial}{\partial z}\left(K_m\frac{\partial u}{\partial z}\right)+F_u \quad (1)$$

$$\frac{\partial v}{\partial t}+u\frac{\partial v}{\partial x}+v\frac{\partial v}{\partial y}+w\frac{\partial v}{\partial z}-fu=-\frac{1}{\rho_0}\frac{\partial P}{\partial y}+\frac{\partial}{\partial z}\left(K_m\frac{\partial v}{\partial z}\right)+F_v \quad (2)$$

$$\frac{\partial P}{\partial z}=-\rho g \quad (3)$$

$$\frac{\partial u}{\partial x}+\frac{\partial v}{\partial y}+\frac{\partial w}{\partial z}=0 \quad (4)$$

$$\frac{\partial T}{\partial t}+u\frac{\partial T}{\partial x}+v\frac{\partial T}{\partial y}+w\frac{\partial T}{\partial z}=\frac{\partial}{\partial z}\left(K_h\frac{\partial T}{\partial z}\right)+F_T \quad (5)$$

$$\frac{\partial S}{\partial t}+u\frac{\partial S}{\partial x}+v\frac{\partial S}{\partial y}+w\frac{\partial S}{\partial z}=\frac{\partial}{\partial z}\left(K_h\frac{\partial S}{\partial z}\right)+F_S \quad (6)$$

$$\rho=\rho(T,S) \quad (7)$$

where x, y, and z are east-west, north-south, and up-down directions at Cartesian coordinate, respectively; similarly, u, v, and w are the velocity components at x, y, and z directions. T, S, ρ, P, f, and g are water temperature, salinity, density, pressure, Coriolis coefficient, and gravity acceleration coefficient. K_m, K_h, F_u, F_v, F_T, and F_s denote the vertical eddy viscosity coefficient, thermal vertical eddy diffusion coefficient, horizontal momentums, thermal diffusion terms, and salt diffusion terms, respectively.

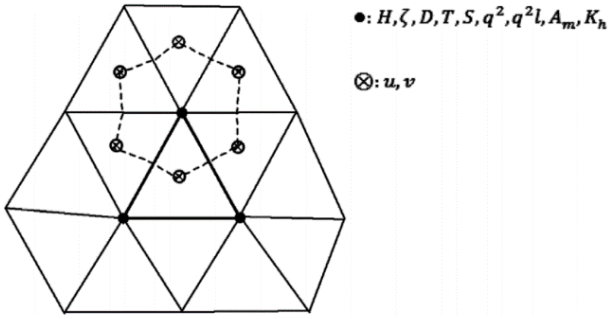

Figure 3: Illustration of triangular unstructured grid. Scalar quantities are defined on the nodes and vectors are defined on the center of elements.

As shown in Fig. 3, the scaler parameters are located on the nodes and the velocity components are located in the center of mesh elements.

Furthermore, the Smagorinsky formula [18] and Mellor and Yamada level 2.5 turbulence closure schemes [19] are used for horizontal viscosity and diffusivity, and vertical mixing.

Using an unstructured triangular grid, FVCOM is capable of modeling complex coastlines and sharp topographies. For vertical layer, σ-coordinate system is used, and at the same time unstructured triangular grid is used for horizontal grid. A finite volume method makes benefit from finite element advantages such as geometric flexibility, and from finite difference advantages namely simple discrete system and effective computation. Thus, the model perfectly functions in describing mass, momentum, and conservation of heat and salt for a complex coastline area.

Furthermore, FVCOM is very capable at calculating wet and dry conditions which makes it an invaluable tool where wet and dry condition is concerned, especially in mangrove forests (Hara Jungle) where it submerged under the water during tidal floods, and it rises above the water during ebb period, making it a dry region. Memari and Siadatmousavi showed that by assuming the Hara Jungles as a wet region at all time or a dry region at all time, currents change dramatically before, after, and at the Jungle regions [20]. Therefore, application of FVCOM nicely suites for this region.

3. Models

3.1. Model Inputs and Description

In the first place, due to the spatially extensive domain, two models with different inputs and mesh sizes are employed: the regional and the local model. The regional model which is the bigger one with courser mesh size is employed to calculate the tide, salinity, and temperature in the Khuran channel, and then provides the boundary conditions for the local model nested inside the regional model.

3.2 Regional Model

The regional model consisted of 10233 elements and 5396 nodes. Moreover, their size near the local model is ~35 meters and grows to ~700 meters at the open

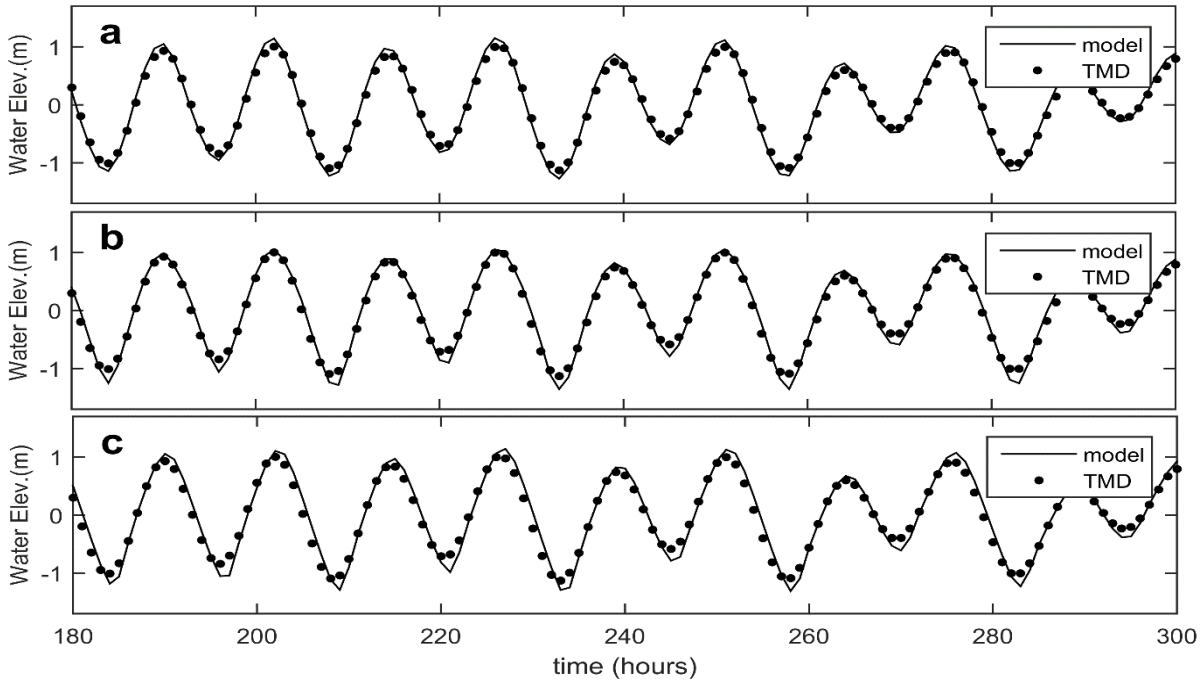

Figure 4: Comparison of tidal elevation and model results at St. Z1 (a), Z2 (b), and Z3 (c).

boundaries, and therefore the elements near the local model boundaries are smaller. The duration of the model run starts from 2005/08/30 to 2005/09/14 for the total of 15 days which includes a full neap and spring tidal cycle. Also, the model startup is set as cold start, and the initial salinity and temperature are set as 32 psu and 32.5°C, respectively. The external time step of the model is set as 0.09 seconds.

The forcing imposed to the model is wind, tide, salinity, and temperature. Wind data are attained from ECMWF Era-Interim database [21] and imposed throughout the domain for the period of the model run. At the same time, although CTD field data showed that the temperature and salinity are vertically homogenous [14], the salinity and temperature data acquired from HYCOM database center [22] are imposed at both east and west open boundaries for the duration of the model run. Furthermore, tide data are attained from TMD model [23] for the duration of the model run at both east and west open boundaries. The harmonic constitutes of tide imposed to the model are $M2, S2, N2, K2, K1, O1$, and $P1$.

Furthermore, bathymetry data used for both regional and local model are acquired from Iran National Cartographic Center [24] with some modification using both GEBCO and local data [25].

3.3. Regional Model Calibration

Bottom roughness coefficient is used to calibrate the model with respect to the five stations assigned along the channel, three of which are used to compare TMD results with model predictions of the water elevation. The other two are RCM9 devices, recording the velocity components of u and v, the locations of which are shown in Fig.1. The data used for stations C1 and C2 were measured by Iranian National Institute for Oceanography and Atmospheric Science in 2005.

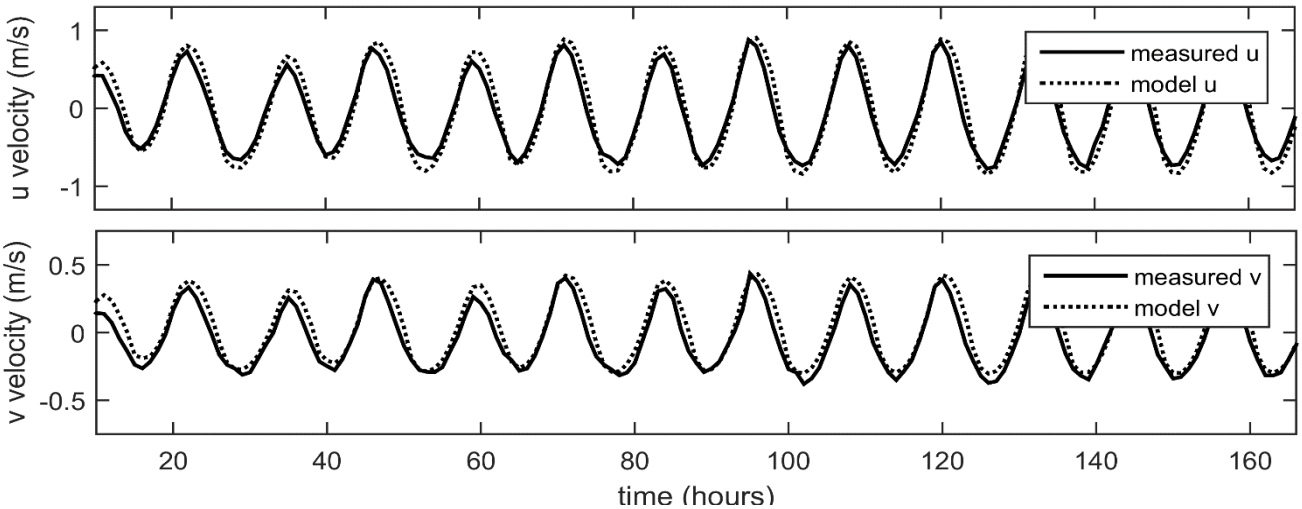

Figure 5: Comparison of velocity between measured data and model results at St. C1

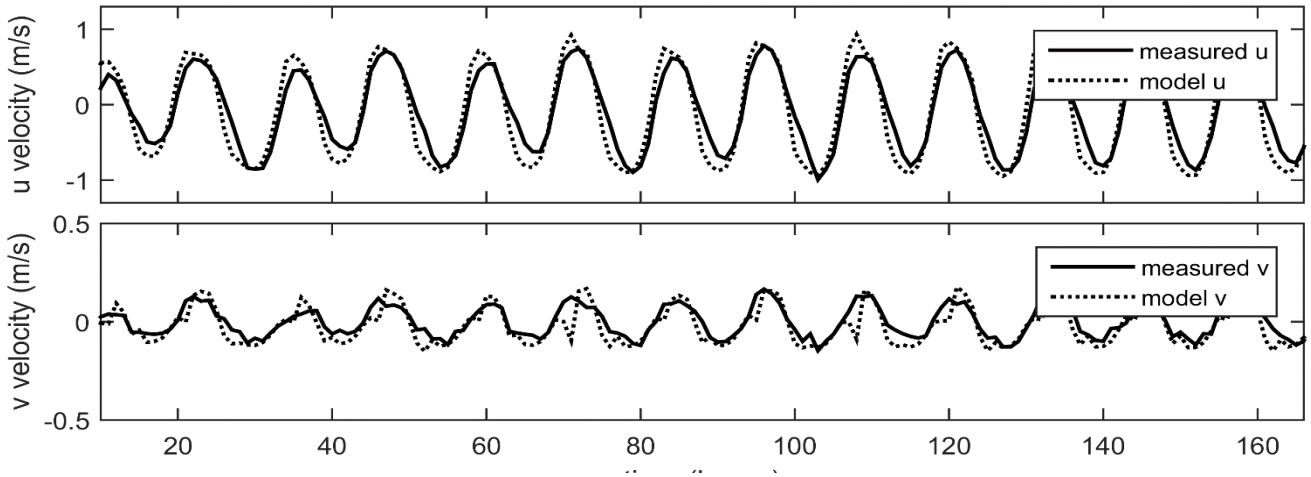

Figure 6: Comparison of velocity between measured data and model results at St. C2

As it can be seen in Fig. 4, the water elevation for all three stations (Z1 to Z3), are in a very good agreement with the TMD results. In similar fashion, in Fig. 5 and 6 the velocity calculated by the regional model and the in situ velocity data are compared, and it can be seen that the two are in a very good accord. Furthermore, the RMSE criterion and the correlation coefficient for all five stations are presented in Table 1, showing that the regional model is well calibrated.

Table 1: RMSE and Correlation Coefficient for all five St.

Station	RMSE	Correlation coef.	Depth (m)
Z1	0.096	0.993	16.65
Z2	0.114	0.990	31.87
Z3	0.130	0.987	16.75
C1	0.150	0.979	21.52
C2	0.218	0.948	28.56
Perfect Match	0	1	---

3.4 Local Model

Since the spread of heat and brine happens in a relatively short distance from the outfall, employing a local model with smaller mesh size is vital. To this end, a local model with a higher resolution consisted of 8848 elements and 4552 nodes is constructed in a way that the minimum mesh size at the outfall locations is 10 meters and increases to 200 meters at the open boundary (Fig. 7). Similarly, the external time step for the local model is set to 0.03 seconds.

Since the dispersion of heat and saline water is greatly affected by horizontal and vertical dispersion coefficient, the local model then should be calibrated with respect to the heat and saline outflow. To this end, four CTD stations at the distance of 150 and 200 meters from the coastal discharge point—present situation—

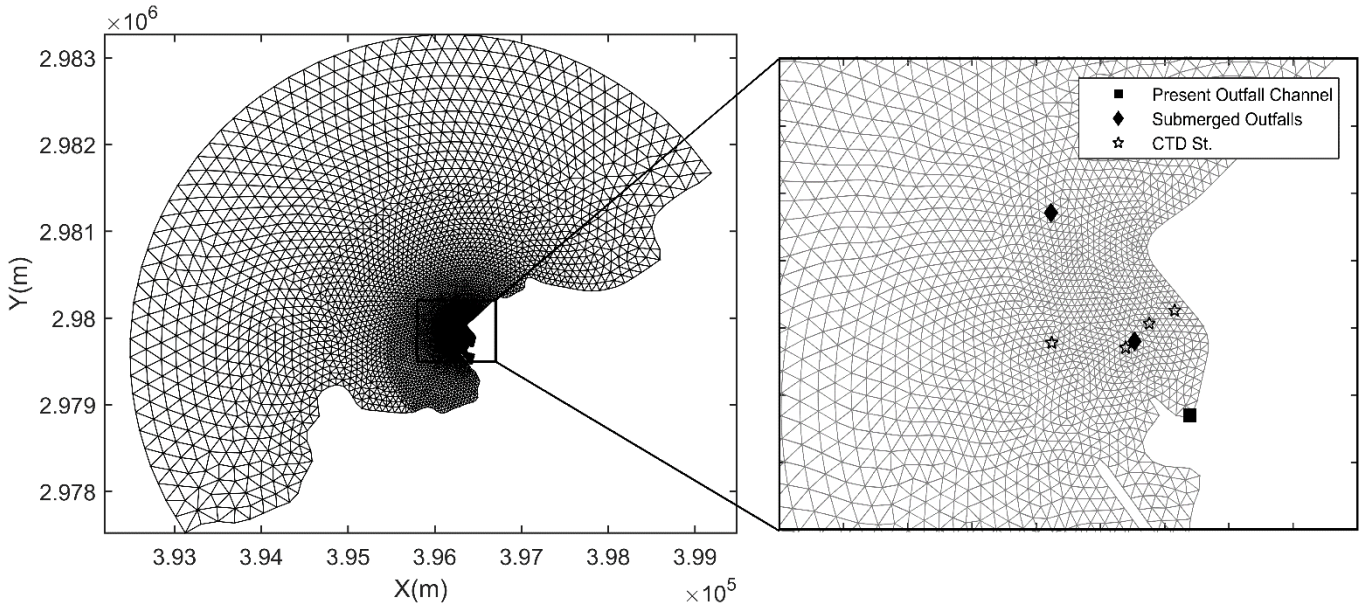

Figure 7: Local model mesh as well as present coastal discharge and submerged scenarios

were used to calibrate the local model with respect to the heat and salinity dispersion.

However, unlike field measurements used for calibrating the hydrodynamics of the regional model, the CTD field measurements were conducted at year 2016. Therefore, the calibrated regional model was run again for that period and the boundary conditions namely salinity, temperature, and tide for the local model was transferred from the regional model to the nested local model. Similarly, the ECMWF wind data were used in the local model as well. The local model was calibrated in a way that the maximum difference of the salinity or heat between the model results and measured results would be less than 4 percent (see Table 2).

Table 2: Maximum error of calibration as well as distance of the CTD Stations from the present discharge channel

Station	t82	t32	t92	t4
Maximum Abs. Error (℃)	0.432	0.796	0.449	0.837
Maximum Percent Error (%)	1.90	3.50	2.03	3.90
Distance From Outfall (m)	150	150	150	200

An extra day is added to the simulation period to warm up the model for velocities, tides, salinity, and temperature. Moreover, the actual discharge point of the outflow, an open channel at the shoreline, is implemented with discharging rate of $2.5\ m^3/s$, and the temperature and salinity of 31℃ and $43\ psu$, respectively, according to the CTD field data at the mouth of the discharge channel. Similarly, the initial values of water salinity and temperature are set as $37.4\ psu$ and 21℃, respectively.

Furthermore, to assess the permissible amount of heat and salinity, different countries have distinct guidelines and regulation based on their native ecosystem. According to Iran national regulation, the maximum amount of temperature at the distance of 200 meters from the outfall must not exceed 3℃ from the ambient water temperature. Similarly, the maximum amount of salinity must not exceed 10% of the ambient water salinity.

4. Distribution of Heat and Saline Outflow

The outflow whose temperature is above the ambient water tends to float and move at the upper layer of water column, and at the same time, the outflow which is more saline than the ambient water tends to sink and move close to the bottom of sea. In this case which is a combination of saline and heated water, the outflow tends to move in upper layer due to the dominant effect of heat on the density of the plume compared to corresponding effect by salinity [26].

As it was mentioned before, three cases are discussed in this study, first of which is the actual method of discharging—surface discharge through a channel at the beach—and two other scenarios which are submerged outfalls, a 5.5-meter-depth and 10-meter-depth submerged outfalls.

4.1. Distribution of Heat

Fig. 8 shows the maximum amount of excess heat at the distance of 200 meters from the present outfall as well as other scenarios for all time steps during the local model run. In each time step during the local model run (one day), the greatest value of heat is depicted, and as it can be seen, for the present outfall—surface discharge—almost in all time steps, the value of heat outreached the guidelines—the horizontal line showing the value of 3 (in degrees Celsius). As the outfall moved to deep areas of the sea and also changed the mechanism of discharging from surface discharge to submerged discharge, the critical value of heat decreased dramatically. Moreover, having moved the outfall to 10-meter-depth, the results asserts that due to the high speed currents, depth, turbulence, and more dilution, the maximum amount of heat in each time step decreased dramatically, showing that it is the best place

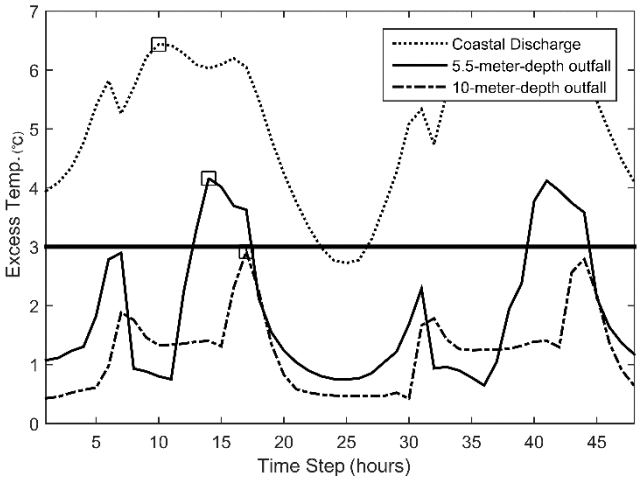

Figure 8: Maximum amount of increase in temperature at the distance of 200 meters from the outfall location for all scenarios and time steps

to discharge the outflow.

Fig. 9 shows the horizontal dispersion of heat at the upper layer of the water column in critical time steps marked on Fig. 8 by squares. As it can be seen, the coastal discharge is the worst method of discharge, causing the plume to slowly dilute, and therefore vast area of the sea is affected by excess heat. The 5.5-meter-deep outfall dilute the plume with much faster rate than the coastal discharge; However, it fails to satisfy guidelines, stating that the amount of excess heat at the 200-meter distance from the outfall must be less than 3℃. Finally, the 10-meter-deep submerged outfall is capable of generating enough dilution for the

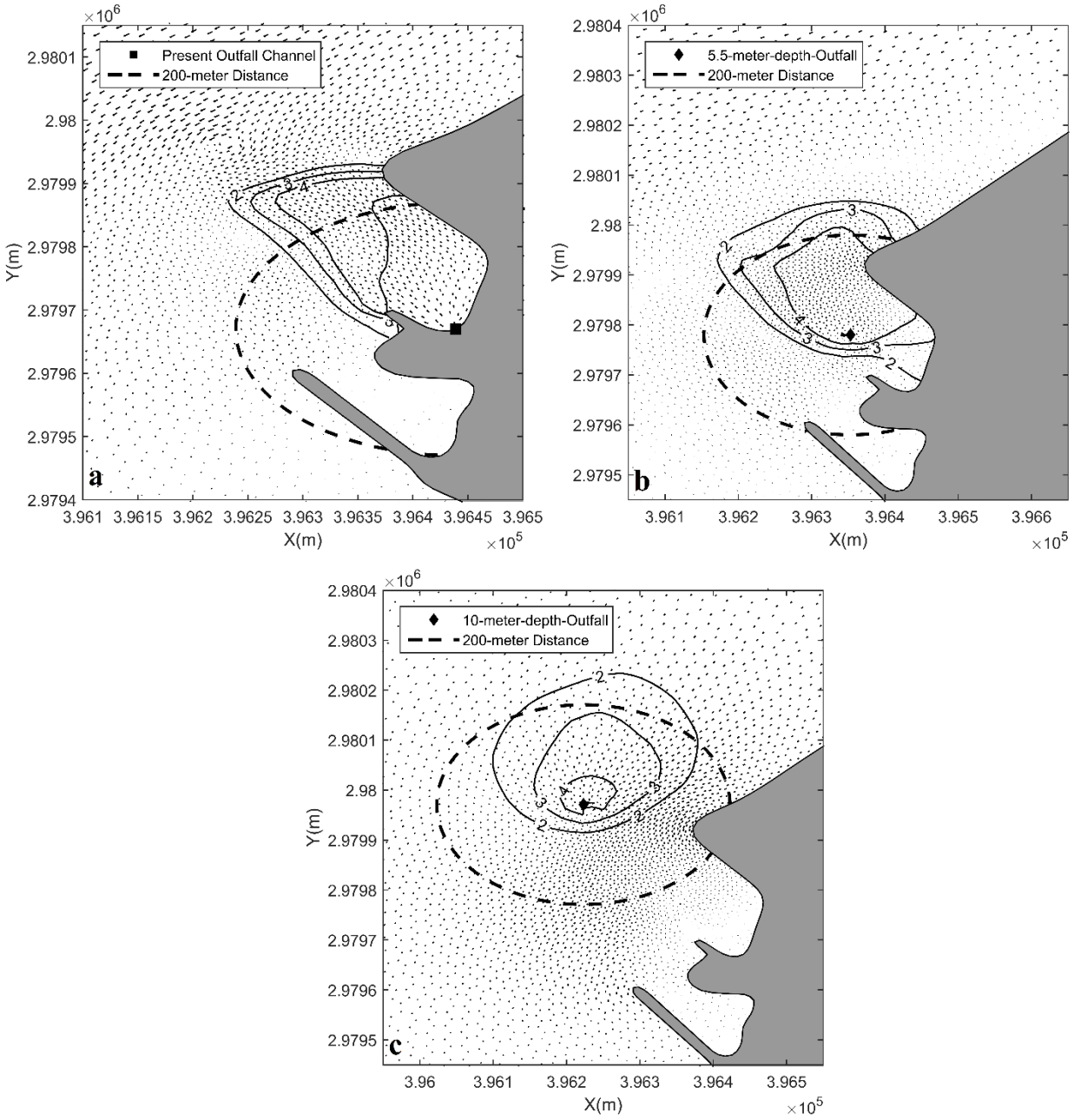

Figure 9: Surface dispersion of heat for (a) surface discharge, (b) 5.5-meter submerged outfall, and (c) 10-meter submerged outfall. The corresponding current vectors for the upper layer are also demonstrated

plume to leave the excess heat of less than 3℃ at 200-meter distance from the outfall location. Therefore, only 10-meter-deep outfall is capable of maintaining the guidelines in all time. Note that the rise and fall in the time series of temperature is in fact out of phase with tidal current; i.e. when current speed is low, the temperature rise is higher due to lack of advection which helps to dilute the plume with the ambient water. Fig. 10 shows the critical situation of heat dispersion when water elevation is at high value. In the absent of a strong current, more time is needed for the plume to dilute with ambient water. Therefore, the two high peaks for each line in Fig. 8 correspond to the high and the low water elevation, or in other words weak currents (slack water).

4.2. Distribution of Salinity

The regulations assert that the amount of salinity at the distance of 200 meters from the outfall should be less than 10% of the background salinity—in this case it equals to 3.75 psu. Since the mechanism in which the power plant turns the saline water into fresh water is of distillation kind, the amount of salinity of the outflow does not dramatically increase. As it can be seen for the worst case in Figure 10, which is the surface discharge, the amount of salinity change at the 200-meter distance hardly reaches the amount of 3 psu. Therefore, for other scenarios, the change in salinity distribution is not presented.

5. Conclusion

In this study, a three-dimensional finite volume circulation model was employed to study the dilution

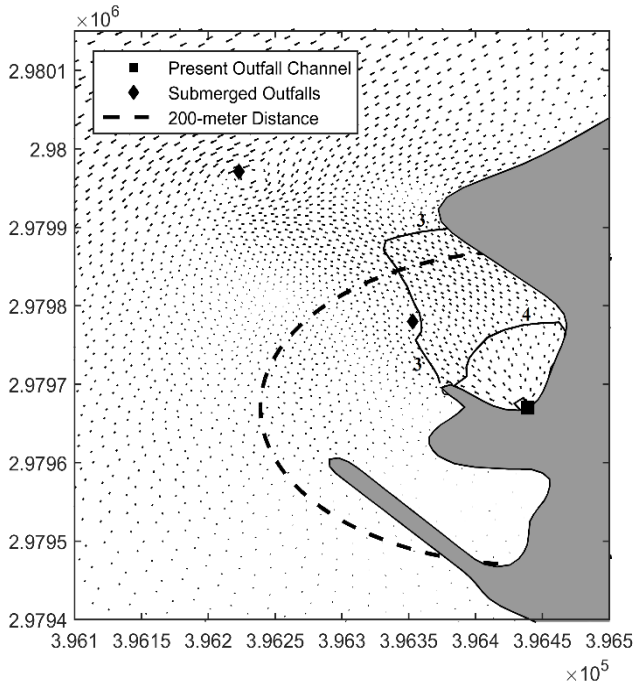

Figure 10: Salinity dispersion from surface discharge point

of outflow from a power plant with ambient water body. This invaluable tool enables us to easily model the current situation to not only better understand the circulation pattern but also plan for the optimum way of discharging.

After calibrating the far-field model based on water elevation and current speed, a local model with smaller mesh size was employed, then temperature, salinity, tide, and wind were nested into the local model. Local model was then calibrated using the CTD field data to determine horizontal mixing coefficient with respect to the actual discharging method—surface discharge. Calibrating the local model, two scenarios were used with respect to both depth and currents. Moreover, discharging method altered to submerged one to better dilute the outflow.

It was shown that by moving the outfall location to deeper areas of the sea where tidal currents are stronger, the dilution rate increases, and therefore the plume disperse more quickly. However, when the regulation guidelines are concerned, only the 10-meter-outfall can be applied.

Salinity, on the other hand, is of the least importance, since the process of producing fresh water—in this case—makes the outflow with only a little extra amount of salt compared to the ambient salinity level.

6. References

1- Ahmad, N., & Baddour, R. E., (2014), *A review of sources, effects, disposal methods, and regulations of brine into marine environments*, Journal of Ocean & coastal management, 87, 1-7.

2- Anschutz, P., Blanc, G., Chatin, F., Geiller, M., & Pierret, M.-C., (1999), *Hydrographic changes during 20 years in the brine-filled basins of the Red Sea*, Journal of Deep Sea Research Part I: Oceanographic Research Papers, 46(10), 1779-1792.

3- Niepelt, A., Bleninger, T., & Jirka, G., (2008), *Desalination brine discharge modelling. Coupling of hydrodynamic models for brine discharge analysis*, Paper presented at the 5th International Conference on Marine Waste Water Discharges and Coastal Environment, Croatia.

4- Fischer, H. B., List, J. E., Koh, C. R., Imberger, J., & Brooks, N. H., (2013), *Mixing in inland and coastal waters*: Elsevier.

5- Grace, R. A., (1978), *Marine outfall systems: planning, design, and construction*: Prentice-Hall.

6- Sharp, J. J., (1989), *Discussion of "Initial Dilution of Horizontal Jet in Crossflow" by Joseph HW Lee and Peter Neville-Jones (May, 1987, Vol. 113, No. 5)*, Journal of Hydraulic Engineering, 115(2), 282-284.

7- Purnama, A., & Al-Barwani, H., (2006), *Spreading of brine waste discharges into the Gulf of Oman*, Journal of Desalination, 195(1-3), 26-31.

8- Kay, A., (1997), *Advection-diffusion in reversing and oscillating flows: 2. Flows with multiple reversals*, IMA journal of applied mathematics, 58(3), 185-210.

9- Macdonald, G. J., & Weisman, R. N., (1977), *Oxygen-sag in a tidal river*, Journal of the Environmental Engineering Division, 103(3), 473-488.

10- Purnalna, A., Al-Barwani, H., & Al-Lawatia, M., (2003), *Modeling dispersion of brine waste discharges from a coastal desalination plant*, Journal of Desalination, 155(1), 41-47.

11- Purnama, A., & Shao, D., (2015), *Modeling brine discharge dispersion from two adjacent desalination outfalls in coastal waters* Journal of Desalination, 362, 68-73.

12- Mohamed, K. A., (2007), *Model investigation on the impact of raha beach development on Umm Al Nar Power and Desalination Plant*, Journal of Desalination, 212(1-3), 357-366.

13- Sun, Y.-J., Cho, Y.-K., Park, K.-S., Yoon, S.-M., & Moon, J.-K., (2012), *Simulation of brine discharge near sea farms in the Korea Strait*, Journal of Desalination and Water Treatment, 43(1-3), 201-211.

14- Mahmoudov, M., Chegini, V., & Montazeri Namin, M., (2011), *Three-Dimensional Simulation of Qeshm Channel Currents*, Journal of Persian Gulf, 2(3), 9-16.

15- Foreman, M. G. G., (1979), *Manual for tidal heights analysis and prediction: Institute of Ocean Sciences*, Patricia Bay.

16- Najafi, H. S., & Noye, B. J., (1997), *Modelling tides in the Persian Gulf using dynamic nesting.*

17- Chen, C., Liu, H., & Beardsley, R. C., (2003), *An unstructured grid, finite-volume, three-dimensional, primitive equations ocean model: application to coastal ocean and estuaries.* Journal of atmospheric and oceanic technology, 20(1), 159-186.

18- Smagorinsky, J., (1963), *General circulation experiments with the primitive equations: I. The basic experiment.* Monthly weather review, 91(3), 99-164.

19- Mellor, G. L., & Yamada, T., (1982), *Development of a turbulence closure model for geophysical fluid problems.* Reviews of Geophysics, 20(4), 851-875.
20- Memari, S., & Siadatmousavi, S. M., (2017), *Modeling the effects on mangrove forests on hydrodynamics of the Khuran Channel*. 19th Marine Industries Conference, Kish, Iran.
21- https://www.ecmwf.int/
22- https://hycom.org/
23- Padman, Laurie, and S. Erofeeva., (2005), *Tide Model Driver (TMD) Manual*. Earth and Space Research.
24- http://www.ncc.org.ir/
25- https://www.gebco.net/
26- Salgueiro, D., de Pablo, H., Nevesa, R., & Mateus, M., (2015), *Modelling the thermal effluent of a near coast power plant (Sines, Portugal).* Revista de Gestão Costeira Integrada-Journal of Integrated Coastal Zone Management, 15(4).

INTERNATIONAL JOURNAL OF
COASTAL& OFFSHORE ENGINEERING IJCOE Vol.3 /No. 4/Winter 2018 (37-44)

Available online at: http://ijcoe.org/browse.php?a_code=A-10-117-1&sid=1&slc_lang=en

An Artificial Neural Network for Prediction of Front Slope Recession in Berm Breakwaters

Alireza Sadat Hosseini[1*], Mehdi Shafieefar[2], Omid Alizadeh[3]

[1]PhD Candidate, University of Tehran; a.sadat@ut.ac.ir*
[2]Professor, TarbiatModares University; shafiee@modares .ac.ir
3PhD Candidate, University of Tehran; o.alizadeh@ut.ac.ir

ARTICLE INFO

Article History:
Received: 9 Oct. 2017
Accepted: 17 Mar. 2018

Keywords:
Recession
Berm breakwater
Artificial neural network

ABSTRACT

Berm breakwaters are used as protective structures against the wave attack where larger quarry materials as armor stone is scarce, or large quarry materials are available but using berm breakwater lowers the costs considerably. In addition, wave overtopping in berm breakwaters are significantly lower than the traditional ones for equal crest level because of the wave energy dissipation on the berm.The most important design parameter of berm breakwaters is its seaward berm recession which has to be well estimated. In this paper a method has been developed to estimate the front slope recession of berm breakwaters using artificial neural networks with high accuracy. Four different available data-sets from four experimental tests are used to cover wide range of sea states and structural parameters. The network is trained and validated against this database of 1039 data. Comparisons is made between the ANN model and recent empirical formulae to show the preference of new ANN model.

1. Introduction

Unlike the conventional rock armored breakwaters, berm breakwaters have a large porous berm at their seaward side which can be reshaped during the wave attack to a stable S-shaped form. PIANC (2003) report "State-of the-Art of Designing and Constructing Berm Breakwaters" provided proper descriptions about the design and construction of berm breakwaters. In the design of berm breakwaters finding the appropriate berm width is undoubtedly associated with well estimation of its seaward berm recession. Figure 1 shows the cross sectional of initial and reshaped profile, together with the recession parameter in a berm breakwater. Estimating the optimized berm width results in more economical design.

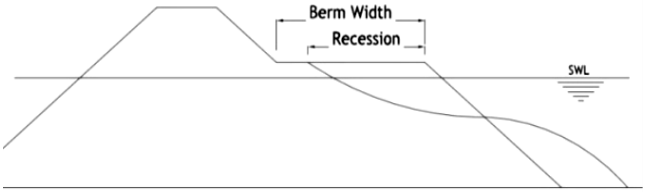

Figure 1.schematic of the berm breakwater section and the recession parameter

A number of researchers propounded methods for calculating the berm recession. There are some numerical methods proposed by Van der Meer (1992), Van Gent (1995) and Archetti and Lamberti (1996). Besides, there are some empirical formulas. For instance, Hall and Kao (1991) presented a formula considering the effect of rounded stones fraction in the armor, and stone gradation on the reshaping of berm breakwaters. Tørum (1998) proposed a formula based on the results of a small model test on different projects which have been carried out in different laboratories as a function of stability number (H_0T_0). A more complete variation of Tørum (1998) formula, including water depth and stone gradation was presented by Tørum et al. (2003). Sigurdarson et al. (2007) suggested a simple formula as a function of stability number (H_0T_0) for multilayer berm breakwaters, based on Tørum (1998) dataset. Lykke Andersen and Burcharth (2009) put forward a semi-empirical recession formula which was at the continuance of Lykke Andersen (2006) researches on his numerous model tests carried out on homogeneous berm breakwaters. Sigurdarson and Van der Meer (2011) showed that the main parameter that describes the recession, Rec, is the stability number Hs/ΔDn50. Moghim et al. (2011) presented a simple formula, as a function of modified stability number ($H_0T_0^{0.5}$) which was proposed based on their experiments. Fundamental to the Shekari (2013) experiments, Shekari and Shafieefar (2013) presented an empirical

formula, which has been ameliorated by Shafieefar and Shekari (2014). Sadat Hosseini (2013) presented a recession formula, employing M5' machine learning approach on the amalgamation of Moghim (2011) and Shekari (2013) datasets. Van Gent (2013) performed physical model tests in a wave flume at Deltares, Delft. His tests were focused distinctively on the upper and lower slope of the berm elevation. In Van Gent (2013) studies, the impact of the slope angle (1:2 and 1:4), berm width, berm level, and also the wave steepness has been investigated. He proposed a recession formula based on the damage parameter and the berm elevation with respect to the water level. Moghim and Alizadeh (2014) presented a new berm recession formula based on the proportionality of the maximum wave momentum flux at the toe of the structure and the berm recession. Van der Meer and Sigurdarson (2016) presented a book as a guidance on design and construction of berm breakwaters as the result of their cooperation, both in the scientific as well as the practical field.

Most of these studies ended to different formulas which show dissimilarities in recession parameter approximation. The aim of this study is to find a more comprehensive algorithm, alternative to the foregoing empirical formulas, aim at minimizing the berm recession estimation error, using artificial neural networks.

2. Description of database and parameters involved

The Recession database which is used for constructing the ANN includes a total of 1039 data which are obtained from the experiments carried out by Lykke Andersen (2006) (474 data points), Motalebi (2010) (120 data points), Moghim (2011) (113 data points) and Shekari (2013) (332 data points).

Lykke Andersen (2006) model tests were performed at Aalborg University. The main part of Moghim (2011) experiments has been carried out in the Shore Protection Division of Soil Conservation and Watershed Management Research Institute (SCWMRI) wave flume that is equipped with a DHI irregular wave generation system. Motalebi (2010) and Shekari (2013) carried out their tests in the wave channel at the Hydraulic Laboratory of Civil and Environmental Engineering department of Tarbiat Modares University.

Ranges of non-dimensional parameters, used in ANN set-up, for these four model tests are presented in Table 1.

Table 1. Ranges of main non-dimensional parameters for each set of data

Parameter		Range			
		Lykke Andersen (2006)	Motalebi (2010)	Moghim (2011)	Shekari (2013)
Stability number	H_0	1.35 to 4.86	1.87 to 4.23	1.53 to 4.03	1.57 to 3.87
Non-dimensional mean wave period	T_0	19.9 to 39.6	20.7 to 27.3	24 to 37.4	15.6 to 29.3
Non-dimensional water depth at the toe of the structure	d/D_{n50}	8.8 to 22.3	8.0 to 16.5	11.8 to 16.5	8.0 to 16.5
Non-dimensional berm width	B/D_{n50}	7.7 to 33.0	8.0 to 17.6	23.5 to 23.5	12.0 to 26.5
Non-dimensional berm elevation above SWL	h_b/D_{n50}	-6.1 to 2.0	0.0 to 4.6	0.9 to 4.4	0.4 to 4.12
Number of incident waves	N	3000 to 3000	3000 to 3000	500 to 6000	500 to 6000
Gradation factor	f_g	1.35 to 1.45	1.82 to 1.82	1.5 to 1.5	1.5 to 3.32
Wave steepness	S_{om}	0.0149 to 0.0638	0.0313 to 0.0511	0.0130 to 0.0724	0.019 to 0.122

3. Artificial Neural Network Modeling and Results

3.1. General

Artificial Neural networks (ANN) are a group of machine learning approaches which can be used for a variety of data mining tasks in order to model and solve the problems in technical and scientific fields. Multi Layer Perceptron networks are type of neural networks which are set up in some layers within each of these, there are one or more neurons as processing units. When the network layers connect to each other in one direction only, the network is called a standard multi-layer feed-forward neural network. The network consists of a topology graph of neurons. The first layer, which is called the input layer, consists of a number of neurons equal to the number of input parameters. The last layer is called the output layer which made up of a number of neurons equal to the number of output parameters to be predicted. The inputs and outputs are weighed by weights and shifted by bias factor specific to each neuron. There are hidden layers between the input and output layers consists of neurons, each of which computes a function of the inputs carried on the in-edges and sends the weighted sum of the outputs of the preceding layer on its out-edges. This output then is used as an input for the next layer neurons. For the output layer often a linear activation function is used (Haykin, 1994) and the final prediction of the neural

network is provided by the neurons of the output layer.

3.2. The Model Architecture

The architecture of the model has been achieved through an algorithm, which is explained as follow. The general solution algorithm is that, when the error criterion, which is in here the root mean squared error ("RMSE", Eq. (1)), of the ANN becomes less than that of the previous network, which is built prior to the present network, that ANN will be chosen as the best network.

$$RMSE = \sqrt{\sum_{i}^{N}\left[\left(\mathrm{Re}c / D_{n50}\right)_{obs,i} - \left(\mathrm{Re}c / D_{n50}\right)_{ANN,i}\right]^2} \quad (2)$$

In Eq. (1), indices obs and ANN refer to the experimental and predicted data by ANN model, respectfully. Index *i* denotes the *i*-th data and *N* is the number of data in training set or testing set.

Therefore, the whole dataset is split into training and testing set. At first, the training data is applied to train the network. The RMSE is calculated and the weights and bias are acquired. Then, a new distribution of the data is selected. In other words, if 20% of the data are selected as the testing data, the dataset is divided into 5 partitions, in which, 1 partition is assigned for testing and 4 others for training. At each step, a new distribution which consists of 20 percent of data is selected. This changes in selection, not only includes the selected partition, but, also the members of the partitioned set can be Changed. The initial weight and bias of the new network is set equal to those of the accepted network. This new network is trained with the new distribution of data. The new network is accepted if it's RMSE error is less than the previous one, as mentioned before. Otherwise, the previous selected network remain as the benchmark and again, this process is repeated with the new distribution of the data. Any changes in data distribution allows the network to be trained and tested with the lowest error, regardless of how the data have been chosen. Hence, with this method, the finally chosen network has the minimum errors. History of change in network's weights and bias could be efficacious in finding the best network with the minimum RMSE. In other words, some networks may temporarily increase the network error, but in upcoming steps, the network error could be less than the initial state. It could be said that, redirecting the decline in weights, can increase the likelihood of encountering an absolute minimum in network error. Thus, in this research, in the process of finding the best network, this feature is included that the networks, which have not fewer errors in comparison to their previous one, could be accepted (redirect to an absolute minimum) by determining a certain probability of occurrence in the process.

Avoiding to be trapped in local minimum of the network error, makes it rational to let the network to examine some other paths toward the other minimum of the network error. To carry out this idea, despite of the main procedure, some networks within a pre-determined range are accepted.

In order to identify the optimum number of hidden neurons in ANN model in the process of training and testing according to the above algorithm, an analysis of the network performance variability was carried out. Figure 2 shows the variation in RMSE value with increasing number of hidden neurons.

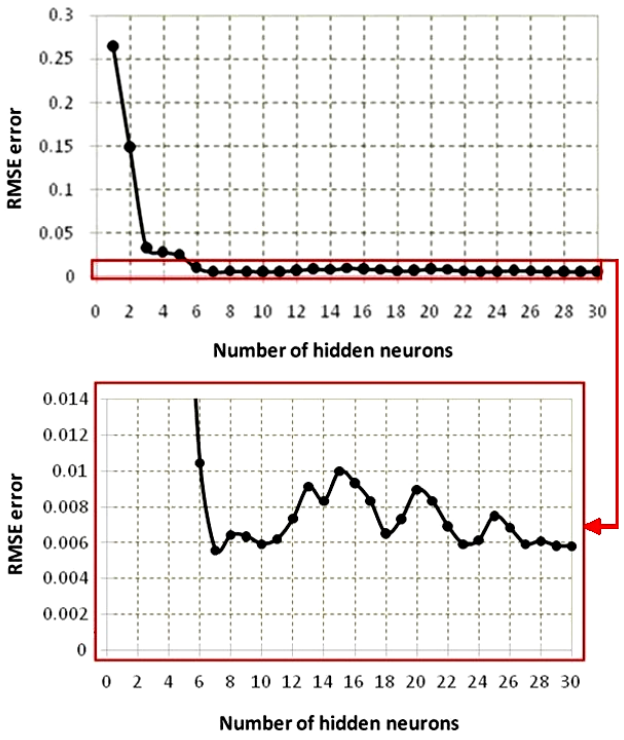

Figure 2. Mean RMSE value as functions of the number of hidden neurons in ANN simulation processes (The diagram on the right shows fluctuations of RMSE with more precision in Y-axis)

It can be observed that the RMSE stabilizes around the average value of 0.007 for a number of training–testing processes with number of neurons greater than 5. The optimum value of RMSE obtained when training–testing processes held with 7 hidden neurons.

Based on the process explained above, the ANN model is built with the following fundamental characteristics:

- Multilayer network, based on a "feed-forward back-propagation" learning algorithm;
- Static network (absence of delays and feedbacks);
- Structure and layers: the input vector with 7 elements, 1 hidden layer with 7 hidden neurons and 1 output neuron, the non-dimensional recession parameter;

- Hidden neurons transfer function: hyperbolic tangent sigmoid transfer function;
- Output neuron transfer function: linear transfer function;
- Data structures: the arrays of data can be provided to the network as "concurrent vectors", *i.e.* rows of a matrix in a random order; as long as a neural network is static, the way the arrays are provided to the ANN (i.e. subsequent or concurrent way) has no relevance for the simulation while for the training phase it is very important since the connections weights are updated accordingly; in fact, connections weights may be updated either at the end of each training epoch or within each epoch for each new test;
- Training style: "batch training", connections weights and biases are updated at the end of each training epoch, just once the ANN has read all the input data;
- Training algorithm: Levenberg–Marquardt algorithm;
- Learning algorithm: momentum gradient descent back-propagation algorithm.

In Figure 3 the logic layout of ANN configuration is schematized.

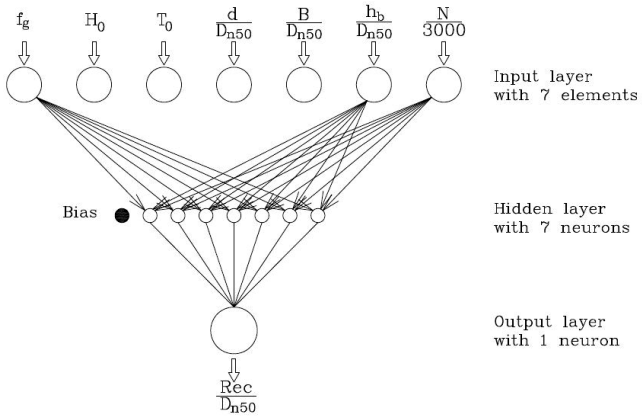

Figure 3. Logic layout of the ANN configuration

3.3. Input Parameters

The input parameters, should include a synthesis of sea, such as wave height, wave period, water depth at the toe of the structure and storm duration; and also the structural characteristics of the breakwater itself including armor stone size, berm elevation from still water level, initial berm width and seaward slope of the initial profile. The choice of the parameters was initially based on the previous simplest non-dimensional parameters in researches on prediction of reshaping parameters in berm breakwaters. Besides, Table 2 illustrates these seven non-dimensional parameters. Note that in Table 2, $\Delta = \rho_s / \rho_w - 1$, which is the relative buoyant density; ρ_s is the density of stone and ρ_w is the density of water.

Table 2. Range of non-dimensional parameters used as the *input* parameters in ANN.

dimensionless parameter	min	max	mean
f_g	1.35	3.32	1.56
$H_0=H_s/\Delta D_{n50}$	1.35	4.86	2.93
$T_0= T_m (g/D_{n50})^{0.5}$	15.6	39.6	25.74
d/D_{n50}	8.0	22.33	14.93
B/D_{n50}	7.73	33.0	19.38
h_b/D_{n50}	-6.1	4.6	1.81
$N/3000$	0.167	2.0	0.994

3.4. Weights and Biases

The main products of the trained ANN are its weights and bias elements, which allow using the network as a predictive model. These elements can be matrixes, vectors or scalars which contain the values attributed to the connections among neurons by the model itself during the training process. The weight matrixes are illustrated in Table 3.

Table 3. Weight matrixes of the connections

IW{1,1}, size: 7×7						
10.051	1.444	0.53	-4.973	123.936	-117.21	7.439
35.054	2.016	0.227	3.098	13.415	-14.671	8.206
1272.168	291.355	-289.95	327.002	187.891	-231.64	519.529
44.48	-1.429	-0.081	21.886	0.111	12.015	-16.419
0.09	0.355	0.115	0.217	0.012	0.081	-0.008
415.141	-278.55	68.195	-273.74	24.88	-11.678	49.442
-413.753	-266.75	16.62	-297.63	-545.46	-416.32	242.343
LW{1,1}, size: 1×7						
0.223	-0.201	0.032	-0.128	2.305	0.029	0.059
B{1,1}, size: 7×1						
-36.213	22.984	967.763	15.749	0.014	432.731	-342.73
B{2,1}, size: 1×1						
-0.1182						

In this study, we have 4 elements: the matrix of "Input Weights" (IW, of dimensions 7×7) to connect input parameters to hidden neurons, the matrix of "Layer Weights" (LW, a single row of dimensions 1×7) which connects hidden neurons to the output neuron, the bias vector (7×1) for hidden layer and the bias scalar (1×1) for the output layer. 64 weights (7×7+1×7+7×1+1×1) associated to connections are employed overall. It is important to note that, before entering into training, the network normalizes the input elements and the output, according to the corresponding minimum and maximum values.

3.5. Performance of the model

In order to investigate the performance of the new ANN model, the observed non-dimensional recession (Rec/D_{n50} observed) is illustrated versus the predicted non-dimensional recession (Rec/D_{n50} predicted) in Figure 4.

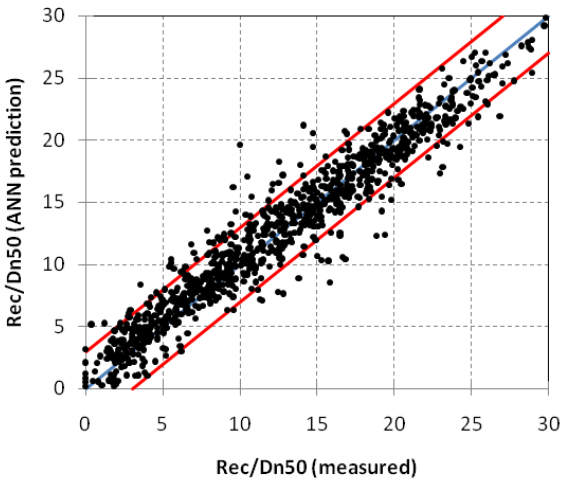

Figure 4. Observations versus ANN predictions for *Rec*/D_{n50} parameter

It is evident from Figure 4 that, the predictions of the ANN model are reasonably accurate in all the range of dataset. The central line stands for the perfect correspondence among predicted and experimental values and the external lines represent the 90 percent confidence boundaries. This indicative 90% confidence band indicates that there are few data points for which the ANN predictions are a factor 10 (or more) larger/smaller than the corresponding observations. Also, it is obvious from Figure 4 that, there is a good degree of symmetry provided by the ANN model. This is also apparent from Figure 5, which represents the error frequency distribution histogram.

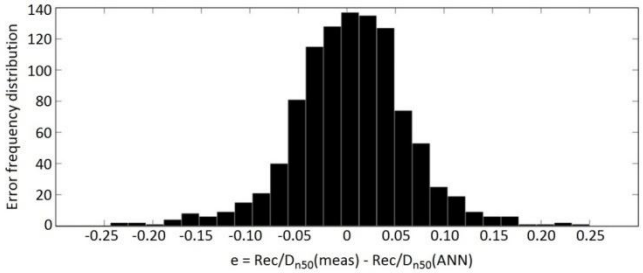

Figure 5. The error (Difference e = *Rec*/D_{n50}(measured) - *Rec*/D_{n50}(ANN prediction)) frequency distribution histogram

In order to make a quantitative estimate of the ANN model accuracy, the correlation of coefficients (R^2), the above-mentioned RMSE and the refined index of model performance (d_r) given by Willmott et al. (2012), compared to the old version of "WI" represented by Willmott (1981), are calculated.

The value of R^2 is 0.93 and the RMSE value is 0.055, which shows that, the average magnitude of the forecast errors are rigorously low. The value of 0.91 for dr, which is a reformulation of Willmott's index of agreement (WI), denotes that the model-estimated deviations about average values of observed data are strong estimates of the observed deviations.

4. Comparison among the new ANN model and recent empirical formulas

The aim of the present section is to provide a comparison among ANN performance and traditional prediction formulae.

Table 4 reports the quantitative results of these simulations in terms of R^2, RMSE and d_r values. The ANN shows more accurate predictions in comparison to the other formulas.

Table 4. Statistical indices (R2, RMSE and dr values) for the ANN model versus the other formulas

Models	R^2	*RMSE*	d_r
Hall and Kao (1991)	0.71	6.47	0.53
Tørum et al. (2003)	0.72	7.49	0.27
Sigurdarson et al. (2007)	0.76	5.24	0.55
Lykke Andersen and Burcharth (2009)	0.86	3.81	0.73
Moghim et al. (2011)	0.81	3.14	0.76
Shekari and Shafieefar (2013)	0.79	7.51	0.39
Sadat Hosseini (2013)	0.88	2.07	0.84
Shafieefar and Shekari (2014)	0.82	3.38	0.71
Moghim and Alizadeh (2014)	0.87	2.53	0.83
ANN (This research)	0.93	0.006	0.91

According to the Table 4, The results from the new ANN model, give much less error than the closed form formulas given by the other researchers. So it is possible to predict the berm recession by using the ANN model more accurate than the formulas.

Figure 6 to 14 present comparisons between the distribution of predicted non-dimensional recession versus corresponding measured values from previous works with the ANN model.

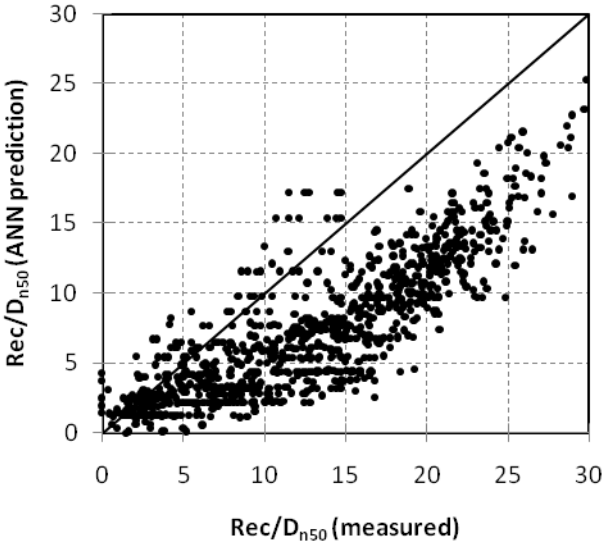

Figure 6. Observations versus predictions by Hall and Kao (1991) for *Rec*/D_{n50} parameter

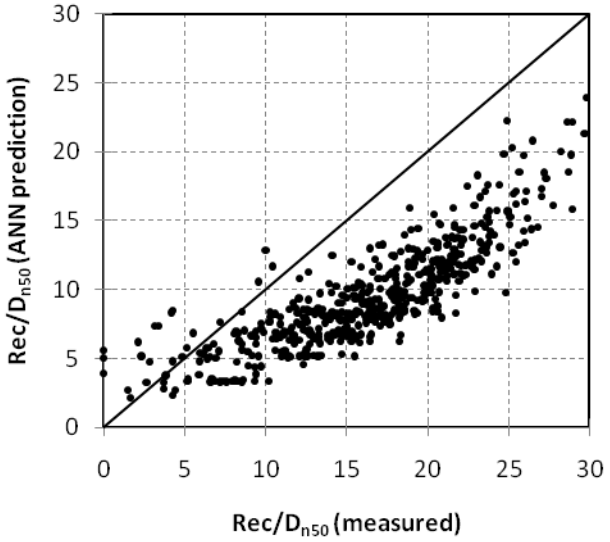

Figure 7. Observations versus predictions by Tørum et al. (2003) for Rec/D_{n50} parameter

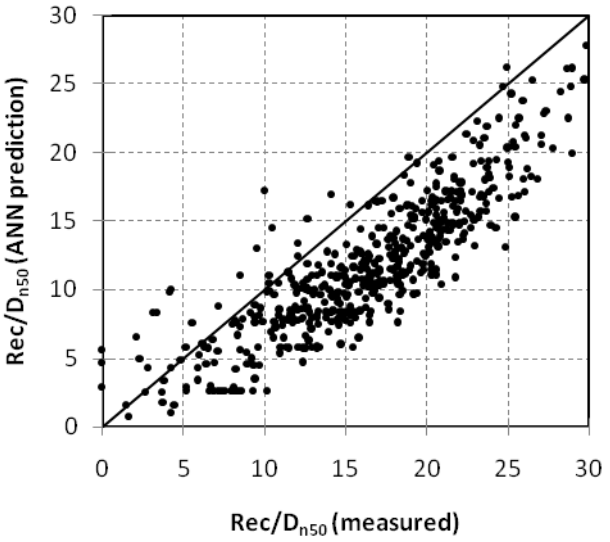

Figure 8. Observations versus predictions by Sigurdarson et al. (2007) for Rec/D_{n50} parameter

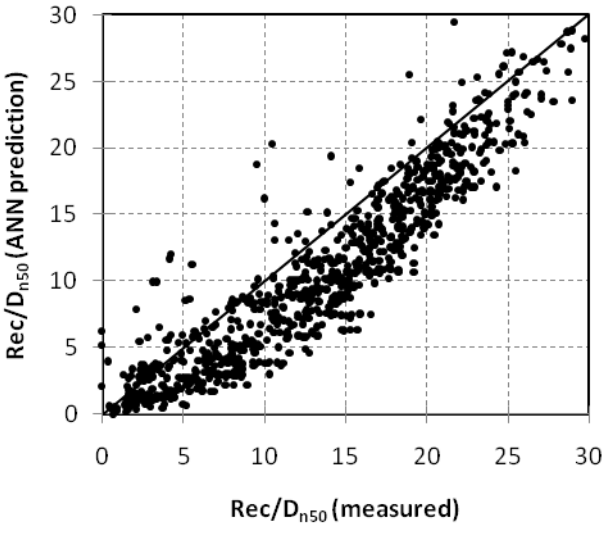

Figure 9. Observations versus predictions by Lykke Andersen and Burchart (2009) for Rec/D_{n50} parameter

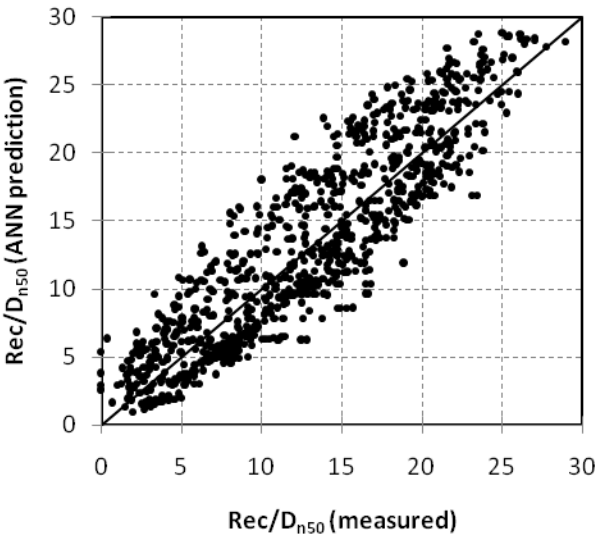

Figure 10. Observations versus predictions by Moghim et al. (2011) for Rec/D_{n50} parameter

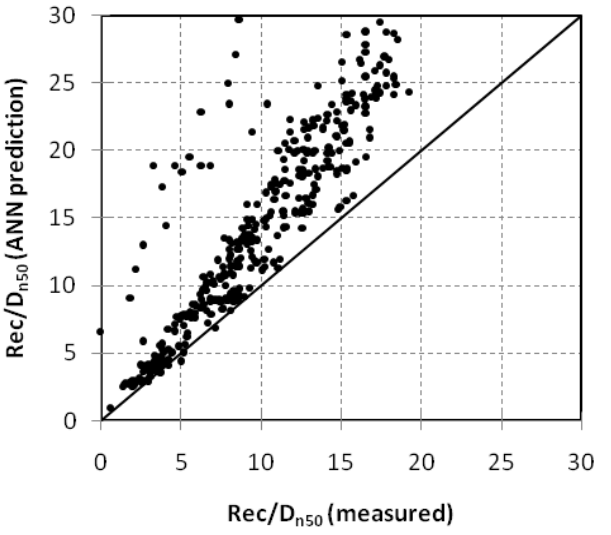

Figure 11. Observations versus predictions by Shekari and Shafieefar (2013) for Rec/D_{n50} parameter

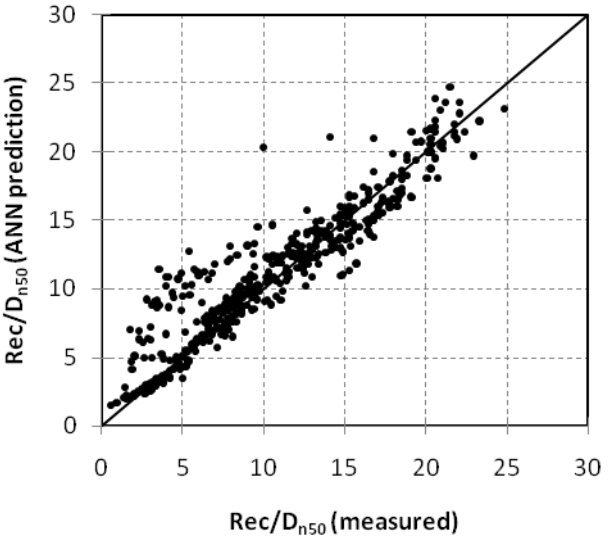

Figure 12. Observations versus predictions by Sadat Hosseini (2013) for Rec/D_{n50} parameter

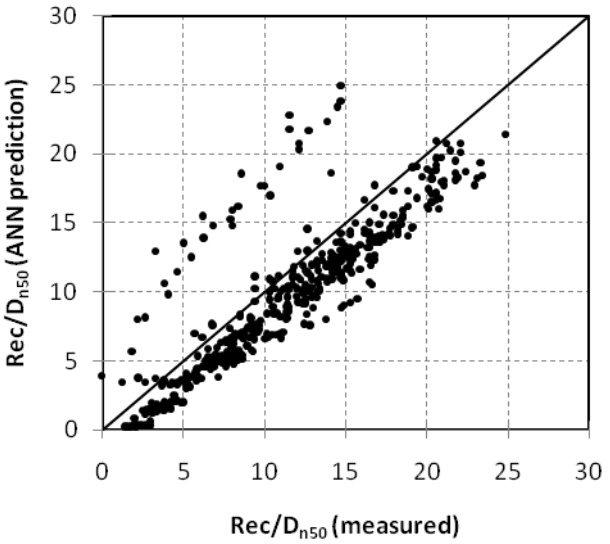

Figure 13. Observations versus predictions by Shafieefar and Shekari (2014) for *Rec*/D_{n50} parameter

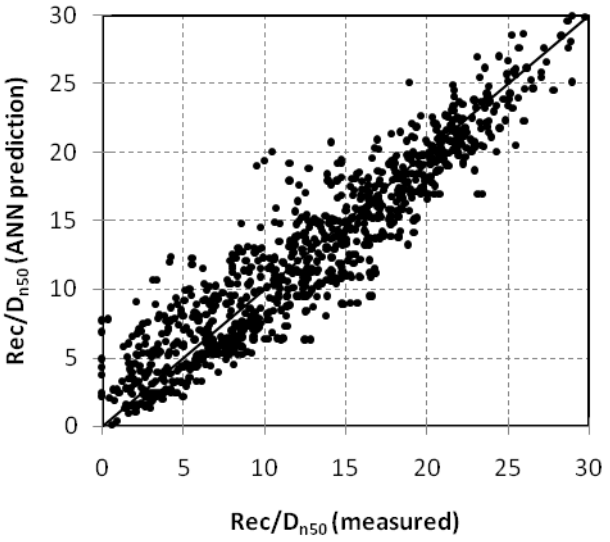

Figure 14. Observations versus predictions by Moghim and Alizadeh (2014) for *Rec*/D_{n50} parameter

5. Summary and Conclusions

A neural network based prediction method has been developed for the estimation of the seaward berm recession in berm breakwaters. A strong technique based on the reduction of the networks' RMSE which are built on the split and redistributed data have been applied to reach to the optimum ANN. The presented results show that Neural Networks can successfully be used to model the relationship between the input parameters involved in berm recession and the one obtained from experimental models. The neural network model constructed herein is based on the database from experiments performed by Lykke Andersen (2006), Motalebi (2010), Moghim (2011) and Shekari (2013). It is illustrated that the agreement between the predicted and the measured berm recession is well acceptable.

Acknowledgements

The authors would like to acknowledge Dr. T. Lykke Andersen, Dr. M. R. Shekari, Dr. M. N. Moghim and Eng. A. Motalebi for providing their data.

8. References

Archetti, R., Lamberti, A., (1996), *Parametrizzazione del profile di frangifluttiberma*, Proc. Congresso AIOM, Padova.

Hall, K., Kao, S., (1991), *A study of the stability of dynamically stable breakwaters*, Canadian Journal of Civil Engineering, Vol.18, p.916–925.

Haykin, S., (1994), *Neural networks: a comprehensive foundation*, Macmillan College Publishing Company, Inc.

Lykke Andersen, T., (2006), *Hydraulic Response of Rubble Mound Breakwaters (Scale Effects - Berm Breakwaters)*, (Doctoral Thesis) University of Aalborg, Denmark.

Lykke Andersen, T., Burcharth, H.F., (2009), *A new formula for front slope recession of berm breakwaters*,Coastal Engineering,Vol.57 (4), p.359–374.

Moghim, M.N., (2009), *Experimental study of hydraulic stability of reshaping berm breakwaters*, (PhD thesis) TarbiatModares University. (In Persian)

Moghim, M.N., Alizadeh, F., (2014), *Hydraulic stability of reshaping berm breakwaters using the wave momentum flux parameter*,Coastal Engineering,Vol.83, p.56–64.

Moghim,M.N., Shafieefar, M., Tørum, A., Chegini, V., (2011),*A new formula for the sea stateand structural parameters influencing the stability of homogeneous reshaping berm breakwaters*, Coastal Engineering, Vol.58 (8), p.706–721.

Motalebi, A., (2010), *Experimental Study of Investigating the Influence of Armor Stone Size in Stability of Berm Breakwaters*, (Master Thesis) TarbiatModares University. (In Persian)

PIANC, (2003), *State-of-the-Art of Designing and Constructing Berm Breakwaters*, PIANC, Brussels.

Sadat Hosseini, A., (2013), *Presentation of a smart model to estimate the reshaped profile of berm breakwater using experimental data*, (Master Thesis) TarbiatModares University. (In Persian)

Shafieefar, M., Shekari, M.R, (2014), *An experimental study on the parameterization of reshaped seaward profile of berm breakwaters*, Coastal Engineering, Vol.91, p.123–139.

Shekari, M.R, Shafieefar, M., (2013), *An experimental study on the reshaping of berm breakwaters under irregular wave attacks*, Applied Ocean Research, Vol.42, p.16–23.

Shekari, M.R., (2013), *Experimental investigation of hydraulic stability of single berm and double berm breakwaters*, (PhD thesis) TarbiatModares University. (In Persian)

Sigurdarson, S., van der Meer, J.W., (2011), *Front Slope Stability of the Icelandic-type Berm Breakwater*, Proceedings of Coastal Structures 2011, ASCE.

Sigurdarson, S., van der Meer, J.W., Tørum, A., Tomasicchio, R., (2008), *Berm Recession of the Icelandic-type Berm Breakwater*, Proc. ICCE. ASCE, Hamburg.

Tørum, A., (1998),*On the stability of berm breakwaters in shallow and deep water*, Proc. 26th International Conference on Coastal Engineering, ASCE, Copehagen, Denmark, p.1435–1448.

Tørum, A., Kuhnen, F., Menze, A., (2003), *On berm breakwaters, stability, scour, overtopping*,Coastal Engineering, Vol.49,p.209–238(September Issue).

Van der Meer, J.W., (1992), *Stability of seaward slope of berm breakwaters*, Coastal Engineering, Vol.16, p.205-234.

Van der Meer, J.W., Sigurdarson, S., (2016), *Design and Construction of Berm Breakwaters*, World Scientific, Advanced Series on Ocean Engineering, Volume 40, ISBN 978-981-4749-60-2.

Van Gent, M.R.A., (1995), *Rock stability of rubble mound breakwaters with a berm*, Coastal Engineering,Vol. 78, p. 35–45.

Van Gent, M.R.A., (1995), *Wave Interaction with Permeable Coastal Structures*, Delft University of Technology.

Willmott, C.J., (1981), *On the validation of models*, Physical Geography, Vol.2, p.184–194.

Willmott, C.J., Robeson, S.M., Matsuura, K., (2012), *Short Communication A refined index of model performance*, International Journal of Climatology, Vol.32, p.2088–2094.

INTERNATIONAL JOURNAL OF
COASTAL & OFFSHORE ENGINEERING
IJCOE Vol.3 /No. 4 /Winter 2018 (45-55)

Available online at: http://ijcoe.org/browse.php?a_code=A-10-183-1&sid=1&slc_lang=en

Study of Flow Characteristics around a Near-Wall Circular Cylinder Subjected to a Steady Cross-Flow

Mohammad Amin Salehi[1], Said Mazaheri[2*], Mohammad Hossein Kazeminezhad[3]

[1] *Ocean Engineering & Technology, Iranian National Institute for Oceanography and Atmospheric Science, Tehran, Iran, mascivil9@gmail.com*
[2] [*] *Corresponding Author: Ocean Engineering & Technology, Iranian National Institute for Oceanography and Atmospheric Science, Tehran, Iran, said.mazaheri@inio.ac.ir*
[3] *Ocean Engineering & Technology, Iranian National Institute for Oceanography and Atmospheric Science, Tehran, Iran, mkazeminezhad@inio.ac.ir*

ARTICLE INFO

Article History:
Received: 7 Jan. 2018
Accepted: 6 Mar. 2018

Keywords:
pressure distribution
force coefficients
separation angle
stagnation angle
vortex shedding suppression

ABSTRACT

Three-dimensional RANS simulations are employed numerically to study flow characteristics around a near-wall circular cylinder for varying gap-to-diameter (G/D) ratios (Where G is the gap between the cylinder and the wall and D is the cylinder diameter) and at Reynolds numbers from 100 to 3900. Pressure distribution around the circular cylinder, base pressure magnitude, separation and stagnation angles, force coefficients and Strouhal numbers were calculated and compared for all of the cases. Inception of vortex shedding can be seen when a sudden decrease in the maximum of positive pressure coefficient occurs. Vortex shedding mechanism and possibility of suppression further investigated via comparison of swirling strength in upper and lower vortex regions through parameter Λ, which signifies vortical activity and balance with respect to the wake center-line and also the flow type parameter, λ, representing the extensional strain dominance in the wake flow and gap flow. Vortex shedding suppression observed for the cases with the high unbalance vorticity content in the vortex regions, namely for $\Lambda \geq 2$.

1. Introduction

Marine pipelines are extensively used to transport oil and gas products between offshore and onshore especially in shallow to deep waters. Pipeline free spans can be formed as a result of local scour beneath pipeline or irregularity of seabed. Vortex shedding phenomenon on a free span pipeline results in fluctuations in hydrodynamic forces acting on it. Vortex induced vibration of a cylinder subjected to steady flow is highly influenced by fluctuating lift fluid forces, damages the pipeline structure and the junctions due to fatigue. To ensure avoiding such harmful effect on the pipelines, managing the occurrence of vortex shedding is attainable through realizing the characteristics of flow around a circular cylinder near a plane boundary.

Many researchers focused on the pressure distribution and force components around a circular cylinder to describe the gap flow and wake flow characteristics. Batham [1] measured mean and fluctuating pressure distributions around a circular cylinder with smooth and rough surfaces at Reynolds number range of 1.11×10^5 to 2.35×10^5 under uniform and turbulent streams. It had been found that the introduction of free-stream turbulence at this range of Reynolds number suppresses the vortex shedding on the smooth cylinder due to three-dimensionality and small axial correlations at separation and also increases the pressure downstream of the separation point. Pressure distribution around smooth and rough cylinders found to be different for uniform incident flows, unlike the Pressure distribution pattern around smooth and rough cylinders under turbulent flows, which was observed to be similar. It can be concluded that the pressure field patterns have been largely influenced by the processes of boundary layer and shear layer transition. Bearman and Zdravkovic [2] experimentally investigated flow around a circular cylinder at various heights above a plane boundary experimentally and found out that flow around a circular cylinder near plane boundary depends on cylinder Reynolds number, gap ratio (G/D) and characteristics of the boundary layer. Distributions of mean pressure around the cylinder and along the plate were measured at a Reynolds number, based on the cylinder diameter, of 4.5×10^5. Spectral analysis of hot-wire signals

demonstrated that regular vortex shedding was suppressed for all gaps less than about 0.3 cylinder diameters and for gaps greater than 0.3 the Strouhal number was found to be remarkably constant. Zdravkovic [3] measured the lift and drag forces on circular cylinders fitted with end plates in a wind tunnel. The gap between the cylinder and the wall, G, the thickness of the turbulent boundary layer along the wall, δ, and Re were varied in the following ranges: $0 < G/D < 2$, $12 < \delta/D < 0.97$ and $4.8 \times l0^4 < Re < 3 \times l0^5$. The lift and drag coefficients were presented in terms of a new variable G/δ. It was found that the lift coefficient is governed by the gap-to-diameter ratio G/D while the drag coefficient is dominated by the ratio of gap to thickness of the boundary layer, G/δ. Buresti and Lanciotti [4] measured mean and fluctuating forces on a circular cylinder near a plane surface in cross-flow submerged in three different types of boundary layer on the plane, at Reynolds number range of 0.86 to 2.77×10^5 and for various gap distances from 0 to 1.5. They found that vortex shedding persistence and suppression, regardless of boundary layer thickness on the plane, is a coherent feature of the flow unless the vertical velocity gradient becomes excessive. Generally, The critical gap, at which the vortex shedding ceases, decreases with increasing the boundary layer thickness but it may become larger in thicker boundary layers if the velocity gradient is greater than a limit value. Effects of other parameters like bed proximity, boundary layer thickness, Reynolds number and separation angles on vortex shedding state has been investigated in other studies.

Oner et al. [5] used particle image velocimetry (PIV) technique to measure the velocity field in a steady, two-dimensional, turbulent flow around a horizontal circular cylinder near a plane boundary. They presented the results for velocity profiles, streamlines and iso-vorticity contours for seven different gap ratios and Reynolds numbers of 840, 4150 and 9500. They illustrated some of the near wall flow field parameters around the circular cylinder through a definition sketch, Fig 1. Where D is the cylinder diameter, u_0 is the free-stream velocity, δ is the boundary layer thickness, θ_s is the stagnation angle, θ_{sep} is the separation angle and G is the gap distance. The four regions of disturbed flow around a circular cylinder near a plane boundary have been illustrated by a, b, c and d labels. Region d signifies the wake region.

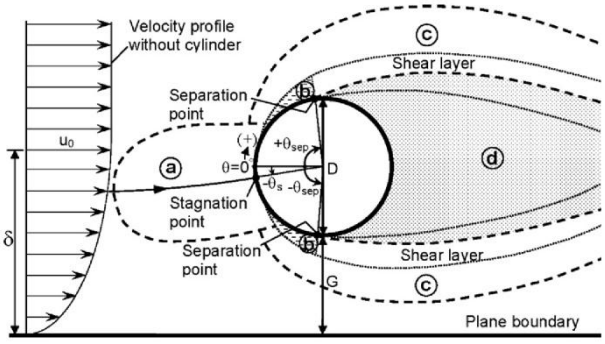

Fig. 1. Definition of near wall flow field parameters around circular cylinder, Oner et al. (2008)

Their results showed that the variations of the parameters such as separation angle, stagnation angle and Strouhal number for $G/D \geq 0.3$ and also the wall proximity effect on the flow becomes insignificant for $G/D \geq 1$. Experiments conducted by Lei et al. [6] investigated the hydrodynamic forces and vortex shedding of a circular cylinder in different boundary layers at Reynolds number range of 1.3×10^4 to 1.45×10^4. They suggested a quantitative method for identifying the vortex shedding suppression and observed that the critical gap ratio of the inception of vortex shedding suppression decreases as the thickness of boundary layer increases. Price et al. [7] visualized the flow around a circular cylinder near a plane wall for $1200 < Re < 4960$ and $0 < G/D < 2$ and categorized the flow to four distinct regions. They observed that for very small gaps ($G/D \leq 0.125$), despite the gap flow is suppressed or extremely weak, there's a periodicity attributed to the outer shear layer. They concluded that for the small gap ratio region ($0.125 < G/D < 0.5$), the pairing between the inner shear layer and the wall boundary layer is more pronounced. At the intermediate gap ratios ($0.5 < G/D < 0.75$), the onset of vortex shedding occurs and for large gap ratios ($G/D > 1$), no separation of wall boundary layer appears either upstream or downstream of the cylinder.

Wang and Tan [8] experimentally studied the flow characteristics in the near wake of a circular cylinder near a plane wall at the Reynolds number of 1.2×10^4 and for various gap ratios from 0.1 to 1. Results showed that for the gap ratio $G/D \geq 0.3$, the flow is characterized by the periodic, Karman-like vortex shedding from the upper and lower sides of the cylinder, while for small and intermediate gap ratios ($G/D \leq 0.6$), the wake flow develops a distinct asymmetry about the cylinder centerline; however, some flow quantities, such as the Strouhal number and the convection velocity of the shed vortex, keep roughly constant and virtually independent of G/D. Lin et al [9] investigated the flow characteristics in the near wake of a circular cylinder near a plane boundary experimentally at the Reynolds number range of 7.8×10^2 to 1.15×10^4 and for various gap heights (G)

from 0 to 4. Wake and gap flow characteristics inspected and it has been observed that for G/D < 0.5 A recirculating eddy is formed on the plane boundary upstream of the circular cylinder and its size increases with the decrease in gap ratio. This eddy deflects a part of the upstream fluid over the top surface of the circular cylinder and reduces the flow through the gap. For gap ratios between 0.1 and 0.3, the gap flow shows the wall-jet characteristics and a formula for recirculation zone border was presented based on the maximum value of horizontal velocity and its corresponding location.

Great efforts are made by many researchers to describe the vortex shedding and suppression mechanism and its subsequent influence on the wake flow and gap flow in the presence of the wall. The assessment of the vorticity dynamics to inspect flow unsteadiness and the instability mechanism to investigate the vortex induced instability is made by Dipankar and Sengupta [10] as they studied how lift and drag coefficients are affected by the gap ratios of G/D=0.5, G/D=1.5 and Re=1200. They concluded that the vortex induced instability occurs due to mutual interaction of vorticity field from the plane wall boundary layer and the vortices created on the cylinder surface that are shed afterwards. They considered the presence of the plane wall as a source of perturbation for the flow past the cylinder and vice versa, and observed large spatio-temporal growth of the disturbance field during wall and cylinder interactions. Physics of flow in the presence of the wall including the shear layer transition, stretching, breakdown and turbulence generation investigated by Sarkar and Sarkar [11] for a Reynolds number of 1440. They employed large-eddy simulations to assess the modifications of wake dynamics and turbulence characteristics behind a circular cylinder placed near a wall for different gap-to-diameter (G/D) ratios. They noticed that the suppression of vortex shedding and stretching of the shear layers occur due to the strong coupling between inner shear layer and approaching boundary layer while the inner shear layer is submerged inside the boundary layer ($G \leq \delta$). He et al. [12] through PIV experiments studied the dynamics of vortical structures in flow over a circular cylinder in the vicinity of a flat plate for various gap ratios ($0 < G/D < 3$) and at Re=1072. They classified the entire region of G/D into five sub-regions based on gap ratios. They observed that for G/D=0 and 0.25 the lower shear layer from the cylinder is inhibited or completely suppressed, while no distinguished peak on velocity can be detected which indicates the cease of vortex shedding process.

As noticed through reviewing the type of studies focused on the wake dynamics and vortex shedding phenomenon, still considerable uncertainties and questions remained on the mechanism of vortex shedding such as; the inception, the continuation and the suppression of vortex shedding. For instance, as the vortex shedding depends on flow regime, geometry, boundary layer characteristics and other factors, still there is no clear understanding that which one mostly influences the stability or suppression of vortex shedding. In this study, three-dimensional flow around a circular cylinder far from and near the plane boundary has been simulated numerically using Open source CFD codes of OpenFOAM. Pressure distribution around the circular cylinder, base pressure magnitude, separation and stagnation angles, force coefficients and Strouhal numbers were calculated and compared for all of the cases. Additionally, detailed velocity and vorticity fields in the wake have been discussed through parameters like Q-criterion, normalized spanwise vorticity and the flow type parameter to scrutinize the wake flow and the possibility of vortex shedding occurrence. At the end, a quantitative method in terms of parameter Λ, the ratio of swirling strength of the upper vortex sheet to the lower one, has been introduced to detect the occurrence of vortex shedding suppression.

2. Governing Equations

Time averaged Navier-Stokes equations including continuity equation are the governing equations for incompressible fluid flow:

$$\frac{\partial u_i}{\partial x_i} = 0 \tag{1}$$

Momentum equation 2 divided by ρ:

$$\rho\left(\frac{\partial u_i}{\partial t} + u_j \frac{\partial u_i}{\partial x_i}\right) = B_i - \frac{\partial p}{\partial x_i} + \mu \frac{\partial^2 u_i}{\partial x_j \partial x_j} + \frac{\partial}{\partial xj}\left(-\rho \overline{u_i' u_j'}\right) \tag{2}$$

$$\frac{\partial u_i}{\partial t} + u_j \frac{\partial u_i}{\partial x_i} = -\frac{1}{\rho}\frac{\partial p}{\partial x_i} + \nu \frac{\partial}{\partial x_j}\left[\frac{\partial u_i}{\partial x_j} + \frac{\partial u_j}{\partial x_i}\right] - \frac{\partial \overline{u_i' u_j'}}{\partial xj} \tag{3}$$

The Reynolds stress tensor approximated by Boussinesq model:

$$\overline{\partial u_i' u_j'} = \nu_t \left(\frac{\partial u_i}{\partial x_j} + \frac{\partial u_j}{\partial x_i}\right) - \frac{2}{3} k \delta_{ij} \tag{3}$$

Where u, p, ρ, υ, B and τ are the velocity, pressure, density, kinematics viscosity, body forces and Reynolds stress, respectively. K-ω SST, a two-equation eddy-viscosity turbulence model has been employed to close the system of equations. K-ω SST, presented by Menter [13] is a variant of the standard k–ω model which Combines the original Wilcox k-ω model for use near walls and the standard k–ε model away from walls using a blending function, F1, and the eddy viscosity formulation is modified to account for the transport effects of the principle turbulent shear stress. This turbulence model solves one transport equation for the turbulent kinetic energy, k, and one transport equation for the dissipation per unit

kinetic energy, ω, also regarded as a turbulent frequency scale.

The original K-ω equations, multiplied by F_1 and the transformed k–ε equations multiplied by $(1-F_1)$, have been added together to comprise the new SST model equations including the turbulence kinetic energy, equation 5 and the specific dissipation rate, equation 6:

$$\frac{\partial(\rho k)}{\partial t}+\frac{\partial(u_j k)}{\partial x_j}= P-\beta^*\rho k\omega+\frac{\partial}{\partial x_j}\left((\mu+\sigma_k\mu_t)\frac{\partial k}{\partial x_j}\right) \quad (5)$$

$$\frac{\partial(\rho\omega)}{\partial t}+\frac{\partial(u_j\omega)}{\partial x_j}=\frac{\gamma}{\nu_T}P-\beta\rho\omega^2 +\frac{\partial}{\partial x_j}\left((\mu+\sigma_\omega\mu_T)\frac{\partial\omega}{\partial x_j}\right)+2(1-F_1)\sigma_{\omega2}\frac{\rho}{\omega}\frac{\partial k}{\partial x_i}\frac{\partial\omega}{\partial x_i} \quad (6)$$

The closure coefficients and auxiliary relations such as production of k, P, and kinematic eddy viscosity, υ_t, are determined as follow, equations 7 and 8:

$$P=\min\left(\tau_{ij}\frac{\partial u_i}{\partial x_j},10\beta^*k\omega\right) \quad (7)$$

$$F_1=\tanh\left(\arg_1^4\right)= \tanh\left\{\left\{\min\left[\max\left(\frac{\sqrt{k}}{\beta^*\omega y},\frac{500\nu}{y^2\omega}\right),\frac{4\sigma_{\omega2}k}{CD_{k\omega}y^2}\right]\right\}^4\right\} \quad (8)$$

$$\alpha_1=\frac{5}{9},\quad \alpha_2=0.44,\quad \beta_1=0.075,\quad \beta_2=0.0828,\quad \beta=\frac{9}{100},$$
$$\sigma_{k1}=0.85,\quad \sigma_{k2}=1,\quad \sigma_{\omega1}=0.5,\quad \sigma_{\omega2}=0.856$$

Where y is the distance to the next surface, Ω is the vorticity tensor and CD_{kw} is the positive portion of the cross diffusion term.

3. Computational meshing

In order to select the proper mesh within the computational domain, sensitivity analysis is performed for different meshes inside subdomain 1 around the cylinder in different cases. Computational domain size and the location of subdomain 1 for the case of G/D=1 and inlet uniform velocity of 0.039 m/s, are shown in Fig. 2. Characteristics of the different computational meshes used are presented in Table 1.

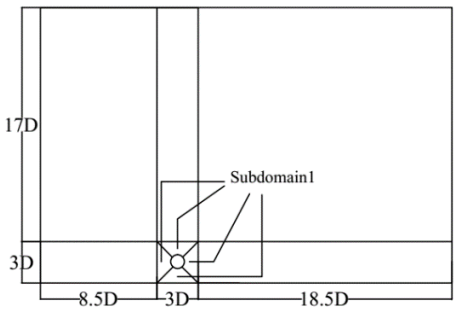

Fig. 2. Computational domain details for G/D=1

Table 1. Characteristics of different meshes used

Mesh name	Max. Δx in subdomain1	Max. Δy in subdomain1	Number of meshes per diameter in horizontal direction	Number of meshes per diameter in vertical direction
Mesh 1	0.0075	0.0075	40	40
Mesh 2	0.006	0.006	50	50
Mesh 3	0.01	0.01	30	30

According to the comparison of time-averaged velocity profiles for different mesh resolutions presented in Fig. 3, in which close results are observed, the mesh resolution 1 is selected as the optimum mesh of the computational domain used in the case of Re=3900 and G/D=1.

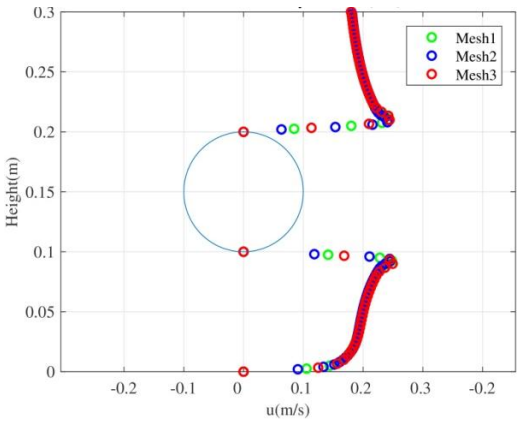

Fig. 3. Time-averaged horizontal velocity profiles for different mesh resolutions applied on subdomain 1, for Re=3900 and G/D=1

4. Near-wall treatment and free-stream initial conditions for turbulent Re=3900 cases at OpenFOAM

For Re=3900 cases turbulence has been modeled by K-ω SST turbulence model. For initial free-stream conditions, the turbulence kinetic energy, k, the turbulence specific dissipation, ω, the kinematic eddy viscosity, ν_t , and the turbulence length scale, L, can be estimated by equations 9, 10, 11 and 12 respectively.

$$k=\frac{3}{2}\left(I\left|u_{ref}\right|\right)^2 \quad (9)$$

$$\omega = k^{0.5} / c_\mu L \quad (10)$$

$$\nu_t = \sqrt{3/2} u_{ref} IL \quad (11)$$

$$L = 0.07 D_h = 0.07 D \quad (12)$$

Where I is the turbulence intensity, u_{ref} is the reference velocity, D_h is hydraulic diameter equal to cylinder diameter, D, and c_μ is a constant equal to 0.09. Depending on the dimensionless wall distance unit y^+ value, which is considered equal to 30 in all cases in order to utilize wall functions, k, ω and ν_t wall boundary conditions determined as equations 13 to 17.

$k_{wall} = kqrwallfunction = k$, acts as a zero gradient condition (13)

$$\omega_{wall} = omegawallfunction = \sqrt{\omega_{vis}^2 + \omega_{\log}^2} \quad (14)$$

$$\omega_{vis} = 6\nu / \beta_1 y^2 \quad (15)$$

$$\omega_{\log} = \sqrt{k} / \sqrt[4]{\beta^*}\kappa y \quad (16)$$

$$\nu_{twall} = nutUSpaldingwallfunction = (u_\tau)^2 / (\partial u / \partial n) - \nu \quad (17)$$

Where ω_{vis} and ω_{log} are respectively the omega values at the viscous sub-layer and logarithmic regions, β=0.075, u_τ is the friction velocity, κ is the Von Karman constant and y is the distance to the first cell center normal to the wall. Kqrwallfunction, omegawallfunction and nutUSpaldingwallfunction are the wall functions used by OpenFOAM to consider the boundary conditions on the wall. The boundary layer thickness and mesh dimension closest to the wall at y^+=30 are computed as equations 18 to 23.

$$\mathrm{Re}_x = ux / \nu \quad (18)$$

$\delta = 0.382x / \mathrm{Re}_x^{1/5}$, based on Schlichting empirical equation [14] (19)

$c_f = \left[2\log(\mathrm{Re}_x) - 0.65\right]^{-2/3}$, based on Schlichting [14] for $\mathrm{Re}_x \le 10^9$ (20)

$$\tau_\omega = \frac{1}{2}\rho c_f u_{freestream}^2 \quad (21)$$

$$u_\tau = \sqrt{\tau_\omega / \rho} \quad (22)$$

$$\Delta = y = \nu y^+ / u_\tau \quad (23)$$

Where δ is the boundary layer thickness, c_f is the skin friction coefficient, τ_ω is the wall shear stress and Δ is the dimension of the cells adjacent to the wall.

5. Model validation

Comparison of simulation results for flow around a circular cylinder far from plane boundary at Re=100, including average drag coefficient, positive maximum value of lift coefficient and Strouhal number were considered and compared with those obtained by Cao and Wan [15] and showed good agreement according to Table 2. Also the computational velocity fields from the present simulations are compared with the experimental results obtained from PIV measurements of Oner et al. [5] at Re=9500 for further validation of the numerical model, which can be seen in Fig. 4.

Table 2. Comparison of C_d, C_l(max) and S_t parameters at Re=100

	C_d	C_l (max)	S_t
Present study	1.3918	0.3229	0.1613
Cao and Wan [5]	1.3932	0.3347	0.168

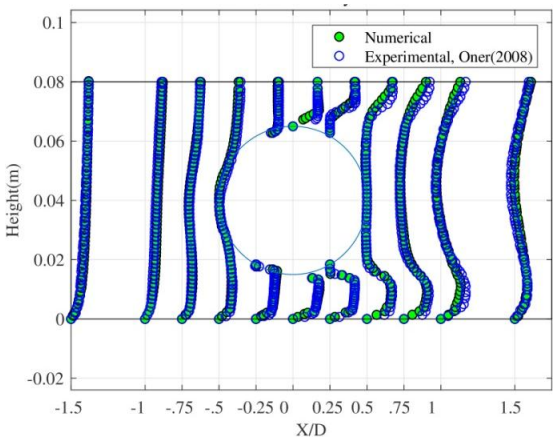

Fig. 4.comparison of horizontal velocity profiles of present numerical simulation and experimental study of Oner et. al [5] for G/D=0.3 and Re=9500

6. Results and Discussion

Time-averaged pressure distribution around a circular cylinder represented by pressure coefficient and separation points for all cases, cylinder far from and near the wall, have been presented in Figs. 5 to 8. It is seen that bell-shaped pressure coefficient distribution pattern includes a smaller section of positive pressure coefficient in front of cylinder and a bigger section of negative pressure coefficient around the other parts of the cylinder perimeter. In all cases, far from and near the wall, the symmetry of pressure coefficient around the stagnation point has been observed. Investigation of pressure coefficient around the cylinder shows that by reducing gap ratio, G/D, higher lift force pushes the cylinder upward. The amount of lift increase is less pronounced when vortex shedding is suppressed or boundary layer is thicker. By increasing G/D, positive and negative values of pressure coefficients around the cylinder are decreased, hence mean lift force on the cylinder decreases too. In high inference between the cylinder and the wall, i.e. smaller G/D, and when boundary layers around the cylinder and the wall overlap fittingly, the maximum of positive pressure coefficient increases and moves downstream.

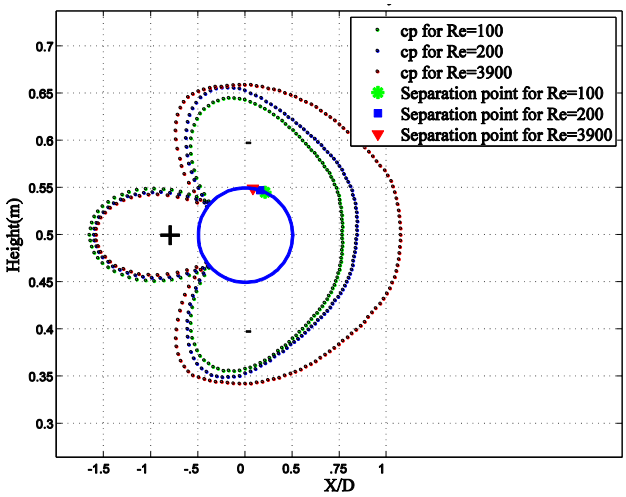

Fig. 5. Pressure coefficient distribution around circular cylinder at G/D=∞, for Re=100,200,3900

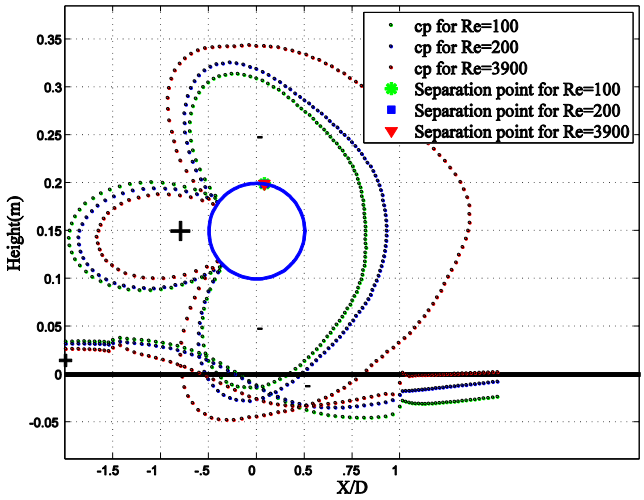

Fig. 6. Pressure coefficient distribution around circular cylinder at G/D=1, for Re=100,200,3900

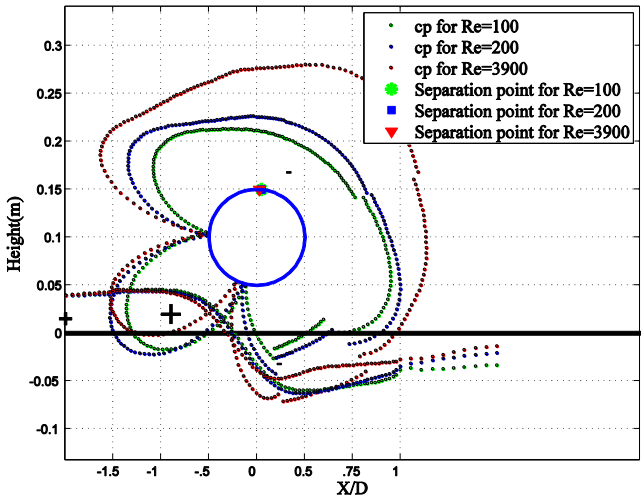

Fig. 7. Pressure coefficient distribution around circular cylinder at G/D=0.5, for Re=100,200,3900

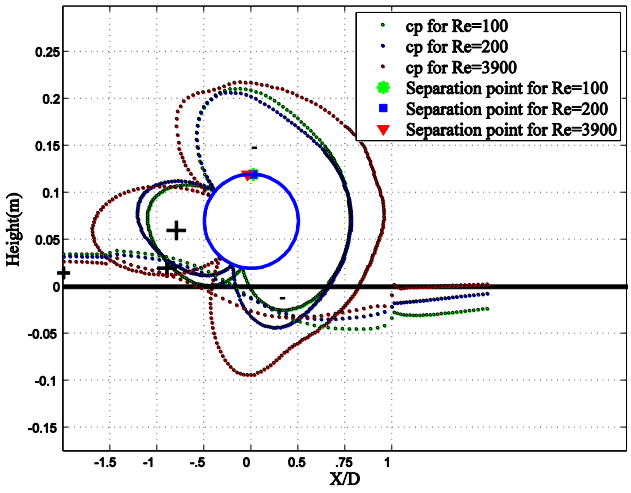

Fig. 8. Pressure coefficient distribution around circular cylinder at G/D=0.2, for Re=100,200,3900

Tables 2,3 and 4 present the results of 3-D computations including hydrodynamic drag, C_d(mean) and lift coefficients, C_l(rms), Strouhal number (st), gap to boundary layer thickness ratio (G/δ), Separation angle, Stagnation angle and base pressure, Cpb, for different gap ratios and Re=100, 200 and 3900. It has been observed that for the range of about $G/\delta < 0.55$ there is a high possibility of vortex shedding suppression. The thickness of the boundary layer, δ, can be determined by measuring the velocity profile of the boundary layer at the cylinder location.

Based on Figs. 6, 7 ,8 and 9, it can be observed that upper separation point moves counter-clockwise by increasing Reynolds number (decrease in separation angle, θ_s), in a fixed gap ratio. Also in a fixed Reynolds number, upper separation point moves upward by decreasing G/D (decrease in separation angle, θ_s). Upward displacement of upper separation point by approaching the wall, can be described by the growing stream-wise pressure gradient induced by the gap flow. Separation occurs when skin friction vanishes, where velocity gradient at the wall becomes zero. The effect of the boundary layer on the pressure distribution can be attributed to the existence of the velocity gradient in the boundary layer. Drag coefficient consists of friction drag and form (pressure) drag and major fluctuations of drag force around circular cylinder relates to form drag in a distinct flow regime. When drag coefficient, a function of pressure distribution, rapidly decreases, it can be deduced that friction drag increases with respect to form drag and velocity gradient reaches its maximum value, hence separation of boundary layer does not proceed, i.e. vortex shedding suppression occurs.

Stagnation point is the corresponding point on the cylinder surface to the maximum of positive pressure coefficient. It is shown that stagnation point moves toward wall by increasing Reynolds number (decrease in stagnation angle).

According to tables 2 to 4, Mean drag coefficient, C_d(mean) generally increases with increasing Gap ratio, G/D. But from G/D=1 to G/D=∞, considering the ratio of gap distance to cylinder boundary layer thickness, G/δ, reduction in drag coefficient observed, which is the result of the cylinder exit from the influence zone of plane wall`s boundary layer. Fig. 9 shows the variation of C_d(mean) for all cases. Oscillating lift coefficient, represented by C_l(rms), root mean square of lift coefficient, in Re=100, where boundary layer is thicker, shows bigger value near the wall. While for Re=3900, where boundary layer is thinner, C_l(rms) decreases when cylinder approaches the wall. Increase of C_l(rms) near the wall in thick boundary layer can be explained by increase of the lift coefficient near the wall, as a result of the perturbance of reverse pressure gradient above and below the cylinder which makes the positive fluctuations of lift coefficient bigger. The variation of C_l(rms) can be seen in Fig. 10, Vortex shedding frequency, represented by Strouhal number, St, in thicker boundary layers (lower Reynolds numbers) increases by decreasing G/D and vice versa.

Table 3: 3-D numerical results of flow around circular cylinder far from and near the wall for Re=100

Re=100	G/D=∞	G/D=1	G/D=0.5	G/D=0.2
C_d(mean)	1.269	1.61	1.405	1.165
C_l(rms)	0.111	0.2	0.163	0.598
st	0.161	0.183	0.183*	0.196*
G/δ	-	1.042	0.521	0.208
separation angle	114.72	98.97	95.51	92.29
stagnation angle	0	-2.2	-5.5	-9
Cpb	-0.53	-0.64	-0.52	-0.56

Table 4: 3-D numerical results of flow around circular cylinder far from and near the wall for Re=200

Re=200	G/D=∞	G/D=1	G/D=0.5	G/D=0.2
C_d(mean)	1.208	1.518	1.425	1.143
C_l(rms)	0.306	0.492	0.342	0.417
st	0.192	0.209	0.233	0.25*
G/δ	-	1.19	0.595	0.238
separation angle	108.07	98.97	95.51	92.29
stagnation angle	0	-2.2	-8.1	-11
Cpb	-0.69	-0.86	-0.72	-0.57

Table 5: 3-D numerical results of flow around circular cylinder far from and near the wall for Re=3900

Re=3900	G/D=∞	G/D=1	G/D=0.5	G/D=0.2
C_d(mean)	1.281	1.712	1.544	1.238
C_l(rms)	0.677	1.032	0.896	0.51
st	0.214	0.18	0.233	0.15*
G/δ	-	2.174	1.087	0.435
separation angle	98.98	98.97	92.75	85.5
stagnation angle	0	-2.2	-14.7	-6.8
Cpb	-1.15	-1.71	-1.13	-0.91

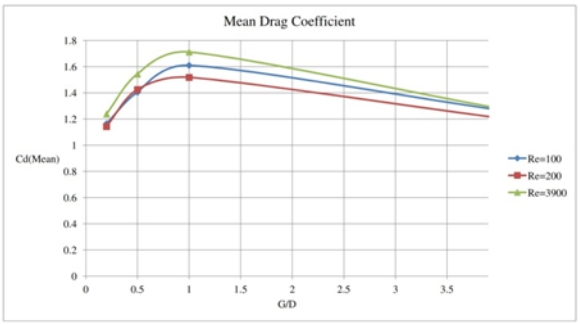

Fig. 9. Mean Drag coefficient versus G/D for Re=100, 200, 3900

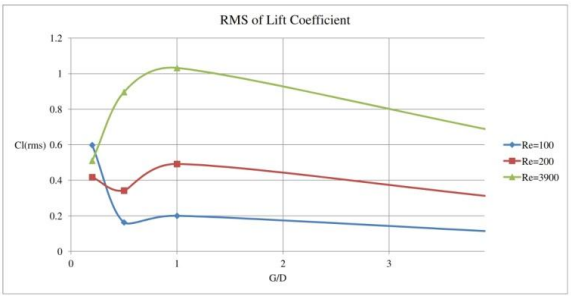

Fig. 10. RMS of lift coefficient versus G/D for Re=100, 200, 3900

Time-averaged horizontal velocity gradient between top and bottom of the cylinder is extracted by two probes and is presented for all cases in table 6 and Fig. 11.

Table 6. Time-averaged horizontal velocity gradient between top and bottom of the cylinder for all cases

G/D	Re=100	Re=200	Re=3900
0.2	0.1065	0.0864	0.2933
0.5	0.0596	0.0469	0.2619
1	0.0836	0.1399	0.3662
∞	0.0012	0.0161	0.0058

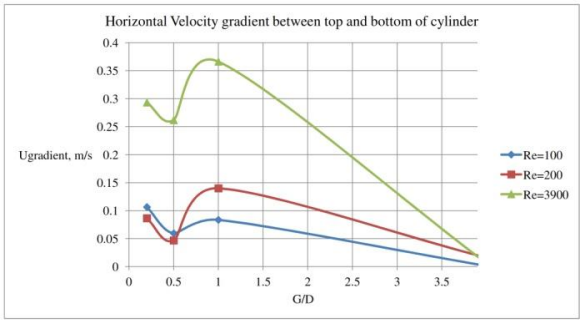

Fig. 11. Time-averaged horizontal velocity gradient between top and bottom of the cylinder versus G/D for Re=100, 200, 3900

The sudden increase in velocity gradient between top and bottom of the cylinder at G/D=1 in all Reynolds numbers is due to the location of bottom probes at the boundary of the wall boundary layer. Intrinsically the

variation of velocity profile at the interference region of the boundary layers becomes considerable.

Vortex shedding suppression can be predicted by monitoring the variations of pressure distribution around the circular cylinder near the boundary, hence suppression can be preceded by modifying the pressure distribution patterns. Vortex shedding suppression observed in 4 cases, all of three cases of flow around a circular cylinder near wall with G/D=0.2 and the other one for flow around a circular cylinder near wall with G/D=0.5 and Re=100. For these cases, a sustained negative pressure is observed at the free-stream side of the cylinder and a less pronounced negative pressure is observed at the wall-side of the cylinder. The maximum of positive pressure coefficient experiences a chamfer in shape and a bit of decrease in value while suppression occurs. Insufficient gradient of pressure between free-stream side and wall-side of cylinder leads to a static and stable state of shear layers, which prevents the process of vortex shedding to proceed or even to form vortex sheets in the high interference conditions of boundary layers, i.e. very low G/δ - the situation that the rolling up of shear layers cannot be happened.

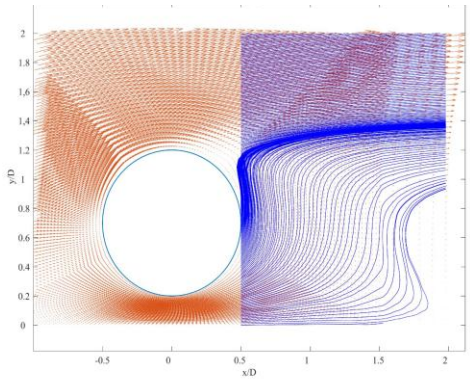

(a)

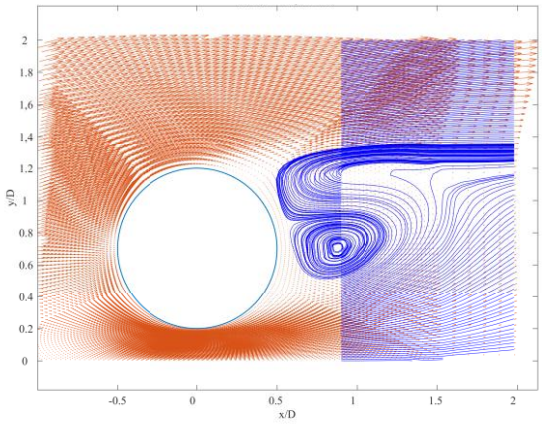

(b)

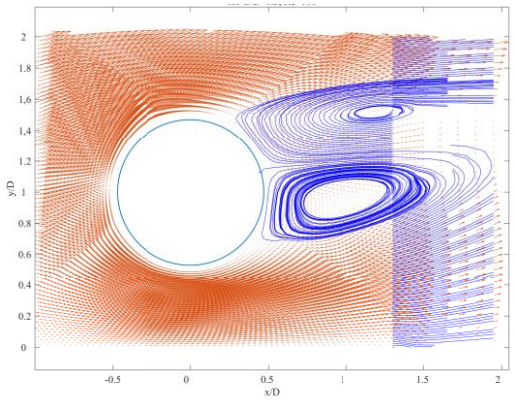

(c)

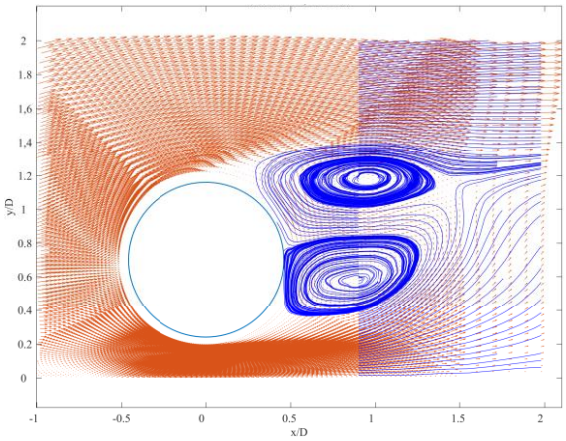

(d)

Fig. 12. Time-averaged streamlines and velocity vectors behind a circular cylinder for (a) G/D=0.2, for Re=100, (b) G/D=0.2, for Re=200, (c) G/D=0.5, for Re=100, (d) G/D=0.2, for Re=3900

Velocity vectors and time-averaged streamlines behind a circular cylinder for the cases subjected to vortex shedding suppression have been demonstrated in Fig. 12.

In order to focus on maintaining or suppression of the vortex shedding process, different aspects of vortex shedding mechanism should be investigated. At subcritical Reynolds numbers Von Karman vortex street is the dominant pattern of vortex shedding which is based on subsequent shedding of swirling vortices from top and bottom of the cylinder. It`s necessary for the vorticity sheets in upper and lower of the wake to be symmetric around the wake centerline and also the upper and lower vortex sheet strengths should be of almost the same range of value to develop vortex shedding in the Von Karman vortex street pattern. The strength of upper and lower vortex sheets can be quantified by circulation or swirling strength value, Γ, which is defined by equation 24:

$$\Gamma = \int\int_{A} \omega_z \, dx dy \tag{24}$$

Where ω_z is the spanwise vorticity and A is the area of the vorticity integration and should be determined for each vortex region. To identify the distinct regions of

vorticity where the vortices can be formed around the cylinder, Q-criterion is employed. The Q-criterion defines a vortex as a connected fluid region with a positive second invariant of the velocity gradient, which means for Q > 0. Q tensor can be defined in terms of strain rate and vorticity tensors by equation 25.

$$Q = \frac{1}{2}\left\|\bar{\Omega}\right\|^2 - \left\|\bar{S}\right\|^2 \tag{25}$$

Where strain rate tensor and vorticity tensor in two dimensions can be expressed as follows in equations 26 and 27:

$$S_{ij} = \frac{1}{2}\left(\frac{\partial u_i}{\partial x_j} + \frac{\partial u_j}{\partial x_i}\right) \tag{26}$$

$$\Omega_{ij} = \frac{1}{2}\left(\frac{\partial u_i}{\partial x_j} - \frac{\partial u_j}{\partial x_i}\right) \tag{27}$$

Time averaged normalized spanwise vorticity contours around the cylinder inside positive Q-criterion regions (colored area) for the cases subjected to vortex shedding suppression have been displayed in Fig. 13.

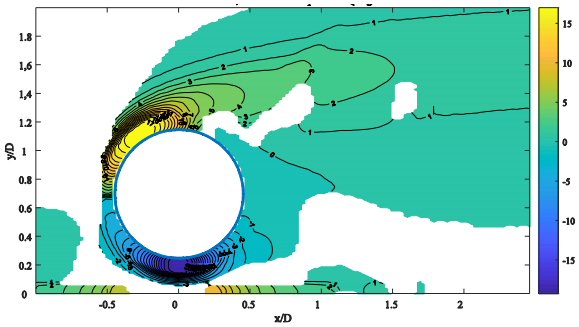

(a)

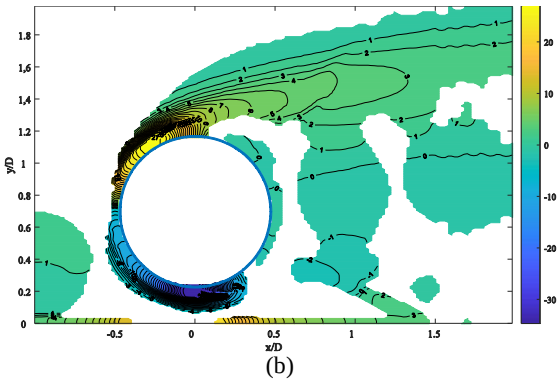

(b)

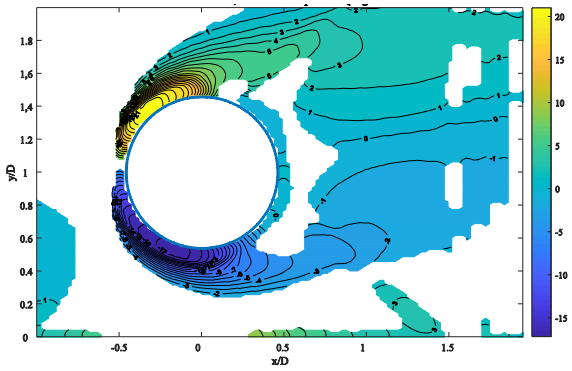

(c)

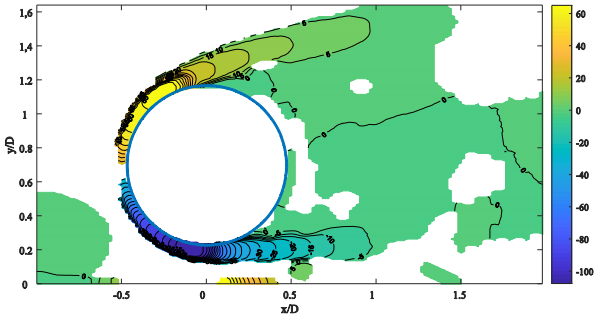

(d)

Fig. 13. Time-averaged normalized spanwise vorticity contours for (a) G/D=0.2, Re=100, (b) G/D=0.2 ,Re=200 (c) for G/D=0.5, Re=100 (d) G/D=0.2, Re=3900 ; colored area denounce the positive Q criterion.

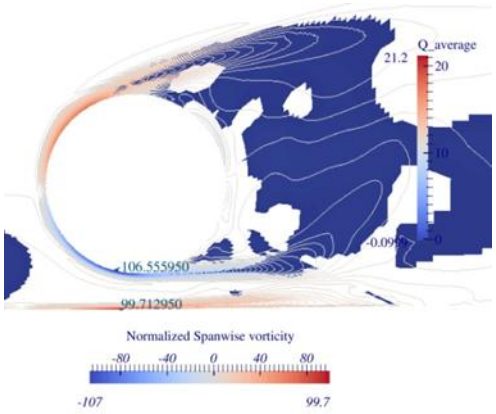

Fig. 14. Time-averaged normalized spanwise vorticity contours and extremum values for G/D=0.2 and Re=3900, colored area denounce the positive Q criterion

Time-averaged normalized spanwise vorticity contours and extreme values for G/D=0.2 and Re=3900 inside vorticity regions is presented in Fig. 14 and shows that the extremums of normalized spanwise in the gap flow between the cylinder and the plane wall contain close values with opposite signs. Which means the vorticity field in the gap flow is supposed to be cancelled out due to the interference of vorticity fields of the cylinder and the wall.

A parameter Λ is introduced as absolute proportion of upper vortex sheet swirling strength to the lower one, which can be a measure of vorticity strength balance between upper and lower vortex sheets. Time-averaged swirling strength for upper and lower vortex

sheets and Λ for all cases is presented in table 7. It can be observed that suppression occurs for the cases with $\Lambda \geq 2$, which implies the unbalance of vorticity content of vortices about the wake centerline. In these cases upper shear layer which feeds into upper vortex gains strength but the lower shear layers weakens and therefore unable to feed vorticity in the vortex region and draw the upper shear layer afterwards.

Table 7. Time-averaged swirling strength for upper and lower vortex sheets and Λ for all cases

		Γl(Lower vortex sheet)	Γu(Upper vortex sheet)	$\Lambda=\lvert \Gamma u/\Gamma l \rvert$
G/D=0.2	Re=100	-0.0014	0.0019	N
	Re=200	-0.000493	0.0013	2.637
	Re=3900	-0.0651	0.1955	3.003
G/D=0.5	Re=100	-0.0013	0.0026	2.000
	Re=200	-0.0018	0.002	1.111
	Re=3900	-0.1224	0.1327	1.084
G/D=1	Re=100	-0.0011	0.0012	1.091
	Re=200	-0.0037	0.0037	1.000
	Re=3900	-0.0687	0.0742	1.080
G/D=∞	Re=100	-0.00147	0.0014	0.952
	Re=200	-0.0044	0.0041	0.932
	Re=3900	-0.0596	0.0601	1.008

Existence of vortical activity and vortex regions do not ensure the maintaining of the vortex shedding mechanism. Vortex shedding mechanism depends on vortex stretching and perturbation growth respectively represented by extensional strain and perturbation vorticity. Rotational field and vortex formation is already discussed by applying Q-criterion and measuring normalized spanwise vorticity contours. According to Sengupta et al. [16] disturbance energy grows while the right-hand side of equation 28 becomes negative which implies a source in energy.

$$\Delta^2 E_d = 2\omega_m.\omega_d + \omega_d.\omega_d - V_m.\nabla\times\omega_d - V_d.\nabla\times\omega_m - V_d.\nabla\times\omega_d \quad (28)$$

Where E_d is the disturbance energy and subscripts "m" and "d" denote mean and disturbance parts of velocity and vorticity fields. This indicates that the last three kinematic terms including velocity and vorticity vectors should contribute as strong source terms to overcome first two terms of vorticity energy dissipation. The mentioned terms can be best represented by the extensional strain. It can be also perceived that the spatial variation of the vorticity field in interaction with the velocity field should contribute to instability in shear layer at the bottom of the cylinder. Extensional strain which can be quantified by the magnitude of strain rate tensor, S, supplies the extension and propagation of the perturbations in the gap flow.

A new parameter called the flow type parameter, λ, is introduced according to the following equation 29:

$$\lambda = \frac{\|S\| - \|\Omega\|}{\|S\| + \|\Omega\|} \quad (29)$$

If λ value approaches -1, it means flow is mostly rotational and if approaches 1, it means planar extensional flow is dominant. Zero value indicates simple shear flow. While extensional strain needs to be large enough to secure vortex stretching in the gap flow, positive λ contours in this region is beneficial and shear layers can feed source generated disturbances from previous cycle of vortex formation. Flow type parameter contours for flow around a circular cylinder for two cases of G/D=0.5 have been compared in Fig. 16. For the first case with Re=100 in which vortex shedding is eventually suppressed, negative dashed contours compactly engages positive contours in the gap flow and interrupts the extensional strain which is dominated by magnitude of strain rate tensor. The flow type parameter contours for the second case with Re=200 is relatively more symmetric with respect to horizontal cylinder centerline and extensional strain is less interrupted by negative contours, which can damp the energy needed to feed the subsequent vortex formation and stretching, Fig. 16.

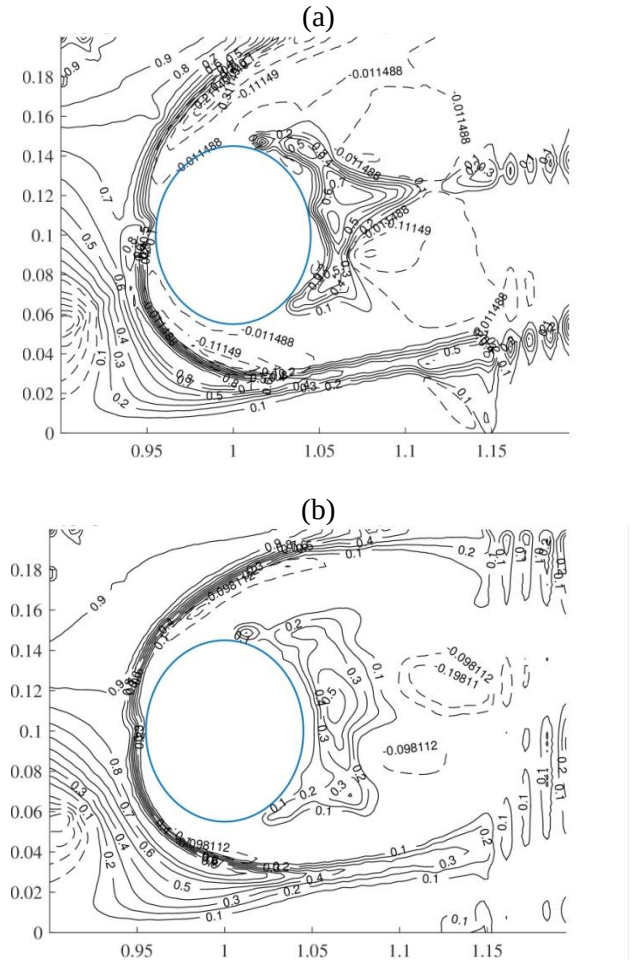

Fig. 16. Time-averaged λ contours around a circular cylinder for (a) G/D=0.5, Re=100, (b) G/D=0.5, Re=200

7. Conclusion

Flow around a circular cylinder near plane has been studied numerically in different flow regimes (Re=100, 200, 3900) with different gap ratios (G/D=∞, 1, 0.5, 0.2). Pressure distribution around the circular cylinder has been utilized to describe the variations in hydrodynamic force coefficients as well as other features of wake flow such as separation and vortex shedding phenomenon near a plane boundary. Plane wall effect on pressure distribution in different flow regimes was also assessed and it was observed that the inception of vortex shedding suppression can be deduced from pressure distribution pattern, through pressure gradient between free-stream-side and wall-side of cylinder and also the sudden decrease in maximum of positive pressure coefficient. Mean drag coefficient increases when cylinder approaches the wall until G/D=1, but when cylinder submerges further in the plane wall's boundary layer, C_d(mean) decreases as C_{pb} decreases. C_l(rms) near the wall in thick boundary layer near the wall, increases as a result of the perturbance of reverse pressure gradient above and below the cylinder which makes the positive fluctuations of lift coefficient bigger. In a constant flow regime, upper separation point moves upward by decreasing G/D, indicating that the separation angle, θ_s decreases too. This can be described by the growing stream-wise pressure gradient induced by the gap flow.

Vortex shedding suppression can also be assessed by the means of quantitative measures obtained from velocity and vorticity fields. A parameter Λ, the ratio of swirling strength of the upper vortex sheet to the lower one, has been introduced to detect the occurrence of vortex shedding suppression. Vortex shedding suppression is observed for the cases with the high unbalance vorticity content in the vortex regions, namely for $\Lambda \geq 2$. To ensure the evolution and stretching of vortices in the gap flow, the state of extensional strain is explored in the gap flow via the flow type parameter, λ. It has been observed that the presence of negative contours of λ in the gap flow acts as a sink of energy and interrupts vortex stretching at the lower side of the cylinder, which consequently can lead to the vortex shedding suppression.

8. References

1- Batham, J.P., (1973). *Pressure distributions on circular cylinders at critical Reynolds numbers*. Journal of Fluid Mechanics, Vol.57, p.209–228

2- Bearman P.W. & Zdravkovich M.M., (1978). *Flow around a circular cylinder near a plane surface*, Journal of Fluid Mechanics, Vol.89, p.33-47.

3- Zdravkovich M.M., (1985). *Forces on a circular cylinder near a plane wall*, Applied Ocean Research Vol.7, p.197-201.

4- Buresti, G., and Lanciotti, A., (1992). *Mean and fluctuating forces on a circular cylinder in cross-flow near a plane surface*, Journal of Wind Engineering and Industrial Aerodynamics, Vol.41(1–3), p.639–650.

5- Oner, A.A., Kirkgoz, M.S., Akoz, S., (2008). *Interaction of a current with a circular cylinder near a rigid bed*, Journal of Ocean Engineering, Vol.35, p.1492-1504.

6- Lei C., Cheng L., Kavanagh K., (1999). *Re-examination of the effect of a plane boundary on force and vortex shedding of a circular cylinder*, Journal of Wind Engineering and Industrial Aerodynamics, Vol.80(3), p.163–286.

7- Price, S.J., Sumner, D., Smith, J.G., Leong, K., Paidoussis, M.P., (2002). *Flow visualization around a circular cylinder near to a plane wall*, Journal of Fluids and Structures Vol.16, p.175–191.

8- Wang, X. K., Tan, S. K., (2008). *Near-wake flow characteristics of a circular cylinder close to a wall*, Journal of Fluids and Structures, Vol.24(5), p.605–627.

9- Lin W. J., Lin C., Hsieh S. C, Dey S., (2009). *Flow characteristics around a circular cylinder placed horizontally above a plane boundary*, Journal of Engineering Mechanics, Vol.135, p.697-716.

10- Dipankar, A., Sengupta, T. K. (2005). *Flow past a circular cylinder in the vicinity of a plane wall*, Journal of Fluids and Structures, Vol.20(3), p.403–423.

11- Sarkar, S., Sarkar, S. (2010). *Vortex dynamics of a cylinder wake in proximity to a wall*, Journal of Fluids and Structures Vol.26(1), p.19–40.

12- He, G. S., Wang, J. J., Pan, C., Feng, L. H., Gao, Q., Rinoshika, A,. (2017). *Vortex dynamics for flow over a circular cylinder in proximity to a wall*, Journal of Fluid Mechanics. Vol.812, p.698–720.

13- Menter F. R., (1994). *Two-equation eddy-viscosity turbulence models for engineering applications*. AIAA Journal, Vol.32(8), p.1598–605.

14- Schlichting, H., Gersten, K. (2017). *Boundary-Layer Theory*. Springer, Heidelberg.

15- Cao, H., Wan, D., (2010). *Application of OpenFOAM to Simulate Three-Dimensional Flows past a Single and Two Tandem Circular Cylinders*, Proceedings of the Twentieth International Offshore and Polar Engineering Conference Beijing, China, June 20-25, 2010.

16- Sengupta, T.K., De, S., Sarkar, S., (2003). *Vortex-induced instability of incompressible wall-bounded shear layer*. Journal of Fluid Mechanics Vol.493, p.277–286.